UNIVERSITEIT VAN PRETORIA
UNIVERSITY OF PRETORIA
YUNIBESITHI YA PRETORIA

COMBUSTION PERFORMANCE OF SELF-ASSEMBLY TERNARY PYROTECHNIC TIME-DELAY COMPOSITIONS

by

Shasha Guo (郭沙沙)

Thesis submitted in partial fulfilment of the requirements for the degree of

Doctor of Philosophy

in

Chemical Technology

in the

Department of Chemical Engineering
Faculty of Engineering, Built Environment and Information Technology

UNIVERSITY OF PRETORIA
Pretoria
December 2022

DECLARATION

I, Shasha Guo, student No. 17407100, do hereby declare that this research is my own original work, and that to the best of my knowledge and belief, it has not been previously, in its entirety or in part, been submitted and is not currently being submitted either in whole or in part at any university for a degree or diploma, and that all references are acknowledged.

SIGNED on this __15th___ day of __December__ 2022.

COMBUSTION PERFORMANCE OF SELF-ASSEMBLY TERNARY PYROTECHNIC TIME-DELAY COMPOSITIONS

Author: Shasha Guo

Supervisor: Prof. Walter W. Focke

Co-Supervisor: Prof. Shepherd M. Tichapondwa

Department: Chemical Engineering

Degree: Ph.D. (Chemical Technology)

ABSTRACT

Pyrotechnic compositions are usually employed in time delay detonators to facilitate controlled initiation of explosive charges in mining and quarrying operations. Traditional fast and slow-burning formulations are problematic, as they contain heavy metals which are bio-accumulative and toxic to the environment. Thermite and intermetallic reactions offer the possibility of greener alternatives. Unfortunately, the high reaction temperatures associated with conventional thermites cause operational failures due to melting of the metal housings. Similarly, it is difficult to achieve sustained burning with intermetallic systems alone. This study investigated the use of a combination thermite and intermetallic-type reactions, produced using environmentally benign materials to achieve both slow and fast-burning effects while overcoming the aforementioned limitations.

In order to obtain the fast-burning effect, a ternary composition based on powder mixtures of aluminium, nickel and nickel oxide was investigated. The maximum adiabatic temperature of the standard Al-NiO binary standard thermite was ca. 3100 K at a ca.19.8 wt-% Al content. The highest combustion rate (191 ± 31 mm·s^{-1}) was achieved for a binary composition with 35 wt-% Al content that was compacted in glass tubes with an internal diameter of 4.0 mm. Progressive dilution of the primary thermite reaction, $5Al + 3NiO \rightarrow Al_2O_3 + 3NiAl$, with the intermetallic reaction, $Al + Ni \rightarrow NiAl$, reduced the adiabatic reaction temperature by as much as 800 K while simultaneously maintaining consistent burn behaviour inside both glass and lead tubes. In the process, the burning rate gradually decreased from ca. 190 mm·s^{-1} to as

low as 23 $mm \cdot s^{-1}$. Analysis of the burn product residue revealed the presence of various Al-Ni intermetallic compounds.

For the slow-burning effect, a ternary composition comprising manganese and tin as fuels mixed with bismuth oxide as an oxidiser was explored. It was hypothesised that the high thermite reaction temperature would ensure a sustained intermetallic reaction, resulting in the desired slow-burning effect. Burn rates ranging from 2.9 to 10.9 mms^{-1} were obtained and were dependent on the relative proportions of the reagents. Burn rate predictions, using a Padè mixture model, were in close agreement with the measured data. The reaction products consisted of mixtures of metal oxides, manganese stannate, and Mn_3Sn, in which the latter was the only intermetallic formed. The slowest burning compositions were those associated with the formation of this intermetallic compound.

KEYWORDS: pyrotechnic, ternary delay composition, thermite, intermetallic, combustion rate

ACKNOWLEDGEMENTS

Having completed this dissertation, I would first like to thank the Doctoral Bursary supported by the University of Pretoria and Prof. Walter W. Focke, who gave me tremendous assistance with studying and living in South Africa.

First of all, my deepest gratitude goes to my supervisor, Prof. Walter W. Focke, for his constant encouragement and guidance, as well as his great contributions and pertinent suggestions. I learned so much from you and had a gratifying working experience with you. To my co-supervisor, Prof. Shepherd M. Tichapondwa, I would like to say thank you for your sharing, engaging discussions, and explaining my problems.

Secondly, I would like to express my heartfelt gratitude to Ms. Suzette Seymore who always made me feel at home and assisted me so much with my project. Ms. Wiebke Grote (XRD), Ms. Jeanette Dykstra (XRF), Ms. Charity Maepa (LM), Mr. Coenraad Snyman (LM) and Mr. Carel Coetzee (JEOL JSM-IT300LV SEM) are thanked for their technical support.

I really appreciate all the professional sharing and discussions from my group colleague Mr. Johannes M. Grobler, who always assisted me with any mechanical problems and took me to experience the local student lifestyle and local culture.

Lastly, special words of thanks and love to my parents, my husband, and my daughter. Thanks to my parents who helped me take care of my daughter (Tutu) when I was not in China, and to my husband who always gave me emotional understanding and support. I cannot say “love you” enough.

In a word, I have had a joyful experience of studying and life at the University of Pretoria, and I will miss everyone who has given me help during these years. Blessings for everyone to stay safe and keep well forever.

CONTENTS

LIST OF FIGURES

LIST OF TABLES

LIST OF ABBREVIATIONS AND SYMBOLS

Abbreviations

BET	Brunauer-Emmett-Teller
DSC	Differential scanning calorimetry
DTA	Differential thermal analysis
ID	Inner diameter of tubes
OD	Outer diameter of tubes
M	Mass weight
MICs	Metastable intermolecular composites
PVA	Polyvinyl Alcohol
PTFE	Polytetrafluoroethylene
SEM	Scanning electron microscopy
σ	Standard deviation
TGA	Thermogravimetric analysis
TMD	Theoretical maximum density
XRD	X-ray diffraction
XRF	X-ray fluorescence
wt- or *w*	Weight

Symbols

u	Combustion rate of a delay composition in delay elements	[$m \cdot s^{-1}$]
T_0	Ambient temperature	[K]
T_i	Initial temperature	[K]
T_c	Maximum temperature of the burning column	[K]
T_{ad}	Adiabatic reaction temperature	[K]
T_{ign}	Ignition temperature of compositions	[K]
T	Local temperature	[K]
z	Axial position of the cylindric delay column	[m]
d	Diameter of the cylindric delay column	[m]
t	Time	[s]
r_s	Rate of the chemical reaction	[$mol \cdot L^{-1} \cdot s^{-1}$]
Q	Apparent heat of reaction	[$J \cdot kg^{-1}$]

E_a	Apparent Arrhenius activation energy	[$J \cdot mol^{-1}$]
E_D	Apparent activation energy for diffusion coefficient	[$J \cdot mol^{-1}$]
A_0	Effective pre-exponential constant for the diffusion coefficient	[$m^2 \cdot s^{-1}$]
C_p	Apparent heat capacity	[$J \cdot kg^{-1} \cdot K^{-1}$]
α	Effective thermal diffusivity	[$m^2 \cdot s^{-1}$]
ρ	Bulk density of the delay composition	[$Kg \cdot m^{-3}$]
λ	Effective thermal conductivity	[$W \cdot m^{-1} \cdot K^{-1}$]
h	Heat transfer coefficient	[$W \cdot m^{-2} \cdot K^{-1}$]
σ	Stefan-Boltzmann constant	[$W \cdot m^{-2} \cdot K^{-4}$]
ε	Emissivity of the outer surface of the cylindric delay column	[-]
k_0	Arrhenius pre-exponential factor of reaction rate constant	[s^{-1}]
h_{rx}	Mass heat of reaction	[$J \cdot kg^{-1}$]
R	Gas constant (its value is 8.314)	[$J \cdot mol^{-1} \cdot K^{-1}$]
N	Constant equal to the reaction order	[-]
e	Natural number (its value is 2.71828)	[-]

1. INTRODUCTION

1.1 Background

Fireworks are known to the general public for their entertainment properties when used for commemorating momentous events or holidays. However, fireworks represent only a small subsection of the pyrotechnics world. The word “pyrotechnics” refers to the fire-related art or technology, derived from the Greek nouns *pyr* and *techne* for “fire” and “art”, respectively (Ellern, 1961). Therefore, both artistic creativity and scientific principles are ubiquitous and they are included in the world of pyrotechnics. Black powder is a well-known energetic material with historical significance. It was discovered in China in 220 BC and it is composed of sulphur, charcoal and potassium nitrate (saltpetre) (Buchanan, 2005; Steinhauser and Klapötke, 2008). Pyrotechnics is one of the three main close fields of energetic materials, the other two being explosives and propellants. Propellants provide energy which enables objects to propel, while explosives release energy capable of destroying or damaging objects. Pyrotechnics, on the other hand, are used in a wide range of applications such as smoke generation, time delays and flares, to mention a few. These three classes of energetic materials can also be differentiated based on their rate of energy release. Explosives react within microseconds, while the combustion rate of propellants is slow and can last for several seconds. Propellants or (high) explosives are sometimes used in pyrotechnic compositions, depending on the application, so the rate of energy release could be within a wide range, i.e. it could be very fast (detonators), very slow (slow delay compositions) or in between (Rossi et al., 2007; Klapötke, 2019).

Conventional pyrotechnics are based on intimate mixtures containing two or more powders which act as fuels, oxidisers or additives. These components undergo a highly exothermic, self-sustained and self-propagation reaction upon ignition. They are generally divided into categories based on the type of effect produced, which include airbag inflators, flares, tracers, smoke grenades, fireworks and time-delay compositions. Delay detonators with pyrotechnic compositions are commonly applied in mining, quarrying and blasting operations to facilitate controlled initiation of explosive charges. The time accuracy of sequential initiation events has a significant influence on the safety and effectiveness of blasting operations, and assist in obtaining better fragmentation and throw of the rock being blasted, less vibrations and air blast noise (Beck and Flanagan, 1992; Verma and Thote, 2013). Although both pyrotechnic and electronic delay detonators are in commercial use, pyrotechnic delay detonators are used more often due to their

smaller size, simplicity, low cost and safety due to the design configuration which gives immunity to stray current and current leakage hazards (Danali et al., 2010; Mui et al., 2015).

Time-delay pyrotechnic compositions are usually compacted or compressed into small-diameter tubes and preferably combusted in an essentially gasless fashion at a constant and predetermined rate. The actual combustion performance of time-delay compositions is determined by the nature of the reagents, the stoichiometry of the compositions, the mixing degree and the particle-particle contact area between the reactants, the geometry and the materials of the tubes. Among the numerous pyrotechnic time-delay compositions, thermites are those that produce high heat via a strongly exothermic reaction, and comprise metallic fuel powders with highly volumetric and gravimetric combustion enthalpies (e.g. Al, Mg, Mn, etc.) and metal-oxide oxidants such as Fe_2O_3, NiO, MoO_3, CuO, etc. On combustion, the metal fuel is oxidised by oxygen released from the decomposition of the oxidant to form its relatively more stable metal oxide, while the oxidant is reduced to its metal state. However, the high reaction temperature achieved with thermites hinder their direct application in conventional pyrotechnic time-delay systems, as the reaction temperature frequently far exceeds the melting points of the detonator subassemblies.

Along the thermite reaction pathway, an intermetallic reaction may occur when the two metals co-exist under fuel-rich conditions in the system. When only intermetallic reaction is considered, the exothermic energy may be insufficient to sustain reliable combustion in delay elements. It is possible to lower the reaction temperature through the combination of these two approaches into a ternary system. However, the thermite and intermetallic compositions should be chosen carefully. For a fast-burning delay system, the lowering of adiabatic reaction temperature could be dependent on the mass proportion of intermetallic composition required to undergo a self-sustained and self-propagation combustion. For a slow-burning delay system, adding a thermite may boost the exothermicity of the intermetallic and hence a sustainable combustion could occur. Hence the requirement of a slow combustion rate for a composition is that the reaction should occur with a very high activation energy and a relatively low exothermicity (Focke et al., 2019).

Another problem is that some commercial pyrotechnic compositions contain heavy metal-based oxides, such as lead oxides and barium sulphate or chromate, which are deemed environmentally unfriendly and hazardous to health (Tchounwou et al., 2012). This has led to the growing health and safety legislative requirements and greater efforts to explore “green” replacements for these compounds (Steinhauser and Klapötke, 2008; Sabatini, 2014; Ma et al., 2020). However, commercial mine detonators currently continue to rely on heavy metal-based pyrotechnic time

delays. Therefore, the less toxic heavy metals, e.g. Al, Ni, Sn, W, Bi and probably Mn, should be preferably employed when designing and creating a new pyrotechnic composition.

1.2 Aims and Objectives

The aim of this dissertation was to find a possible approach to reduce the reaction temperature or boost the exothermicity of environmentally benign compositions. These systems combined a classic thermite reaction with a standard intermetallic reaction or reactions between different oxides. Based on the classic example of a thermite Al-Fe_2O_3 system, aluminium is a more attractive metal as it is non-toxic at low levels of exposure, safe, environmentally acceptable, low cost and readily available in a variety of particle shapes and sizes. Apart from Fe_2O_3 as an oxidiser, other metal oxides are also used in pyrotechnic delay compositions such as CuO, WO_3, MoO_3 and NiO. Sometimes, polymers are also selected (i.e. Viton B and PTFE). However, they feature a very high heat of combustion of -31 $MJ \cdot kg^{-1}$ (Wang et al., 2011). The characteristics and combustion mechanism of an Al-NiO binary system with micro- and nano-sizes are well established, and factors affecting the combustion rate are investigated, such as the particle size, stoichiometry, compaction density, additives and different materials of tube wall (Bohlouli-Zanjani et al., 2013; Dean et al., 2010). The ignition process is driven by a liquid-gas mechanism for a micro-scale thermite and the reaction is essentially gasless (Fathollahi and Azizi-Toupkanloo, 2019). In addition, the reactive intermetallic Al-Ni system has received considerable attention in which diffusion plays a dominant role (Morsi, 2001). A linear combination of pure Al-NiO thermite and Al-Ni intermetallic is a possible way to modify the reaction temperature and combustion behaviours.

Manganese-fuelled pyrotechnic compositions are attractive due to their metallic properties and multiple oxidation states of oxides. A medium-to-slow combustion rate is provided by the combination of manganese as a fuel with different oxidisers such as Bi_2O_3, MnO_2, Cu_2O, and V_2O_5 (Swanepoel et al., 2010). Sustained combustion was observed for the Mn-Bi_2O_3 binary system at 40 – 60 wt-% fuel contents, and a faster combustion rate was observed at ca. 22 $mm \cdot s^{-1}$. However, the bismuth oxide was prepared by the thermal decomposition of bismuth (III) subcarbonate and not the raw material directly from the manufacturer. Very little information is available in the literature on the Sn-Bi_2O_3 binary system. Only gassy Sn-fuelled binary systems coupled with oxidizers such as KNO_3, $KClO_3$ and $KClO_4$ were found (Hosseini et al., 2011). Regarding environmental friendliness and heath safety, inorganic tin compounds feature a very low toxicity in animals mainly due to their generally low water solubility, poor absorption and a

low tendency for accumulation in tissues and rapid excretion (Howe and Watts, 2005). In the pre-experimental tests in the open air, the combustion behaviours of compositions containing Sn and Bi_2O_3 were not self-sustained and they died out before reaching the end of the length. A ternary pyrotechnic delay composition brought about by adding pure Mn-Bi_2O_3 binary thermite to Sn-Bi_2O_3 binary systems may modify the combustion performance compared to each binary system.

Two ternary pyrotechnic time-delay compositions were therefore prepared through the brush-mixing method and then tapped into borosilicate glass tubes with different inner diameters to construct the time-delay elements. At the same time, an experimental study of the time-delay compositions tapped in the lead tubes was conducted, in which the delay elements were constructed via a rolling process. The details of the two ternary systems are as follows:

(i) Aluminium (Al) – Nickel oxide (NiO) with Al – Ni system.

(ii) Tin (Sn) – Bismuth oxide (Bi_2O_3) with Manganese (Mn) – Bismuth oxide (Bi_2O_3) system.

The characteristics of these ternary compositions were determined by SEM, a particle size analyser, BET, XRD, XRF and a bomb calorimeter. Thermodynamic simulations were calculated using EKVI software. The combustion rates of these time-delay elements were measured through an assembled structure containing a digital camera and holder.

1.3Outline of the Thesis

This thesis is organised in five chapters and the outline is shown in **Figure 1-1**.

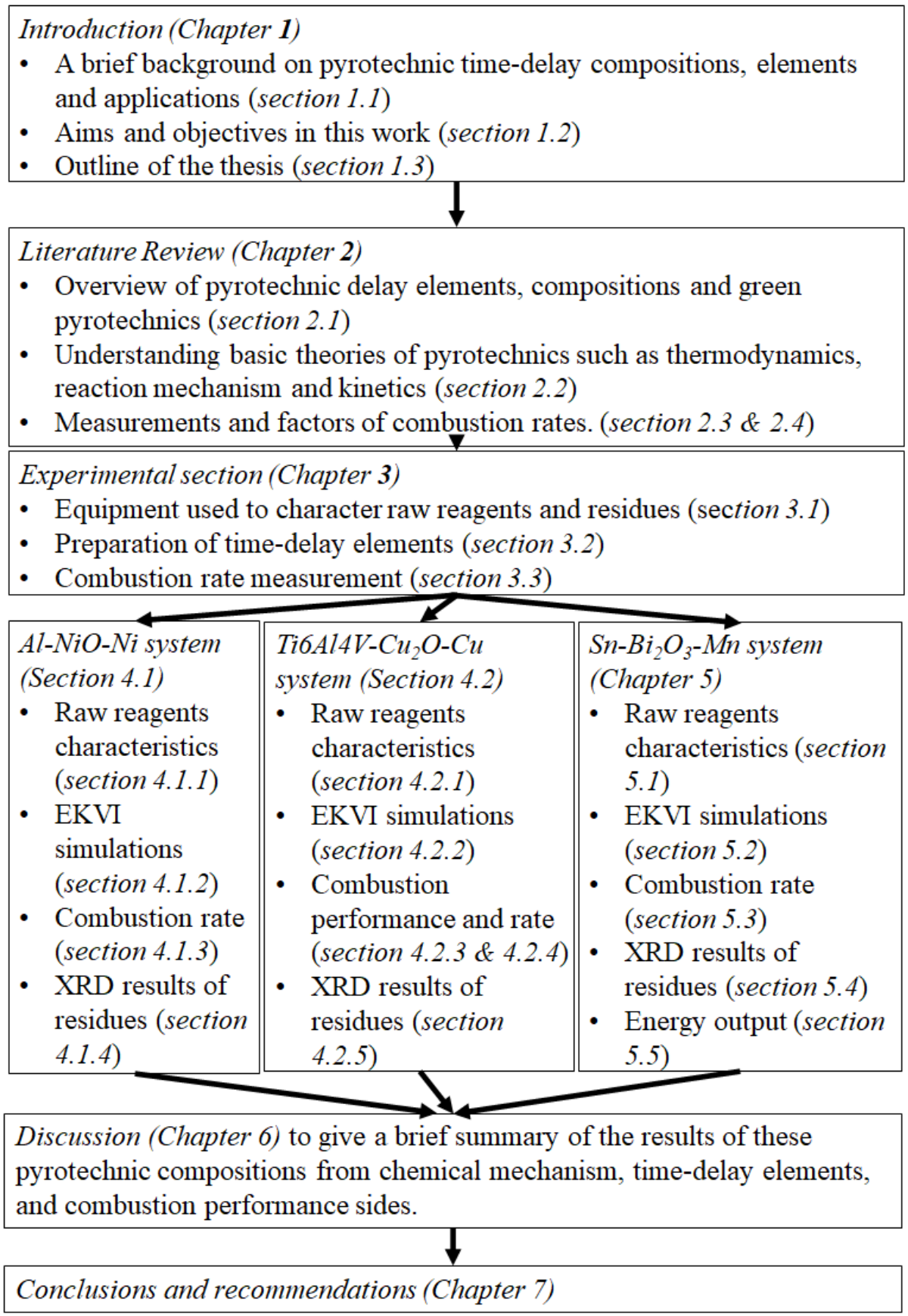

Figure 1-1： Schematic overview of this thesis

2. LITERATURE REVIEW

2.1Pyrotechnics

The term pyrotechnic is derived from the Greek words "*pyr*" and "*techne*", and briefly means "an art or science of fire" (Ellern, 1961). It was defined comprehensively by a German working group (Treumann, 1975) in the 1970s which states that pyrotechnics is a science or art that produces desired functional effects by an exothermic chemical reaction of single substance or mixtures, such as the desired sound, heat, light, fog, smoke, gas or incendiary. Ellern (1961) also defined pyrotechnics and emphasised that it was an exothermic chemical reaction of mixtures of solid compounds characterized as non-explosive and relatively slow, self-sustaining and self-contained, with some exceptions. Pyrotechnic compositions are used in both military and civilian applications (Ellern, 1968; McLain, 1980). Pyrotechnic compositions are normally divided into gassy and gasless (relatively) systems based on the amounts of gaseous products released during combustion in unconfined or confined columns. So-called gasless compositions are those systems in which the volume of products generated is less than 10 $mL \cdot g^{-1}$ (Charsley et al., 1980). It should be noted that "gasless" compositions are preferred in confined environments for time delay applications.

Gassy pyrotechnic compositions are used in applications such as gas generators. The volume of gas produced from these pyrotechnic compositions depends on the type of reagents and the variations in ratios used. For example, a composition comprised of potassium nitrate, magnesium-aluminium powder, an additive and an adhesive produced gases in the range of 4.84 – 7.56 $L \cdot g^{-1}$ (Li et al., 2015). Gas volumes as high as 300 $mL \cdot g^{-1}$ have been reported during the combustion of the well-known black powder composition (Ellern, 1968). Other notable commonly used gassy pyrotechnic compositions include $B_4C/NaIO_4$/PTFE (Shaw et al., 2015a), $Si/Bi_2O_3/Sb_2O_3$, Ti/C-3Ni/Al (Poret et al., 2014), and Al/copolymer (Grobler et al., 2018).

A major drawback associated with the use of gassy pyrotechnic time-delay compositions is that the varying pressure formed by the gaseous products would change the burning rates dramatically. It has been widely known empirically that the burning rates of gassy energetic materials, including pyrotechnics increase exponentially with increasing operational pressure, and tend to be extinguished in low-pressure environments (Kosanke, 2004). The delay times become inconsistent, making these unsuitable for applications requiring precisely accurate

time intervals. Therefore, gasless pyrotechnic time-delay compositions would be necessary to attain sustainable, reproducible linear burning rates.

2.1.1 Pyrotechnics delay elements

Delay detonators (electric or non-electric type) are commonly employed in modern explosive applications such as mining, quarrying and other blasting operations (Beck and Flanagan, 1992). Upon the initiation of the explosive charges, speedy explosion occurs, accompanied by fragmentation, throw of the rock being blasted, ground vibration and air blast noise. The sequential timing and initiation of the main explosive charges notably reduce the ground vibration and noise. The delay time interval between the sequential and successive combustion procedure is in a range from a fraction of a millisecond to several seconds.

Configuration. A typical structure of a pyrotechnic time-delay element is illustrated in **Figure 2-1** along with its position as commonly employed in non-electric detonators (Tsang, 2005). It is noted that, based on the function of the individual group, the detonator can be divided into three zones, namely the ignition source, the delay element and the output charge. Delay detonators consist of a metallic tube (typically aluminium, lead, etc.) in which pyrotechnic delay compositions are compressed. One end of the element is connected to an ignition source (a shock tube, for example), and the other end is in contact with heat-sensitive output charges (primer and base charge, such as lead azide and pentaerythritol tetranitrate, respectively). The shock tube is segregated from delay compositions by an antistatic cup which prevents any potentially incidental initiation which might be ignited by an electrostatic discharge. The cup is easily broken by the shock wave as it enters the detonator. Typically, a small amount of the delay composition is replaced with the starter composition to ensure reliable ignition of the main delay compositions. On ignition of a shock tube, the hot particles and gas enter the delay chamber and then ignite the starter composition. Then the initiating signal is transmitted to the main delay composition and successive layer-by-layer combustion occurs. The delay time interval is essentially the time it takes between the initiation of the starter composition and the ignition of the primary explosives at the end of the delay element.

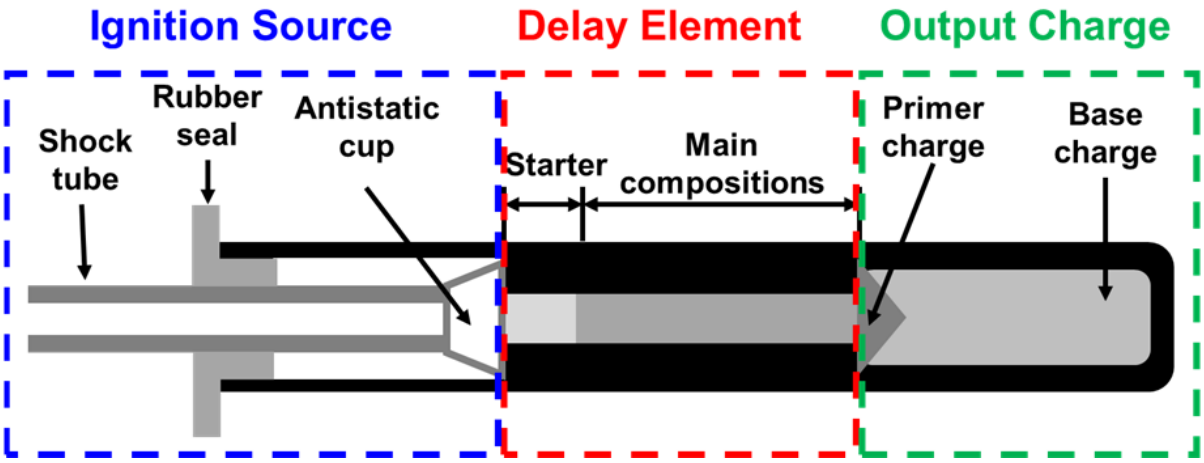

Figure 2-1: Typical structure of a pyrotechnic time-delay element along its position as commonly employed in non-electric detonator trains

Requirements. Some requirements that should be considered when creating and designing a pyrotechnic delay element are detailed as follows:

- Delay elements must be economically feasible to manufacture.
- Delay elements must be safe to handle from a health and safety point of view.
- During storage and transportation, delay elements should be resistant to moisture and deterioration.
- Geometric parameters of a designed delay element must be adaptable over a wide range of applications, especially for a limited space available inside a detonator shell (Davitt and Yuill, 1983; Beck and Flanagan, 1992).

Manufacturers. McLain (1980) discussed two methods of the general processing procedure and equipment employed for a pyrotechnic delay element. In the first manufacturing method, the delay compositions are compressed into zinc, aluminium or brass tubes with the desired geometry, and then the tubes can be slid into the detonator shell. The thickness should be sufficient to withstand the consolidating pressure in order to ensure that the delay element is rigid. In the second method, the delay compositions are filled into a lead tube and then the tube is drawn down to the desired diameter using a rolling machine. Thereafter, the rolled lead tube is cut to the required length (Fordham, 2013). It should be noted that lead-based detonators are in the process of being phased out since they pose considerable health and environmental risks. While zinc or aluminium tubes are considered as suitable alternatives, the heat-sink effect of these materials may cause quenching of the exothermic reaction along the column axial direction (Beck and Flanagan, 1992). In addition, the delay compositions have to be made into a free-flowing form for either the aluminium or lead tube method. This

free-flowing form can be attained through granulation or spray drying. Furthermore, the ease of ignition as well as the repeatability of the combustion velocity of the compositions are affected by the thermal conductivity and the extent of solid-solid contact. With this in mind, the packing density of the composition inside the delay element must be controlled. Uniform increments of delay composition must be added into the column, and pressed under an accurate pressure condition (Fordham, 2013).

Ignition. There are several ways to ignite the delay compositions compressed in a delay element, and various methods have been detailed as follows:

(i) *Black powder safety fuse.* (Kelly et al., 1975).

(ii) *Detonator cord.* A detonator cord consisting of a plastic tube filled with pentaerythritol tetranitrate has been used commercially as a reliable ignition source (Thureson and Gladden, 1988).

(iii) Nichrome wire and fuse head. A nichrome wire inserted in the end of a delay element receives the electrical power and then heats up to the ignition temperature of the composition (Kappagantula et al., 2011). A fuse head contained in an electric trigger delivers a 5 A current to a delay element and then ignites the delay composition (AI-Kazraji and Rees, 1979).

(iv) Shock tube. A shock tube is used to transport the initiating signal to explosive charges, and consists of a plastic tube (typically polyethylene) with an inner and outer diameter of 1.3 mm and 3 mm, respectively; a small amount of reactive material which conventionally refers to a composition of thin layer of aluminium and octahydro-1,3,5,7-tetranitro-1,3,5,7-tetrazocine (HMX) compositions is coated on the inside of the tube (Brent and Harding, 1993).

(v) Laser beam irradiation (in the future). Laser beams as a source of ignition are attractive for researchers and a single laser ignition source could reduce the possibility of accidental ignition (Danali et al., 2010; Granier and Pantoya, 2004; Ahmad and Russell, 2005; Ahmad and Russell, 2008).

2.1.2 Time-delay compositions

Suitable pyrotechnic compositions employed in non-electric delay detonators provide a self-sustained and self-propagated successive combustion performance, and they consist generally of fuels and oxidisers which remain in the powdered solid state. Conventional pyrotechnic compositions generally refer to intimate mixtures whose components are capable of a highly exothermic oxidation-reduction but non-detonation reaction (Klapötke, 2022). Pyrotechnic compositions should be ignitable yet safe from the storage, usage, transportation and health points of view (Beck et al., 1984). A wide range of fuels and oxidisers have been used to develop pyrotechnic compositions with varying time delay effects. **Table 2-1** summarises some of the common combinations available in the literature. It is worth noting that the fuels can be subdivided into metals, metal alloys and metalloids, while the oxidisers can be subdivided into metal oxides, oxy-salts and organic polymers.

Binders. During the manufacturing process of pyrotechnic compositions, it is sometimes necessary to add small amounts of binders to the pyrotechnic system in order to improve contact between the reagent particles and impart some mechanical properties to the granules. Both inorganic and organic compounds are typically used as binders. Examples of inorganic binders include water glass, gypsum and bentonite. Common types of natural and synthetic organic binders are Arabian rubber and acaroid resin for natural binders, dextrin and starch for semi-synthetic binders, and polyvinyle chloride (PVC), Viton B and polynitropoly-phenylene (PNP) for synthetic binders. Synthetic polymetric binders enhance the mechanical strength, reduce the amount of moisture adsorbed and improve the homogeneity of the mixtures (Focke et al., 2019; Berger, 2005).

Table 2-1： Fuels and oxidants commonly used in pyrotechnic compositions published in the open literature

Fuel	Oxidiser	Reference
Metal		
Al	**Metal-oxide** (MoO_3, Fe_2O_3, SiO_2, CuO, WO_3); **Fluoropolymer Viton B**; **Salts** ($KMnO_4$)	(Danali et al., 2010; Gibot et al., 2011; Sanders et al., 2007) (Potgieter et al., 2016) (Fathollahi and Behnejad, 2015)
Mg	**Metal-oxide** (CuO, Fe_2O_3); **Fluoropolymer** (PTFE); **Salts** ($KmnO_4$, $Ba(NO_3)_2$)	(Pourmortazavi et al., 2008; Monogarov et al., 2019) (Chen et al., 2012) (Fathollahi and Behnejad, 2015; Ouyang, 2013)
Mn	**Metal-oxide** (MnO_2, Bi_2O_3, V_2O_5, Cu_2O, BaO_2, SrO_2)	(Swanepoel et al., 2010; Miklaszewski et al., 2014a; Drennan and Brown, 1992)
Fe	**Metal-oxide** (BaO_2, SrO_2); **Salts** (KNO_3, $KclO_4$)	(Tribelhorn et al., 1995a) (Gillard, 2007)
Zn	**Metal-oxide** (BaO_2, SrO_2)	(Tribelhorn et al., 1995b)
W	**Metal-oxide** (Sb_2O_3, MnO_2,) **Salts** (KIO_4)	(Poret et al., 2013; Koenig et al., 2017)
Ti	**Metal-oxide** (CuO, MoO_3, BaO_2); **Salts** ($Sr(NO_3)_2$, $KclO_4$, $BaCrO_4$)	(Zhu et al., 2011, Laye and Charsley, 1987)
Zr	**Metal-oxide** (Fe_2O_3,)	(Han et al., 2019; Ebrahimzadeh and Ziarati, 2020)
Alloy		
Al-Mg	**Salts** ($KmnO_4$)	(Fathollahi and Behnejad, 2015)
Mg-Zn	**Fluoropolymer** (PTFE)	(Zhao et al., 2022)
Zr-Ni	**Salts** ($KclO_4$, $BaCrO_4$)	(Han et al., 2020)
Metalloid		
B	**Metal-oxide** (CuO, Fe_2O_3, Pb_3O_4, Bi_2O_3, **Salts** ($K_2Cr_2O_7$, $BaCrO_4$, $SrMoO_4$, $BaMoO_4$)	(Li et al., 2018; Elischer et al., 1986; Li et al., 2010; Huang et al., 2019) (Howlett and May, 1973; Walters and Groven, 2019)
Si	**Metal-oxide** (Pb_3O_4, SnO_2, Fe_2O_3, Bi_2O_3, MnO_2, PbO, Sb_2O_3); **Salts** ($BaSO_4$, $CaSO_4$, $KclO_3$, $KmnO_4$, $PbCrO_4$)	(Jakubko, 1997; Moghaddam and Rees, 1981; Rugunanan and Brown, 1991; Ricco et al., 2004; Tichapondwa et al., 2015)
Compound		
MgSi	**Viton B**	(Potgieter et al., 2016)
System		
$B_4C/NaIO_4$	**PTFE**	(Shaw et al., 2015)
Ti/C	3Ni/Al	(Miklaszewski et al., 2014b)

Additives. With a view to fine-tuning the compositions and creating a desired result, additional substances can be added to the composition, resulting in binary systems being converted to ternary systems. The optional additives can be inert or chemically active and function as processing aids, thermal insulators, fluxing agents, heat sinks, sensitisers or catalysts within the primary compositions. Normally, the presence of additives affects the activation energy of components, the heat of reaction or the energy feedback from the flame propagation front (Kosanke, 2004). The following are some examples of these additives:

- Processing aids: fumed silica (Tulis, 1980), carbon nanotubes (Ren et al., 2010), nanodiamonds (Pichot et al., 2015), graphite (Poret et al., 2013) and waxy lubricants (Shaw et al. 2012; Poret et al., 2013). These additives are used to improve the processing and preparation of various pyrotechnic compositions. However, this improved processability is often accompanied by changes in the burning rates and it is important to take this into account when formulating pyrotechnic delay compositions. Addition of 1% fumed silica to silicon-based binary systems, resulted in free flowing compositions which enabled efficient delay element filling. A slight decrease in the burning rates was observed as a result of the presence of the inert fumed silica (Tulis, 1980). Adding variable amounts of carbon nanotubes to Si powder during the ball milling process increased delay precision and burning rates in Si-Pb_3O_4 binary systems (Ren et al., 2010). A study by Pichot et al. (2015) revealed that it was safer to mix Al with Bi_2O_3 coated with nanodiamonds as they reduced friction in this system compared to the binary composition without nanodiamonds. However, this was accompanied by a 50% decrease in flame front velocity. Addition of 2% graphite to the W-Sb_2O_3-KIO_4 ternary system alleviated the abrasiveness caused during the pressing process (Poret et al., 2013). Addition of 1 – 5% waxy lubricants (calcium stearate or stearic acid) to W-Sb_2O_3-KIO_4 and B_4C-KNO_3-KCl ternary systems resulted in improved packing densities. The burning rates of the W-Sb_2O_3-KIO_4 compositions reduced by half upon calcium stearate addition. This was attributed to the formation of an insulating wax layer by the molten calcium stearate ahead of the burning front (Shaw et al. 2012; Poret et al., 2013).

- Fluxes: metals or metal compounds, which melt at a lower temperature than the burning temperature, such as V_2O_5, Sb_2O_3, Sb_2O_5, Na_2SO_4 (Beck and Flanagan, 1992; Beck and Brown, 1986b).

- Heat sink: calcium stearate (Poret et al., 2013) and shellac (Han and Yan, 2014).

- Catalysts: substances can lower the ignition temperature such as MnO_2, Fe_2O_3, V_2O_5, CuO, and CrO_2 (Beck and Flanagan, 1992; Kosanke et al., 2004).
- Sensitizers: the heat produced by the substances reacted before the dominant reaction is required to initiate the dominate reaction, such as Si-Bi_2O_3 composition (Ilunga et al., 2011).

Pyrotechnic time-delay compositions are a small part of the pyrotechnic world, and a key characteristic parameter is the delay time intervals. Delay time intervals refer to a measured combustion time which is provided by the combustion process in a specific length of column for a delay formulation – values vary from a few milliseconds to several minutes. Thus, it depends on the delay compositions selected and the length of the delay columns. The general requirements of time-delay compositions are summarised as follows:

- Mixtures consisting of suitable fuels and oxidants which stay in the form of solid powders and should be inexpensive and available.
- Compositions should be ignitable and non-hygroscopic, but sufficiently safe and stable during storage and transportation.
- The typical reaction should be an exothermic redox reaction.
- Combustion should be "gasless" with none or less than 10 $cm^3 \cdot g^{-1}$ gaseous products generated along the combustion pathway (Charsley et al., 1980).
- Combustion should be favourable for manufacturing and preparation of delay elements, such as good flow property for the filling process.
- Residual products should be benign to the environment and health.
- The combustion rate should be constant and reproducible in order to obtain a reliable delay time interval.

The main factor which influences the combustion delay time interval is the combustion rate. This is affected by multiple factors such as particle size and shape, the mass ratio of fuels/oxidants, additional substances, temperature, pressure, and the physical and chemical properties of the components. The relationship between these parameters and the combustion rate can be theoretically established using analytical or numerical models under some assumptions. The advantage of using analytical modelling is that it reduces the resources needed to develop a new composition such as raw materials and equipment, while effective

prediction of the combustion rate and minimised safety risks in experimental testing are obtained from numerical modelling. In analytical modelling, assumptions are made based on the physical properties of the starting materials, possible reaction mechanisms and phase transitions (Khaikin and Merzhanov, 1966; Aldushin and Khaikin, 1974; Armstrong, 1990). The time-dependent variable can be eliminated through the mathematical method when using analytical modelling. However, time-dependent variables presented during the combustion propagation procedure can provide more information in order to increase the accuracy of predicted combustion front speed and temperature profiles. Numerical modelling is based on the temperature and concentration profiles obtained along the length of the delay element over time (Beck et al., 1984; Boddington et al., 1986; Boddington and La Ye, 1987; Boddington et al., 1989). Some analytical models and numerical models are summarised in **Table 2-2**. More detailed explanations of these models are presented in **Section 2.2.3**.

Table 2-2： Summary of mathematical models describing pyrotechnic delay elements

Key assumptions	Mathematical descriptions	References
Analytical models		
(1) Reaction only occurs in a thin reaction zone. (2) Physical properties are independent of concentration and temperature. (3) No phase transitions occur. (4) Arrhenius temperature dependence.	$u=\sqrt{\frac{\lambda k_0 R T_c^2}{\rho E_a h_{rx} g(n)} e^{-E_a/RT_c}}$	(Khaikin and Merzhanov, 1966) (Swanepoel et al., 2010)
(1) Compositions stacked in neat layers. (2) Growing layers of products provide medium for diffusion. (3) Particles are flat and reaction rate is controlled by parabolic law. (4) Arrhenius temperature dependence.	$u=\sqrt{\frac{6RT_c^2}{E_D(T_c-T_i)}\frac{\lambda A_0}{\rho C_p d^2} e^{-E_D/RT_c}}$	(Aldushin and Khaikin, 1974) (Armstrong, 1990)
(1) Solid reactants melt and form a homogeneous liquid mixture. (2) Order-based kinetic reactions. (3) Arrhenius temperature dependence.	$u=\sqrt{\frac{N\lambda k_0 R T_c^2}{\rho h_{rx} E_a} e^{-E_a/RT_c}}$	(Dunmead et al., 1989)
Numerical models		
(1) Reaction only occurs in a thin reaction zone. (2) Mass transfer effects are neglected. (3) Gasless reactions with planar propagation front. (4) A single heat source is the heat generation. (5) Heat loss only occurs through convection and radiation.	$\rho h_{rx}\frac{d\alpha}{dt}+\frac{\lambda}{u^2}\frac{d^2T}{dt^2}-q_L(T-T_i)=\rho C_p\frac{dT}{dt}$	(Beck et al., 1984; Boddington et al., 1986; Boddington and La Ye, 1987; Boddington et al., 1989; Dunmead et al., 1989)

2.1.3 Green pyrotechnics

Green chemistry was initially introduced by the US Environmental Protection Agency in the 1990s. The definition can be found on their website (EPA) and it noted that the reduction or elimination of hazardous or poisonous substances generated can be achieved through the

design, development and implementation of chemical products and processes. Green pyrotechnics are designed and created on the basis of the Twelve Principles of Green Chemistry (Paul et al., 1998). Growing numbers of academic articles have been focusing on environmentally benign pyrotechnic delay compositions (Poret et al., 2012; Miklaszewski, 2014a; Koenig et al., 2017; Walters and Groven, 2019). Traditionally, pyrotechnic formulations still contain some compounds associated with significant human health and environmental concerns. The current inventory of main contaminants is as follows:

- ***Lead (Pb) compounds***: Lead is a priority pollutant listed by the Environmental Protection Agency (EPA). Exposure to lead adversely affects various systems of human bodies, such as the nervous system, kidney function, immune system, reproductive and developmental systems, and the cardiovascular system. Additionally, lead bioaccumulates in bones and soft tissues (EPA). Currently, lead is found in pyrotechnic compositions in the form of lead oxide (such as PbO, PbO_2 and Pb_3O_4), lead(II) chromate or nitrate which are used for all kinds of pyrotechnic and technical initiations applications (Alenfelt, 2000; Barkley, 1978).

- ***Barium (Ba) compounds.*** Barium compounds containing the cation of water-soluble barium (II) (such as $BaCl_2$, BaO and $Ba(OH)_2$) are highly poisonous and possible products obtained after combustion of pyrotechnics can cause cardiotoxic and bronchoconstriction effects after being inhaled (Hicks et al., 1986).

- ***Chromates.*** The toxicity of chromates are significantly dependent on the oxidation state of the ion; the most toxic and carcinogenic of compounds contain Cr(VI) compared to the metallic Cr, Cr(II) and Cr(III) (Sukumar and Subramanian, 1992; Rossol, 2001). Cr(VI) found in the scalp of Indian factory labours was identified as the cause of headaches and dizziness (Sukumar and Subramanian, 1992). Exposure to strontium chromate has been also been identified as one of the most potent animal carcinogens (Rossol, 2001).

- ***Perchlorates***: The perchlorate ion is teratogenic and has a negative effect on thyroid gland function as it inhibits the uptake of iodide by the thyroid gland (Urbansky, 2000; Sijimol and Mohan, 2014).

Therefore, concerted efforts have been made to look for greener replacements for these hazardous or poisonous components used in pyrotechnic delay compositions. While the development of alternative “green” pyrotechnic compositions might cause significant

financial pressure, support from local government or other external organisations is the key. The alternatives should be non-toxic and require comparable processibility, safety and performance effectiveness based on corresponding to traditional pyrotechnics. The utilisation of nano-scale thermite materials (metastable intermolecular composites or MICs) for the lead-free electric matches employed in pyrotechnic initiation has recently been increasing in the past studies (Naud et al., 2003; Son et al., 2002). Miklaszewski et al. (2014) and Koenig et al. (2017) selected manganese dioxide as a replacement for perchlorates or chromate (i.e. $BaCrO_4$ and $KClO_4$) that were coupled with manganese or tungsten fuels. These simplified binary formulations showed low toxicity, produced very little gas, achieved low-combustion velocity and presented good aging characteristics (Miklaszewski et al., 2014; Koenig et al., 2017). Anhydrous calcium sulphate has been proposed as a possible oxidant replacement for barium sulphate in binary slow-burning pyrotechnic delay systems in which silicon was used as a fuel. It was determined that the reactants as well as the products were environmentally benign (Tichapondwa et al., 2015). The possibility of using a molybdate cation to replace chromate was investigated when combined with strontium, and a high degree of configurability for a novel approach was constructed in which delay formulation was integrated into printable ink and deposited onto soapstone substrates (Walters and Groven, 2019).

2.2Basic Theories of Pyrotechnics

This section reviews the basic theories of the following parameters in pyrotechnic composition design: thermodynamic principles, reaction mechanisms and kinetics.

2.2.1 Thermodynamic principles

Thermodynamics of condensed phase reactions. Gasless pyrotechnic delay compositions undergo oxidation-reduction reactions between the fuels (metallic or non-metallic) and oxidants selected in the systems. In these systems, combustion is mainly confined to the condensed state (solid or liquid). The raw materials chosen are originally in a solid state in most cases while the liquid state is obtained when some constituents melt before or during the initiation of an exothermic reaction. Since the combustion of pyrotechnic gasless compositions is highly exothermic and irreversible, the Gibbs free energy change of the reaction ($\Delta G_R = \Delta H_R - T\Delta S_R$) should be negative at a constant temperature and pressure. This is in line with the spontaneity of pyrotechnic reactions as they obey the second law of thermodynamics. The entropy changes of commonly crystalline solid products generated from the chemical reaction are usually very small, as well as the sum of the atomic specific heats being maintained in a constant based on Kopp's rule. Hence the approach of ensuring a large ΔG_R is only dependent on the absolute value of enthalpy changes ΔH_R which refers to a highly exothermic reaction to some extent. Detailed thermal characterisation studies for nano- and micro-Al/NiO binary systems published by Fathollahi and Azizi‐Toupkanloo (2019) established that the thermite reactions were highly exothermic and the Gibbs free energy change of reactions were all negative. Kosanke et al. (2004) also listed the thermal properties of some commonly used pyrotechnic compositions and they all featured negative Gibbs free energy change of reactions.

Ellingham diagram. The Ellingham diagram is a significant graph which provides a preliminary way to evaluate the thermodynamic feasibility of a potential driving force for a proposed exothermic reaction (Ellingham, 1944), and in which the standard Gibbs energy of formation of the non-metallic and metallic oxide varies with various temperatures. The location of the plotted lines in the Ellingham diagram indicates the relative ability of the metallic elements combined with oxygen. At the same time, this also provides a rapid way of evaluating the reducibility for a given oxide or sulphide. **Figure 2-2** illustrates an example of an Ellingham diagram for several metallic elements which reacted with oxygen gas under

various temperatures (Kumar, 2008) and an extended investigation of known manganese oxides shown in the right window (Swanepoel et al., 2010). The standard oxidation-formed pathway of a metallic element is written as follows:

$$(2x/y)M + O_2 \rightarrow (2/y)M_xO_y \tag{2-1}$$

When considering the family of manganese oxides and their pathways shown in **Figure 2-2**, four common manganese oxides (MnO, Mn_2O_3, MnO_2 and Mn_3O_4) are formed based on the content of oxygen gas presenting in the oxidation. A surprising thermite reaction (Mn + $MnO_2 \rightarrow$ 2 MnO) is a net reaction for the mathematical calculation of oxidation reactions (a) and (d) under the same conditions based on Hess's law. At a given temperature, the Gibbs free energy changes of the thermic reaction (ΔG_R°) is equal to the calculated value of the standard Gibbs energy of formation of these two reactions at the same mathematical rules (Swanepoel et al., 2010). Apart from the evaluation of the Gibbs free energy of the thermite reactions, a greater stability and lower reducibility of a specific oxide is indicated by the plotted lines located lower down.

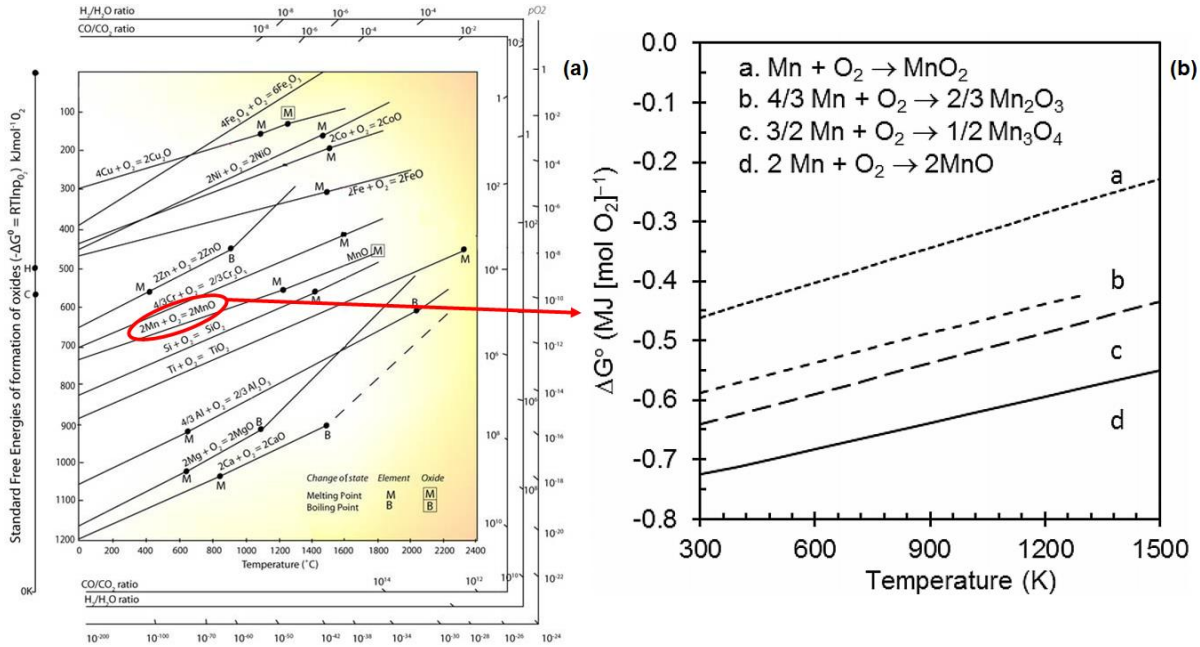

Figure 2-2： (a) An example of an Ellingham diagram (Kumar, 2008); (b) Ellingham diagram for an extended investigation of known manganese oxides at an ambient pressure of 0.1 MPa (Swanepoel et al., 2010)

Adiabatic reaction temperature. For the combustion behaviour of a pyrotechnic gasless delay element, the flame temperature and the driving force (the evolution of heat from exothermic reaction itself) must be high enough to maintain the combustion front of a self-sustaining reaction under conditions of constant pressure and no energy transfer between the delay

element and the surrounding (Munir and Anselmi-Tamburini, 1989). The adiabatic flame temperature (T_{ad}) is a significant thermodynamic parameter and it refers to a reaction temperature which is generated only by heat from the reaction under adiabatic conditions along the reaction front. Considering the phase states of the reactants and the fact that the products remain in a condensed state, including solid and liquid states, the evaluation of the adiabatic flame temperature for an irreversible reaction (a binary reaction as an example: $A_s + B_s \rightarrow C_s$) can be obtained by the following steps (Focke et al., 2019):

(i) Assumption step: The only phase change is melting of the constituents during the combustion procedure – the initiation temperature of the reaction is precisely chosen (T_i, typically 298 K). The constituents of the compositions remain in a solid state before the ignition.

(ii) T_{ad}-calculated step: The only force driving the self-sustaining reaction forward is the heat of the reaction, which is approximately equal to the enthalpy change of the reaction including the enthalpy changes of the phase change. The calculation of the adiabatic reaction temperature is generally written in a definite integral equation as follows:

$$\Delta H_R = \int_{T_i}^{T_m} C_{p_s} dT + \Delta H_m + \int_{T_m}^{T_{ad}} C_{p_l} dT \tag{2-2}$$

(iii) T_{ad}-calculated simplified step: Assuming that no phase changes occur and the physical properties of the constituents can be noted as a constant and they are independent of the conversion of the reagent, equation 2-2 is re-written as follows:

$$T_{ad} = T_i + \left(-\Delta H_R\right) / C_p \tag{2-3}$$

In equations 2-2 and 2-3, ΔH is the enthalpy changes; the subscripts R and m are associated with the reaction and the melting of the products, respectively; C_p is the heat capacity; and the subscripts s and l refer to the solid and liquid state of the products, respectively. For most actual combustion of pyrotechnic compositions compressed in delay elements, enthalpy changes of the reaction should be frequently corrected when equation 2-3 is used.

2.2.2 Reaction mechanism

The reaction mechanisms of solid particles which undergo an overall exothermic redox reaction are still much debated. Typical pyrotechnic redox reactions take place in solid-solid, solid-liquid or solid-gaseous states (Berger, 2005). When deducing the real reaction

mechanism of a pyrotechnic system, some experimental data should be detected such as phase changes, the intermediates and the products generated from the selected reagents, and temperature profiles along the reaction procedure. Hence, two types of analytical techniques should be commonly carried out for a given composition. Thermal analysis provides phase transitions and energy changes under controlled conditions, and these techniques include differential thermal analysis (DTA), thermogravimetric analysis (TGA), differential scanning calorimetry (DSC) and bomb calorimetry. The post-products can be analysed through X-ray diffraction (XRD), X-ray fluorescence (XRF), and infrared spectroscopy (IR). The morphology and element analysis can be analysed through optical microscopy and scanning electron microscopy (Dunmead et al.; Laye and Charsley, 1987). However, few problems can arise during these analytical techniques, which are as follows (Tribelhorn, 1994):

- For a high-temperature pyrotechnic system, thermal analysis which takes place under controlled conditions cannot accurately interpret the reaction procedure; slow-burning and secondary reactions may occur under controlled conditions at a slow heating rate.
- Measured data are obtained by testing the post-products which were collected after the combustion of pyrotechnic compositions, but not the actual products at a higher temperature.
- Products and intermediates identified via these techniques are not precise as many phase changes may be unknown at the actual reaction temperature. Amorphous states were shown in XRD spectroscopy. Therefore, not all phases can be drawn in the phase diagram.
- Inhibiting reactions between the product and the environment poses challenges. Exposure to ambient air can lead to the formation of various products, as demonstrated by the multiple reactions depicted in **Figure 2-2 (b)**. The presence of multiple oxidation states in manganese can result in the formation of a range of manganese oxides.

Solid state. The solids used in most pyrotechnic compositions are naturally polycrystalline, and their structure is characterised via their repeated unit cell or building block in which the constituent atoms are arranged in an ordered pattern. Crystalline structures are classified based on the types of bonding force, and the descending sequence is covalent, ionic, metallic, hydrogen and van der Waals. Furthermore, crystalline structures are characterised by the geometric symmetry of repeated unit cells and the closeness of their packing. The physical properties of a solid depend on the bonding forces and its crystal structure, namely:

- *Hardness.* The Mohs scale of mineral hardness is a qualitative ordinal scale that characterizes the scratch resistance of various minerals, and is generally divided into ten grades. Diamond (consisting of C-C covalent bonds) is the hardest material on the scale (Mohs hardness:10). Poly-crystalline cubic diamond obtained from the direct conversion of graphite at static high pressures and temperatures (Dubrovinskaia et al., 2005) also display ultra-hard behaviour. Metalloid boron (Mohs hardness: 9.5) consists of icosahedron units typically formed as a result of covalent bonds which give it its characteristic hardness. Boron has been used as a fuel in combination with various oxidisers such as Bi_2O_3, CuO, MoO_3, Fe_2O_3 and Co_3O_4 (Huang et al., 2019). Boron carbide, which also has a icosahedron crystal structure (Mohrs hardness: 9.3) was used as a cerimic fuel in gassy $B_4C/NaIO_4$/PTFE pyrotechnic compositions (Shaw et al., 2015a). Tungsten (strong metallic bonds between tungsten atoms) is a relative harder metallic fuel (Mohs hardness: 7.5) generally used in pyrotechnic delay compositions with various oxidisers, such as MnO_2 (Koenig et al., 2017), Sb_2O_3 and KIO_4 (Poret et al., 2013).

- *Melting point.* The stronger the bonding force in the crystal structure, the higher the melting point of the solids displayed in microscopic scale. This is generally applied for a pure substance, but the melting point of the substance with some impurities (even in a small amount) would become lower, which is typically the case in most industrial applications.

- *Decomposition temperature.* The higher the decomposition temperature of compounds, the more stable the solid compound remains and the stronger the bonding force present in the crystal structure.

- *Malleability and ductility.* The malleability and ductility of metals are better than those of other solids as the orientation of their bonding force is arbitrary and no bonds are ruptured under stretching or compressing (McLain, 1980).

The presence of crystalline imperfection, such as displacement, lattice defects, and grain boundaries of polycrystals, cause an inexact relationship between the physical properties of a solid and crystal classification based on chemical and geometric types. The chemical reactivity of a solid is dependent on these imperfections such as lattice defects, cracks and displacements, which lead to an increase in the surface area where the rate of adsorption, decomposition and solution increase (McLain, 1980). The classified defects affecting the reactivity of solids are listed as follows:

- *Inherent defects* (e.g. Schottky and Frenkel defects) occur when a vacancy at one site is formed by the absence of an atom or an atom is displaced from its site to the near-site, and these vacancies are not due to the presence of impurities.
- Non-stoichiometric defects (e.g. $Fe_{1-x}O$ and TiO_{2-x}) refer to the defects that deviate from the stoichiometric proportion between cations and ions, and they are produced by the exchange of matrix crystals with certain cations or ions in the medium. As the temperature increased, so did the amplitude of the vibrational motions at the average position increase.
- Crystal dislocations refer to an internal microscopic defect which is a local irregular arrangement of atoms. Dislocations are classified as edge dislocation or screw dislocation. It has been shown that the chemical stability near the intersection between a dislocation and surface is lower than the other parts of the surface due to the dislocation stress field. The strength of the material depends on the dislocation density and the lattice can deform or slip along the dislocation defect, resulting in plastic deformation.
- Grain boundaries are planar defects that are typically found in polycrystalline solids that consist of multiple crystals with different orientations separated by the internal grain boundaries. The energy of the atoms at the grain boundaries are higher and the diffusion rate is faster compared to the atoms inside the grains.
- Crystal dislocation and grain boundaries may result in a larger surface area, more edges and corners in solid materials. This in turn affects the properties and chemical reactivity of the solids. These defects can weaken the bonds between atoms, making them more susceptible to chemical reactions with liquids or gases that come into contact with the solid material.

McLain (1980) listed the factors influencing the chemical reactivity of solids as follows:

- *Hereditary structures:* The prepared ways of the materials and the history of the samples influence their further behaviours, such as introducing impurities or crystallisation in them. For example, sulphate-derived iron oxide (Fe_2O_3), with larger particle sizes and less crystallization shown in X-ray diffraction patterns, was much more reactive than Fe_2O_3 derived from iron oxalate.
- *Mechanochemical activation:* Mechanical treatment of the starting materials can be used to obtain smaller particle sizes and larger particle size distributions through milling,

atomising, pulverising and grinding processes. After these mechanical treatments, many atomic bonds can be broken down and many bonds on the newly created surfaces, edges and corners are much weaker than the internal bonds. Hence, this enhances the reactivity of the solid particles, as well as affecting the ignition properties and derivation of reaction mechanisms.

- *Doping and co-crystallisation:* Doping is an approach of introducing small amounts of impure elements or compounds to chemical materials or crystalline structures in order to modify some properties such as electric, magnetic or light effects. Doping $KClO_3$ with $Cu(ClO_3)_2$ or NiO with LiO_2 and Cr_2O_3 has a positive effect on the reactivity of $KClO_3$ or NiO, especially a spontaneous high-order explosion for compositions containing sulphur and $Cu(ClO_3)_2$-doped $KClO_3$. Another example is that doping with co-crystallisation of precursors makes iron oxide more reactive.

- *Passivating oxide surface layer:* The passivation oxide layer on the outer surface of almost all metallic particles provide protection against the oxidation reaction between pure metal and atmospheric oxygen, and also increases the contact state between the fuels and the oxidant particles in pyrotechnic compositions, which then leads to a higher ignition temperature. The thickness of the oxide layer has a major effect on the ignition temperature, especially for nanoparticles (Granier and Pantoya, 2004; Kwon et al., 2007).

- *Presence of water:* It is well known that water vapour present has a noticeable influence on the sintering, structural rearrangement and crystal coarsening of oxides which are attributed to the chemisorption that occurs on the surfaces and interfaces of the oxides. This then leads to an increase in the mobility of ions at these locations. Furthermore, water vapour is widely employed as a catalyst and accelerator in pyrotechnic reactions. The concentration should be controlled to less than 0.1 wt-% H_2O, otherwise, the reaction will be inhibited McLain (1980).

- *Corrosion inhibition:* Chemical treatment is commonly applied to lengthen the life of relatively reactive materials such as Al, Mg and Zn. Formation of oxide layer is one protective way against atmospheric moisture or contact with water. Sometimes it is also favourable for preventing hydrogen evolution during the wet mixing process (Tichapondwa et al., 2014).

Solid-solid reactions. Some of the major steps occurring in solid-solid reactions include nucleation, growth and transfer of matter. Diffusion plays a crucial role in the reaction

mechanism and its theory is made up of the basic explanation of solid-solid reactions. When considering the diffusion of the reaction between metal atoms and non-metal atoms, two possible mechanisms may occur based on the migration direction from the non-metal atom to the metal atom through the product layer or vice versa. When combining BaO_2 and SrO_2 as oxidants with iron, manganese or molybdenum fuels, diffusion via cation vacancies should be preferable in the BaO_2 lattice to that in the SrO_2 lattice due to the different radii of ionic species. The activation energies of these systems were similar to those of the Mn/SrO_2 and Mn/BaO_2 systems. For the same oxidant in a binary system under the same mass fraction of fuel or same-order mole ratio, a decreasing sequence of the combustion rates for compositions containing different metals was obtained in the following order: Zn, Fe, Mn, and Mo (Tribelhorn, 1994; Drennan and Brown, 1992; Tribelhorn et al., 1995b). Tribelhorn et al. (1995a) established that the higher the compaction pressure applied to a Fe-BaO_2 binary delay composition, the faster the combustion rates obtained. They attributed this to an increase in the interparticle contact area. Investigation of the combustion behaviour of the Zn-$KMnO_4$ binary system in the range of 30 – 75 wt-% fuel loadings and compacted under 50, 100 and 150 MPa, showed that Zn may diffuse into the K_2MnO_4 residue formed during the first stage of the decomposition of $KMnO_4$. The exothermic reaction between the Zn and this K_2MnO_4 residue started at 520 ℃ based on the thermal analysis results (Tribelhorn et al., 1995b). From the above observations, diffusion effects should be considered necessary when constructing models of the solid-solid reactions of pyrotechnic delay compositions.

Solid-liquid reactions. For fuels with a lower melting temperature than the ignition reaction temperature, the molten fuels will flow to the oxidant particles before ignition and increase the contact surface areas. Reactions would occur at the solid-liquid interface and propagate in the new liquid phase, and the transfer of matter and energy would determine the ignition and combustion processes. The surface tension of the liquid phase is a key parameter in solid-liquid reactions, and it determines the wettability of the granular reactants (Howlett and May, 1973). Compared to other metals with lower melting points, the surface tension of Zn at its melting point is higher and the movement of molten Zn through pores and channels would not occur readily when combined with the difficult-to-wet surfaces of oxidants (Tribelhorn et al., 1995b).

Solid-gas reactions. The gaseous source of pyrotechnic delay elements is mainly oxygen gas from the environment or the decomposition process of the oxidants, and the reaction mechanism would be a solid-gas reaction pathway because of the gaseous intermediates or

products. The void fraction of the delay column with a fixed geometry is the main factor affecting the reaction mechanism. When the composition is loosely packed in a delay column, a larger fraction of void volume is available for the convection of combustion products and hot air. An uncontrolled reaction rate is created and an explosion frequently occurs due to the rapidly increased pressure and heat in a confined column. For compositions in a consolidated state, the combustion reaction propagates in a thin reaction zone and the gaseous flow is strongly impeded. The reaction mechanism transitions to a solid-solid reaction if the bulk density tends towards the theoretical maximum density.

Tribelhorn et al. (1995b) observed a decrease in combustion rates with increasing compaction pressure for Zn-$KMnO_4$ and Zn-SrO_2 delay compositions. These compositions were postulated to undergo a solid-gas reaction mechanism where the zinc reacts with the oxygen gas released during the decomposition of the oxidants. Because of the multiple gaseous sources of Zn-Pb_3O_4 compositions, such as Zn and Pb vapours and the O_2 generated by the decomposition of Pb_3O_4, the reaction mechanism was much more complex than the other two zinc-fuelled compositions.

2.2.3 Kinetics

As reaction mechanisms are very complex and affected by diffusion and multiple steps, the kinetic analysis of pyrotechnic compositions in the condensed phase is also debatable. The reaction rate at the condensed state can generally be expressed as a function of temperature and conversion, which can be a product of two separable functions (one is dependent on the temperature and the other on the conversion of the reactants):

$$r = \frac{dx}{dt} = \Phi(T, x) = k(T) f(x) \tag{2-4}$$

This is a single-step kinetics approximation and is referred to as the general rate equation. Equation 2-4 is not only used in a single-step reaction, but also for controlled-step kinetics in a complex multiple-step reaction (Šimon, 2005). When considering the reaction constant k(*T)*, the conventional assumption is that the rate constant *k* follows simple Arrhenius kinetics:

$$k(T) = k_0 \, exp(-E_a / RT) \tag{2-5}$$

where k_0 and E_a are the pre-exponential factor and activation energy, respectively. Combining equations 2-4 and 2-5 results in the reaction rate expression presented in equation 2-6.

$$r = \frac{dx}{dt} = k_0\, exp\left(-E_a/RT\right) f\left(x\right) \tag{2-6}$$

Condensed phase reaction Kinetics. A "true" kinetic model cannot be presented by the single-step approximation but must fit all the experimental data under varying temperature conditions such as isothermal, linear heating rate and modulated temperature (Perez-Maqueda et al., 2006). A "true" complex reaction would be determined by Arrhenius kinetics at a low-temperature stage and the diffusion mechanism at a higher temperature where the rate could be independent of the temperature. The reaction constant can be written as follows (Laye, 1997):

$$k^{-1} = k_{Ar}^{-1} + \left(BT^n\right)^{-1} = \left[k_0\, exp\left(-E_a/RT\right)\right]^{-1} + \left(BT^n\right)^{-1} \tag{2-7}$$

where subscript "*Ar*" refers to Arrhenius kinetics and *B* is the diffusion coefficient.

Many solid-state kinetic models have been developed and classified based on mechanisms such as nucleation, geometric contraction and order-based diffusion and conduction (Montgomery, 2018). For pyrotechnic reactions, particle sizes and their distribution play a significant role in solid-state reactions (Koga and Criado, 1998). With the increasing development of mathematical analysis and conversion models, an empirical approximation equation is employed in most models and expressed as follows (Perez-Maqueda et al., 2006):

$$f\left(x\right) = x^m\left(1-x\right)^n \tag{2-8}$$

where superscripts "*m"* and "*n"* are adjustable constants. It is noted that this equation can be used for kinetic models by analysing any experimental data without any previous assumptions. For homogeneous kinetics (e.g. those reactions containing liquid or gas phases), a general reaction rate can be expressed based on an order-based reaction as follows:

$$r = \frac{dx}{dt} = k_0\, exp\left(-E_a/RT\right) x^m\left(1-x\right)^n \tag{2-9}$$

where k_0 and E_a are the pre-exponential factor and activation energy which are dependent on temperature; *R* is the gas constant; and *x* is the degree of conversion.

Elementary model for a cylindrical delay element. **Figure 2-3** shows a schematic of an elementary model for a typical experimental configuration of the delay element in a cylindric column. The following assumptions are the basis for the model and analysis:

- Geometry of a delay column: symmetrical and cylindrical body.
- Solid compositions: the order of the solid particle size is much less than the body. An approximation of continuum and homogeneity is assumed as the thin reaction zones where the local heat is transferred.
- Heat source: the only heat source of sustained combustion in the delay element is the heat of chemical reaction.
- Heat transfer: heat transfer takes place by the conduction within the body and by the difference in temperature between the surface and the external medium.
- Phase change: phase changes of the constituents such as melting and vaporisation are neglected.
- Properties: physical and transport properties should be assumed to be constant, for example heat capacity and bulk density are independent of temperature and conversion of the reactants.
- Temperature configurated: the temperature at the start surface of the cylinder at $z = 0$ is the same as the ignition temperature (T_*); the temperature at the end surface of the cylinder at $z \rightarrow \infty$ tends towards the ambient temperature (T_0); radial temperature gradients are neglected.

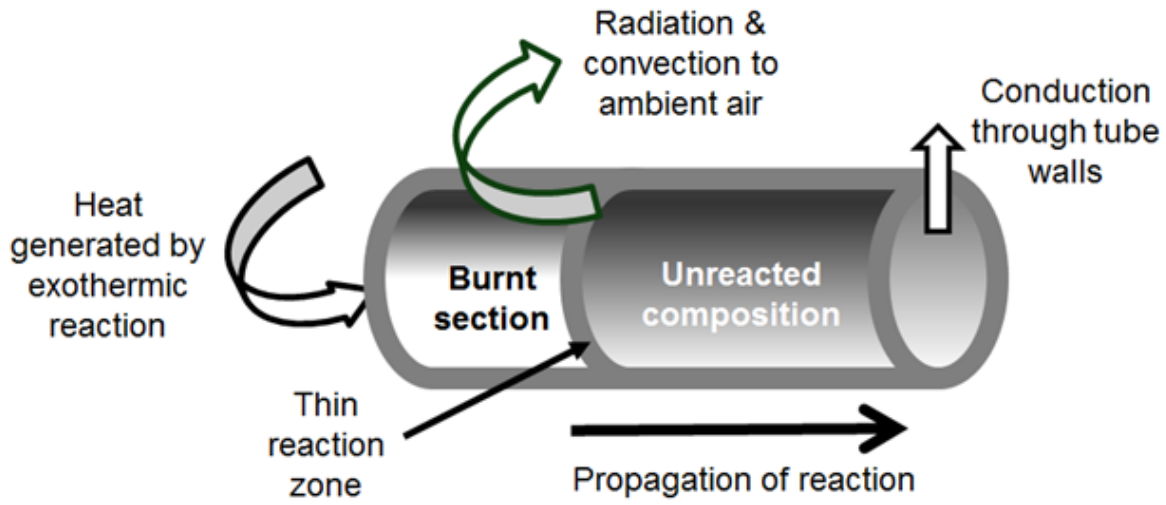

Figure 2-3： Schematic illustration of the elementary model of a delay element in a cylindrical column showing the heat flows affecting performance

With these assumptions for a pyrotechnic composition which undergoes self-sustained self-propagated combustion, the energy balance equation for the setup above is as follows:

$$\rho C_p \frac{\partial T}{\partial t} = \lambda \frac{\partial^2 T}{\partial z^2} + \rho Q r_s - \frac{4h}{d}(T - T_0) - \frac{4\sigma\varepsilon}{d}\left(T^4 - T_0{}^4\right) \tag{2-10}$$

The definitions of each term are listed in **Table 2-3**. Equation 2-11 is assumed to follow the initial and boundary conditions presented in equation 2-10 which is applied to a cylindrical column:

$$\begin{array}{lll} t = 0 & Z > 0 & T = T_0 \\ t > 0 & Z = 0 & T = T_* \\ t > 0 & Z \to \infty & T = T_0 \end{array} \tag{2-11}$$

Table 2-3： Detailed description of the terms used in the energy balance equation 2-10

Terms	Description
$\rho C_p \frac{\partial T}{\partial t}$	The rate of the local energy change
$\lambda \frac{\partial^2 T}{\partial z^2}$	The rate of the local energy redistribution of heat conduction
$\rho Q r_s$	The rate of heat generation by the exothermic chemical reaction
$\frac{4h}{d}(T - T_0)$	The rate of the surface convection heat loss
$\frac{4\sigma\varepsilon}{d}\left(T^4 - T_0{}^4\right)$	The rate of the surface radiation heat loss

By combining equation 2-10 and other dimensionless energy and mass equations, the calculation and analysis of ignition criteria for gasless self-propagating reactions are simplified by converting these parameters into a dimensionless form using mathematical methods (Zhang and Stangle, 1993). Using converted dimensionless parameters θ, Z and τ (listed in Table 2-4), the selected reaction kinetics were assumed to be second-order in conversion. Equation 2-10 was then rewritten as follows:

$$\frac{\partial\theta}{\partial\tau} = \frac{\partial^2\theta}{\partial Z^2} + \beta\, exp\left[-\frac{\gamma}{\theta}\right]\varepsilon_1\varepsilon_2 - 2\omega\left(\theta-\theta_\infty\right) - 2\delta\left(\theta^4-\theta_\infty^4\right) \qquad (2\text{-}13)$$

which was solved numerically subject to the boundary conditions in equation 2-11. It was concluded that the relative significance of dimensionless groups (listed in Table 2-3) was in decreasing sequence of γ, β, δ and ω. An approximate guide to the existence of self-sustaining and self-propagating combustion of the compositions was noted at a ratio of $\Delta H_R / C_p > 1500\,K$.

Table 2-4: Descriptions and a range of values for the dimensionless groups (Zhang and Stangle, 1993)

Dimensionless Groups	Description	Range of Values
$\beta = \frac{(\Delta H_r) k_0 a_v r_0^2 \rho^*}{k_s T_R}$	The rate of local heat generation	$10^8 \sim 10^{19}$
$\gamma = \frac{E_A}{k_B T_R}$	A ratio of activation energy to thermal energy	$40 \sim 200$
$\omega = \frac{h r_0}{k_s}$	The rate of surface heat loss by convection	$0.0 \sim 50$
$\delta = \frac{r_0 T_R^3 \sigma\varepsilon}{k_s}$	The rate of surface heat loss by radiation	$0.0 \sim 3.5$
$\lambda_i = \frac{v_i M_i}{\rho_i} \frac{k_0 a_v r_0^2 \rho^*}{\alpha_s}$	Reaction rate (i = 1,2,3.)	-
$\theta = \frac{T}{T_R}$	Dimensionless temperature	-
$Z = \frac{z}{r_0}$	Dimensionless axial position	-
$\tau = \frac{\alpha_s t}{r_0^2}$	Dimensionless time and thermal diffusivity are given by $\alpha_s = k_s / \rho_s C_{p_s}$	-

Combustion in delay column. The combustion of the delay compositions in a delay column starts from the ignition, which can be described as a process of stimulating a pyrotechnic composition to release its internal energy (Kosanke et al., 2004). The ignition temperature (T_{ign}^{*}) is defined as the minimum temperature to which a pyrotechnic composition with a specified size, shape and boundary constraint must be heated in order to induce a thermal run-away (Pickard, 2002). **Figure 2-4** illustrates a Semenov diagram which shows the relationship between the rate of heat generated or heat loss and the temperature (Johnson, 1965; Merzhanov and Abramov, 1981). With the assumption of zero-order reaction kinetics, and from the shape of the heat-generated curve, the rate of heat generated from the reaction inside the composition agreed well with the exponential curve of the Arrhenius temperature dependence of the reaction rate constant. As the temperature increases continuously, the rate of heat generated increases sharply and then leads to a thermal run-away. The heat loss curve is inversely proportional to the difference in temperature. Thus the heat balance of this model is expressed in equation 2-14:

$$\rho C_p \frac{dT}{dt} = \rho Q k_0 \, exp\left(-E/RT\right) - h\left(A/V\right)\left(T - T_0\right) \tag{2-14}$$

where k_0 and E are the Arrhenius pre-exponential factor and activation energy, respectively; and A and V are the heat transfer surface and the volume of the sample, respectively. Descriptions of other symbols are the same as those in **Table 2-1**. A critical tangent point B is the lowest temperature at which the rate of heat generated is equal to the rate of heat loss, and the tangency temperature (T_*) refers to the ignition temperature (T_{ign}). After this point, the reaction would be spontaneous, self-sustaining and self-propagating, as the rate of heat generated is larger than the rate of heat loss.

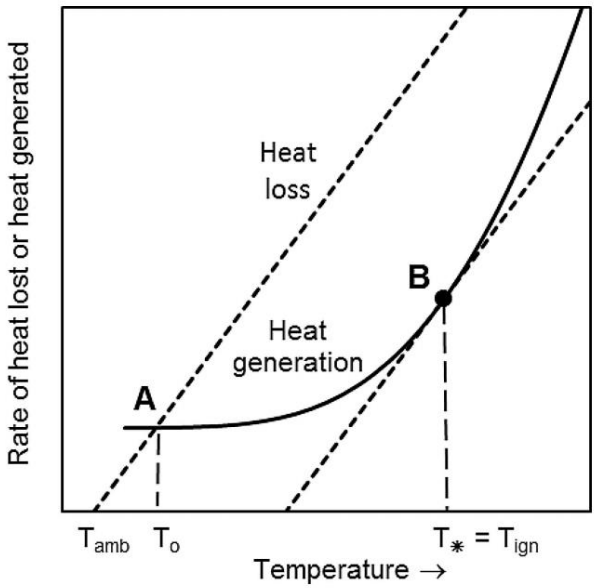

Figure 2-4： Semenov diagram which illustrates the relationship between rate of heat generated or heat loss and temperature

The successful ignition of pyrotechnic compositions is influenced by the net heat generated by the chemical reaction and the stoichiometry. Ignition failure occurs commonly as excessive heat loss to the environment occurs over the entire length of the delay column, most likely in small-diameter container tubes and at lower ambient temperature. Ignition will be enhanced by low thermal conductance and heat capacity, small particle sizes, as well as high heat of reaction. Combined with the thin reaction layer along the propagated combustion direction, the condition of successful propagation can be that sufficient energy fed back from the pre-reacting layer to the reacting layer must be larger than the activation energy. The so-called propagation inequality expression can be written as follows (Kosanke et al., 2004):

$$\Delta H_r \bullet F_{fb} > E_a \tag{2-15}$$

where ΔH_r, F_{fb} and E_a are the heat of reaction, fraction of energy fed back and activation energy, respectively. Hence the possibility of successful propagation can be enhanced by higher heat of reactions, larger fraction of energy feedback and lower activation energy.

Numerous theoretical models are applied for predictions of combustion rates in a delay element under varying conditions such as the nature of the particles (shape, size and size distribution); the physical properties of the reagents (e.g. density, heat capacity); the stoichiometry of the compositions; and the manufacture of the reagents. The advantages of these predictions can be to minimise the potential safety risks in experimental work and to aid in confirming whether the observed data are reasonable. The simplest chemical kinetic theory

was analytically the relationship between the combustion rate of a delay composition and its physical and surrounding properties. It is based on the following key assumptions (Khaikin and Merzhanov, 1966):

- Reaction only occurs in a thin reaction zone.
- Physical properties are independent of temperature and composition.
- A gasless exothermic n^{th} order solid-state reaction is postulated.
- No phase transitions are assumed.
- Arrhenius temperature dependence is considered.

Under these assumptions and adiabatic reaction conditions, an expression for linear burn rate is yielded as follows:

$$u^2 = \frac{g(n)RT_c^2}{E_a(T_c - T_0)}(\alpha k_0)e^{-E_a/RT_c} \tag{2-16}$$

where $g(n)$ is a dimensionless function of the reaction order n with assumed values in a range of 0.5 and 2; the interpretation of other variables is listed in **Table 2-4**.

Another analytical model was based on a completely different theory and the following assumptions (Aldushin and Khaikin, 1974):

- Compositions are packed in neatly stacked layers.
- Reaction and inter-diffusion take place in growing layers of products.
- Particles are flat.
- Reaction rate is governed by parabolic law.
- Arrhenius temperature dependence is considered.

Under these assumptions and adiabatic reaction conditions, an expression for burn rate is yielded as follows:

$$u^2 = \frac{6RT_c^2}{E_D(T_c - T_i)}\left(\frac{\lambda A_0}{\rho C_p d^2}\right)e^{-E_D/RT_c} \tag{2-17}$$

where the interpretation of variables is listed in **Table 2-4**.

A unique model was different significantly from the above two models and is based on the following assumptions (Dunmead et al., 1989):

- A homogeneous liquid phase is created as solid reactants melt before reacted.
- Reactions are dependent on order-based kinetic.
- Arrhenius temperature dependence is considered.

Under these assumptions and adiabatic reaction conditions, an expression for burn rate is yielded as follows:

$$u^2 = \frac{N\lambda k_0 R T_c^2}{\rho h_{rx} E_a} e^{-E_a/RT_c} \tag{2-18}$$

where the interpretation of variables is listed in **Table 2-4**. The great disadvantage of this model is the extreme dependence on the reaction order.

Apart from the mathematical analysis for combustion rate in delay elements, the time variation also affected the predicted results although it is eliminated in those models above. Considering the temperature and concentration obtained from the combustion process, a numerical model is derived from a heat balance in equation 2-19 based on the following assumptions (Beck et al., 1984):

- Reaction only occurs in a thin reaction zone.
- Mass transfer effects are neglected.
- Gasless reactions occur with planar propagation front.
- The single heat source is the chemical reaction heat.
- Heat loss occurs only via convection and radiation.

$$\rho h_{rx} \frac{d\alpha}{dt} + \frac{\lambda}{u^2} \frac{d^2 T}{dt^2} - q_L (T - T_i) = \rho C_p \frac{dT}{dt} \tag{2-19}$$

where q_L is the lateral heat loss coefficient which should be constant or neglected; d here is the particle size measured specially. Interpretation of other variables can be found in the list of symbols on page x of this document.

2.3 Measurement of combustion rates

Whether the combustion rate refers to the mass rate or linear rate, the combustion time is a crucial determining parameter for the combustion rate. Hence the accuracy of the combustion time determines the accuracy of the combustion rate. To date, popular measurements of the combustion time can be summarised into the following two methods and the average combustion rate is obtained using the measured time.

The first approach of the combustion rate is set up for combustion performance in a sequence in which compositions are ignited by stimuli at one end of the delay element and combustion are stopped at the other end. The signal of the combustion flame pulsed to the end is detected by a photoelectric cell. The first commercial technique was assembled for use on complete delay detonators (Hedger, 1983). The variation of this method may be based on the type of stimuli used to initiate the combustion such as a shock tube, sound sensor, thermocouple, fuse-wire or an optical sensor. Much more detailed information on measurement setup combined with a shock tube was described by Tichapondwa et al. (2015). As this method is constructed at low cost and is simple to set up, similar constructions were applied in the laboratory to some extent (AI-Kazraji and Rees, 1979;, Beck et al., 1984; Beck and Brown, 1986a; Elischer et al., 1986). A photoelectric cell which replaced the shock tube was used to capture the image of emitted light from the ignition (Li et al., 2010). However, the requirements of this method should be tested in a tube with both open sides; as a result, the combustion rate is in doubt when compared to a closed end delay element. Another set up was constructed using thermocouples to obtain a sharply temperature-varying point at which a starting timing signal was produced by the ignition of flame propagation (Swanepoel et al., 2010).

The second approach adapted a high-speed camera, which is placed in a perpendicular direction based on the combustion testing axial direction at a specific distance. Images of the flame propagation front are captured by the high-speed camera when pyrotechnic compositions are combusted in glass tubes (Kappagantula et al., 2011). The great advantage of this method is that it is capable of capturing detailed images of the transient flame propagation front of fast-burning systems and aids in research on the reaction mechanism. This method is suitable for easier capturing of the optical signal whether using visible tube materials or suitable coating materials outside the tube wall with temperature-sensitive light and light which is easier to emit. When combined with a series of thermocouples, temperature

profiles were drawn by using transient experimental data obtained through the number of points set up along the length of the delay element. Temperature profiles drawn provide aids to understanding the combustion process and energy variation throughout the different sections of the delay elements (Boddington et al., 1982; Boddington et al., 1986; Boddington et al., 1989). Evaluation of experimental data and data obtained from numerical predicted models have been presented in several published works (Boddington et al., 1989; Montgomery et al., 2017a; Montgomery et al., 2017b) .

2.4 Factors affecting combustion rates

Kosanke (2014) published an exhaustive list of 15 parameters that affect combustion performance, which should be considered prior to designing new pyrotechnic delay compositions. These parameters were categorised based on the nature and manufacturing process of the pyrotechnic compositions themselves, the preparation method and the materials of construction chosen for the delay element housings (Berger, 2005; Focke et al., 2019). It should be noted that the effect of these parameters on the combustion rate is generally qualitative. However, an accurate influence predicted of each parameter cannot be obtained owing to the complex and non-linear relationship between the parameters. Here, some of the main factors that influence the burning rate are discussed. These include the nature of chemicals and compositions, the size and morphology of particles, binders, additives, degree of mixing and packing, container materials chosen, and environmental factors.

2.4.1 Components and compositions

The chemicals chosen for the pyrotechnic delay compositions always serve as the fuel, oxidiser and sometimes additives based on different applications. The preferred chemicals should be non-hygroscopic and stable during the handling and compaction. As well as their readily ignitable property, the chemicals should not be affected by the temperature during storage and transportation. Based on these requirements, the reaction between the fuel and oxidiser should be exothermic, self-sustaining and self-propagating. Therefore, the significant influence of the nature of the chemicals chosen can be demonstrated by the activation energy and the heat of reaction (ΔH_R) (McLain, 1980).

Choice of Fuels. Since the combustion propagation of the pyrotechnic delay elements takes place through the re-ignition for layer-to-layer along the axial direction, the degree of energy

transferred from the reacted to the unreacted thin region is affected by the thermal transport phenomena of the selected chemicals consisting of the formulations, such as conduction, convection and radiation. It is well known that current fuels are typically metallic, non-metallic, metalloid and organic. Among them, the relatively preferred fuel is metals with higher thermal conductivity and lower melting points. Steinberg et al. (1992) and Cashdollar and Zlochower (2007) displayed the melting points and boiling points of some familiar fuels such as metallic fuels (Pb, Mg, Al, Fe, Ti, Zr, Mo and W), metalloids (B, Si), inorganic fuels (C, P, S) and organic fuels. Among them, the metals with the lowest and highest melting points are Pb and W respectively. However, the heavy metal Pb presents a potential hazard problem to environmental and health and safety because of the series of its oxides such as PbO_2.

Familiar metallic fuels are Al, Mg, Mn, Ti, Fe, W, Zn, Al-Mg alloy and other metallic alloys, which are employed in most binary compositions. Aluminium, magnesium and their alloys are notably attractive to many researchers due to their safety, non-toxicity, environmentally friendly, acceptability, low cost and availability in a wide range of particle sizes and shapes. When different metal fuels reacted with one selected oxidiser such as MnO_2, various burning performances were observed. When Mn was used as a fuel in the binary compositions, Swanepoel et al. (2010) and Miklaszewski et al. (2014a) reported the range of combustion rates to be 5 – 22 $mm \cdot s^{-1}$ and 2.4 – 7.3 $mm \cdot s^{-1}$, respectively. This difference was attributed to the difference in particle size of the manganese fuel used. While Koenig et al. (2017) studied compositions containing tungsten (W) as the fuel and MnO_2 as the oxidiser, and the range of the combustion rates was 0.67 – 1.68 $mm \cdot s^{-1}$ and 1.62 – 4.61 $mm \cdot s^{-1}$, in which the former rates are for samples that burnied in open air and the latter rates are for samples that were pressed into Al tubes. This indicates that the combustion rate is affected by many parameters, not only one. Apart from single metallic fuels, metallic alloys are sometimes a better choice as a fuel in pyrotechnic delay systems. Vaz and Pantoya (2022) attempted to explore the different effect of the fuels on the flame propagation speed and the results showed that the combustion rate was in the range of 162 – 175 $m \cdot s^{-1}$ for Al and Al-Si alloy. Compared to classic Al-MoO_3 thermite, thermite consisting of Al-Si alloy and MoO_3 exhibited better performances on the diffusion-controlled oxidation kinetics, condensed phase combustion, radiant heat transfer and shorter time from ignition to steady flame propagation.

Popular metalloid fuels are silicon and boron. Silicon is a widely used fuel in pyrotechnic time-delay compositions and its binary or ternary Si-fuelled formulations have been reported

in significant number of works in the literature. The combustion rates and reaction mechanisms of Si – Pb_3O_4 binary systems have been thoroughly investigated (Jakubko, 1997; AI-Kazraji and Rees, 1979; Moghaddam and Rees, 1981; Rugunanan and Brown, 1991; Jakubko and Černošková, 1997; Jakubko, 1999; Hedger, 1983). Hedger reported combustion rates in the range of 16 – 300 $mm \cdot s^{-1}$ while Ren et al. (2010) showed that the burning rate was between 2.2 – 3.8 $mm \cdot s^{-1}$. These values were dependent on the chemicals chosen, the variation in powder particle sizes and testing temperatures. For the same oxidiser, the combustion rates of binary B-Pb_3O_4 compositions were investigated in the range between 1.33 $mm \cdot s^{-1}$ and 2.89 $mm \cdot s^{-1}$ at ambient temperature (Li et al., 2010). When considering the toxicity of lead, Bell et al. (2020) provided a two-dimensional lead-free functional pyrotechnic delay-line, and the burning rate of the Si-Bi_2O_3 system with thickness of 100 μm was measured as 52 ± 7 $mm \cdot s^{-1}$. Apart from the pure metalloid fuels, silicides are sometimes used as fuels such as titanium silicide ($TiSi_x$), ferro silicide ($FeSi_x$) and calcium silicide ($CaSi_2$). (Shaw et al., 2015b; Krone and Lancaster, 2000). For the feasibility of boron compounds, boron carbide was investigated as a fuel in pyrotechnic smoke compositions (Shaw et al., 2012; Shaw et al., 2013).

Inorganic fuels generally refer to carbon (C), phosphorous (P) and sulphur (S). The famous example is black powder containing charcoal and sulphur. Koch (2008) reviewed some detailed compositions containing white phosphorous and red phosphorous applied as smoke generators. Comet et al. (2010) investigated the combustion mechanism, sensitivity and the morphology of the combustion residues of the binary composition containing red phosphorous and CuO (micro-scale and nano-scale). In addition, organic fuels sometimes used sorbitol, potassium benzoate and hexamethylenetetramine.

Choice of oxidisers. The main classic types of oxidisers are metallic oxide, organic polymer and some salts containing nitrate, chlorate, perchlorate and chromate. Many heavy metal oxides are normally used such as Cu_xO (x = 1 or 2), Pb_xO_y (x : y = 1:2 or 3:4), MnO_2, Bi_2O_3, and Fe_3O_4. Among these types of oxide, the most important factor to consider when choosing the oxidiser is the relative affinity to the oxygen between the metal elements of the compositions (Conkling and Mocella, 2019). Swanepoel et al. (2010) studied the combustion behaviour of manganese-fuelled delay compositions consisting of MnO_2, Cu_2O, Bi_2O_3, and V_2O_5, and found that the fastest- and slowest-burning binary systems were Mn-Bi_2O_3 and Mn-Cu_2O, respectively. Those burning rates were in the range of 5 – 22 $mm \cdot s^{-1}$ which were measured by the combustion of the mixtures pressed in the Al-tubes. Montgometry et al.

(2016) found that the combustion rate of Mn-Sb_2O_3 binary compositions compressed in lead-tubes was in the range of 4.2 – 9.4 mm·s^{-1} and the surprising explanation was the influence of the intermetallic reaction on the classic thermite reaction. Sanders et al. (2007) reported four nano-scale thermites consisting of Al metal powder and metallic oxides (CuO, WO, MoO_3, Bi_2O_3), and quantitatively measured the pressure and propagation speed of the reaction. Their experimental results showed that each composites' behaviour had a strong dependence on the metal oxides. Sarawadekar and Agrawal (2008) reviewed nano-scale pyrotechnic compositions consisting of Al metal powder and various oxidants such as CuO, Cu_2O, NiO, Fe_2O_3, MnO_2, MoO_3, Bi_2O_3, and WO.

The influence on the combustion performance of systems containing two metal oxides in a single formulation has been studied by many researchers. Poret et al. (2012) investigated the combustion performance of a ternary formulation consisting of Si and two oxidants (Bi_2O_3 and Sb_2O_3). As the amount of the second oxidant added increased, the combustion rates decreased from 18.5 mm·s^{-1} to 5.5 mm·s^{-1} and 14.7 mm·s^{-1} to 4.4 mm·s^{-1} for composition pressed in Al tubes and SS tubes (SS: stainless steel), respectively, which was compared with a Si-Bi_2O_3 binary system. Huang et al. (2019) investigated the effect of metal oxide on sub-micro boron-fuelled thermites and found the Bi_2O_3-CuO mixtures enhanced the combustion properties of boron fuel. Hosseini and Eslami (2010) investigated the relative reactivity of three tin-fuelled pyrotechnic compositions containing nitrate salts (refer to KNO_3, $Ba(NO_3)_2$, $Sr(NO_3)_2$) via the apparent action energy (E), the entropy, enthalpy and free energy of activation ($\Delta S^{\#}$, $\Delta H^{\#}$, $\Delta G^{\#}$) of the combustion process determined. The results showed that the nature of the oxidant played a key role in ignition temperatures. The relative decreasing activity sequence of those tin-besed compositions was $Sr(NO_3)_2$, $Ba(NO_3)_2$ and KNO_3. While considering the hazardous environmental effects of the various oxidisers, Walters and Groven (2019) made an effort to look for replacements of $BaCrO_4$. They established average combustion rates of 10 ± 0.4 mm·s^{-1}, 16 ± 0.4 mm·s^{-1} and 68 ± 1.4 mm·s^{-1} for B-$SrMoO_4$, B-$BaMoO_4$ and B-$BaCrO_4$ binary systems, respectively.

It is noted that sometimes fluoropolymer is used as an oxidiser and has been employed in delay detonators. Potgieter et al. (2016) obtained the maximum open-air combustion rates of binary compositions based on fluoropolymer Viton B, where combustion rates of 40 mm·s^{-1} and 82 mm·s^{-1} were obtained when coupled with Al flake and Mg as fuels, respectively. Cowgill (2017) explored the viability of extrudable pyrotechnic compositions containing poly(chlorotrifluoroethylene-co-vinylidene fluoride). Polytetrafluorethylene (PTFE) was

employed in flare pyrotechnic compositions or base bleed propellants, together with a metallic fuel such as Al or Mg (Nacu, 2011; Xue et al., 2020).

Ratio of fuel/oxidiser. To date, the effect of varying the mass ratios of fuel/oxidiser in binary systems has been extensively studied for many delay formulations (Swanepoel et al., 2010; Ricco et al., 2004; Kappagantula et al., 2011; Kalombo et al., 2007; Gerlich and Wojewódka, 2020; Koenig et al., 2017; Li et al., 2018). The general trend is that the combustion rates increase as the concentration of the fuel increases until the rates reach a maximum value. After this point, the combustion rates decrease due to the excess fuel serving as an inert diluent. The maximum burning rate is typically associated with compositions that contain the fuel and oxidiser in stoichiometric amounts. Upon ignition, stoichiometric compositions release maximum energy which corresponds to an essential completion of the reaction (Kosanke et al., 2004; Berger, 2005). It has, however, been established in some cases that fuel rich compositions may have higher combustion rates due to the higher thermal conductivity and diffusivity which result in more efficient energy transfer between the particles.

2.4.2 Particles

Once the reagents are selected, some parameters corresponding to the physical nature of the reacting particles should be considered fundamentally before designing or creating a new pyrotechnic formulation based on varied applications. These parameters include: particle size and morphology, particle size distributions and BET surface areas. Occasionally, some studies investigate the effects of the packing density of the compositions on the combustion behaviours.

Mean particle size, particle size distribution and BET surface area. The general size-scale used in delay compositions are micro- or nano-scale powder particles. The mean particle sizes and particle size distribution of the reagents play a significant role in the combustion performance of pyrotechnic delay compositions. As the particle size decreases accompanied by increased available surface area, the burning rate increases and the range of the concentration of the fuel with successful combustion widens. This inverse relationship between the particle size and burning rate is attributed to the sufficient active surface area and the number of contact points between the reacting particles. The greater number of smaller particles used in the compositions, the less the energy required. Additionally, the time required to heat the mixtures to the reaction temperature becomes shorter, resulting in higher

burning rates compared to larger particles. When larger powder particles are used, the probability of interrupted burning increases. Silicon-fuelled binary systems typically obey this trend. The influence on the Si powder particle size in Si-fuelled compositions has been extensively investigated (Kalombo et al., 2007; AI-Kazraji and Rees, 1979; Ricco et al., 2004). Tichapondwa et al. (2016b) discussed the effect of particle size on the combustion rate of the Si-$CaSO_4$ binary system where the burning rate increased as the particle sizes of the fuel decreased. The D_{50} of three types of silicon used were 15.2 μm, 5.02 μm and 1.85 μm, respectively. The corresponding burning rates were in the range of 6.6 – 11.0 mm·s^{-1} and 6.9 – 12.5 mm·s^{-1}, respectively for the latter two fuels at 30 – 70 wt-%. Ignition and sustained combustion of mixtures containing the largest fuel particles was achieved at 30 wt-% and 40 wt-% fuel loading. Similar research was reported by Spice and Staveley (1949) on Fe-BaO_2 binary formulations containing 25 wt-% or 36 wt-%. In addition, when oxidisers with a wider particle size distribution were used, the packing density of the binary compositions with Mg was greater. This trend led to a decrease in the ignition temperature and time delay of ignition of the system.

The relationship between particle size and combustion rates is inversely related. When the particle size decreases from micro-scale to nano-scale, the combustion rates increase (Bockmon et al., 2005; Danali et al., 2010; Sarawadekar and Agrawal, 2008). Granier and Pantoya (2004) investigated Al-MoO_3 binary compositions with micro- and nano-sized Al powders, and the results showed that the burning rates varied from 1.2 m·s^{-1} to 29.9 m·s^{-1} as the diameter of the Al particles increased from 17.4 nm to 20 μm. It is noted that the concentration of active Al particles also increased as the particle size increased and the fastest burning rate was of the micro-sized Al-MoO_3 compositions. This varying trend during propagation of the flame was attributed to the Al_2O_3-shell layer acting as a heat sink due to its overall amount and not the thickness. Kappagantula et al. (2011) examined the combustion rate of a Mn-MnO_2 binary system with micro- or nano-Mn fuel particles – the maximum combustion speed was 12.01 mm·s^{-1} for nano-Mn, almost two times faster than the micro-Mn fuel.

Degree of mixing. In most delay formulations, the primary reagents used are solid powder particles, with the degree of mixing playing a critical role in the combustion rate of these compositions. As the flame propagation front flows along the column or channel axial direction, the combustion rate is dependent on the ratio of fuel to oxidiser in the reaction zone. For a fixed length and fixed diameters of the delay elements compacted with a certain amount

of the composition, the heat of the reaction for the same system may not be affected, while the combustion time of the reaction zone of poorly mixed delay compositions should be longer than that of well-mixed compositions. Thus the combustion rate was reduced to some extent in poorly mixed compositions with the local fuels/oxidisers ratio. Four types of preparation methods of black powder were reviewed and the combustion rate was in the range of 0.2 – 0.5 $g \cdot s^{-1}$ (Kosanke et al., 2004). The maximum combustion rate was 156 $mm \cdot s^{-1}$ when the 125 μm mesh was substituted by a 53 μm mesh sieve during mixing (Kalombo, 2008). Several methods of improving the mixing and contact between reagent particles have been explored for pyrotechnic delay compositions. These include spray drying, arrested reactive mixing, ultrasonic mixing and resonant acoustic mixing (Morgan and Rimmington, 2012; Umbrajkar et al., 2006; Nellums et al., 2013; Osorio and Muzzio, 2015; Hope et al., 2015). These processing methods could yield spherical particles with good flow properties and improve the homogeneity of pyrotechnic compositions.

Packing density of particles. Limited research has been published on the effect of the packing density of the compositions in delay elements and their subsequent combustion behaviours. Montgomery et al. (2016) studied the relationship between the burning rate and the particle packing density, which was usually expressed as a fraction of the theoretical maximum density of compositions. The packing density was unaffected by the volumetric ratio of oxidant/fuel particles which had a D_{50} ratio of 0.92 μm / 23.4 μm. Koenig et al. (2017) found a standard TMD of W-MnO_2 compressed pellets for maximising combustion rate and a reduction of combustion rate with higher or lower than the standard TMD (the standard TMD was set up at 60 wt-%). These results were attributed to the different dominant effects on the combustion rate, which were conductively controlled at higher or convectively controlled at lower than standard TMD (Koenig et al., 2017).

Morphology. A variation in manufacturing methods of selected reagents results in variable shapes being produced. These can range from conventionally spherical particles with smooth or jagged surfaces, to flakes and other morphologies (e.g. needle-like shapes). Few studies have been conducted on the effect of particle shapes on the combustion characteristics as applied to delay compositions. McLain (1980) found that the reactivity and speed to the ignition temperature of flakes were greater and quicker than spherical particles under the same nominal mesh size. Doorenbos et al. (2012) determined that the ignition delay time of Al-Bi_2O_3 and Al-Fe_2O_3 binary systems with flake-Al fuel were three times higher than the spherical Al-fuelled binary nano thermites, while the flake-Al used exhibited less influence

on the maximum combustion pressure than spherical Al. Similar performances were found between smoothly spherical and jagged particles.

2.4.3 Binder

The influence of the various types of binder and content used in pyrotechnic compositions and the resultant combustion temperatures and rates have been studied in several investigations. The combustion rate generally decreases as the binder content increases, and compositions fail to burn when excess binder is added. Khan et al. (2018) discussed the effect of three binders (carboxyl methyl cellulose, fish glue and dextrin) on the combustion behaviour of B-$BaCrO_4$ time-delay compositions and only fish glue for Si-PbO-Pb_3O_4 systems. The combustion rate decreased as the binder content increased, and the decrease in rate was significantly higher for the Si-fuelled composition with 1 wt-% fish glue added compared to the Bi-$BaCrO_4$ composition. Fish glue had a better decreasing performance on the combustion rate compared to the other two binders for the B-$BaCrO_4$ composition. The decreasing degree of the combustion rate for B-$BaCrO_4$ was around two times for fish glue to dextrin at 1 wt-%, while very near at 3 wt-% loading. Berger (2015) reviewed the effect of the varying binder content on the combustion rate for Ti-$KClO_4$ composition, and a wide range of decrease in reaction rate was found for reducing agent at the range of 60 – 85 wt-%. Tichapondwa et al. (2021) found that the combustion of Mn-Bi_2O_3 composition was interrupted when more than 3 wt-% binder (polyvinyl alcohol) was used and the burning rate decreased by half for a binary formulation including 35 wt-% Mn. When boiled linseed oil was used in a Sb-$KMnO_4$ composition including 15 wt-% Sb with less than 53 μm particles, the assembled system burned successfully due to the lower ignition temperature (Beck and Brown, 1986b).

2.4.4 Additives

When an additional substance is used as the third component, the combustion rates of binary pyrotechnic compositions are modified by the types of material selected. These additives can be a chemically inert substance, additional metal fuel or oxidant, or a source of reactive intermediate. In most cases, additives act to lower the combustion rate by affecting the effective activation energy, the heat of reaction or the efficiency of energy feedback to the unreacted zone along the delay elements.

Inert additives. Inert additives can alter the thermal properties of the system such as thermal conductivity, heat capacity, and melting point, thereafter leading to a reduction in the combustion rate. Normal inert additives are Al_2O_3, fumed silica, SiO_2, kaolin, diatomaceous earth and so on. McLain (1980) found that the combustion rate decreased as kaolin was added due to its low thermal conductivity. SiO_2 was used as an inert additive to replace some of the fuel in the Sb-$KMnO_4$ system in the range of 0 – 15 wt-%, and the influence on the burning rate was slightly slower compared to the binary system (Beck and Brown, 1986b). Various inert additives were investigated for a Si-$CaSO_4$ binary system and the binary compositions were significantly sensitive to fumed silica compared to other additives (Tichapondwa et al., 2016). Failed combustion in Al tube delay elements was found even though as small wt-% as 1 wt-% fumed silica was added. When the additives with a low melting point were added, a molten phase was produced before the ignition temperature was reached and the contact surface area increased, thus there were faster combustion rates and fewer failed ignitions were generated (Beck and Flanagan, 1992; Beck and Brown, 1986b).

Fuel additives. When fine Cu and Ag powders were selected as additives due to their thermal conductivity, the combustion rate increased (McLain, 1980). Six fuel additives were substituted for 5 wt-% Si in Si-$CaSO_4$ compositions and the highest combustion rate of composition, including metal Al added as a flux, was 2.5 times higher than that of binary compositions (Tichapondwa et al., 2016). While the additional content of Al powder increased, the combustion rates of Si-Sb_2O_3 and Si-$Cu(SbO_2)_2$ compositions decreased (Ricco et al., 2004).

Oxidant additives. Boron oxide and $KMnO_4$ had a minor effect on the combustion rates for the Si-Bi_2O_3 system (Kalombo, 2008). As a minor mass fraction of Bi_2O_3 was added to the Mn-MnO_2 compositions, the combustion rate decreased to cal. 5 $mm \cdot s^{-1}$ (Swanepoel et al., 2010). Tichapondwa (Tichapondwa et al., 2016) found four of six oxidants added were tuneable for combustion rates and the results showed that only compositions with added Bi_2O_3 burned faster than the binary system. It was attributed to Bi_2O_3 acting as a sensitiser.

Intermediate source. Some coarse Sb was substituted by using Sb_2O_3 (as a volatile intermediate) for a Sb-$KMnO_4$ system and the amount of decrease in the combustion rate of the ternary composition was 3 – 4 times that of the original system (Beck and Brown, 1986b).

2.4.5 Container materials

Geometry. The heat flow inside a pyrotechnic delay element is dependent on the heat loss through the container wall for the radial direction and heat transfer along the axial direction. This is due to the container geometry, such as the thickness of the wall, the inner and outer diameters of the delay housing, as well as the physical properties of the materials employed. As the heat produced by the core travels to the wall, heat loss is greater early on due to the adiabatic reaction temperature being at quite a distance from the ambient temperature and the latter heat loss decreasing as the real temperature tends to the adiabatic value. This indicates that radial heat loss is dependent on the thickness of the wall and the increased combustion rate is attributed to the pre-heat step of the unreacted compositions before initiation. Meanwhile, the axial heat loss of the cross-sectional area of delay elements is an important factor in the consistency of the combustion rate for a specific pyrotechnic delay composition. However, few studies on the effect of the thickness of the container wall on the combustion rates have been done as the experimental data were difficult to obtain due to the evaluation or testing methods. In general, radial heat loss increases as the thickness of the wall increases, while axial heat loss for a constant wall thickness increases as the diameters of the container increase. The burning rate of W-MnO_2 compositions compacted in Al tubes with a core diameter of 4.7 mm was slightly higher than those of 6.35 mm in diameter in general. At the same time, the standard deviation of the burning rate increased as the core diameter decreased, causing an unsteady and inconsistent combustion performance (Koenig et al., 2017). Al tubes with a varied inner diameter in the range of 2 – 5 mm did not affect the combustion rate of the Si-Bi_2O_3 system (Kalombo, 2008). The combustion rate increased as the outer and inner diameters of the delay column increased, and lateral heat loss was a significant factor for determining the flame propagation front (Montgomery et al., 2017a). Boddington evaluated the influence of the cross-sectional area of a square channel on lateral heat loss, and a faster-burning propagation was found for a larger cross-sectional area (Boddington et al., 1986, Boddington et al., 1989).

Container materials. The thermal conductivity and diffusivity of wall materials play a key role in determining combustion performance as they affect the conductive, convective and radiational heat flows. Potential materials can be metallic, polymeric and ceramic materials. The common metallic tube wall is Al, Pb, stainless steel and Zn. Larger thermal conductivity of the container wall produces greater heat loss, leading to a larger inner diameter required for keeping a constant combustion rate. Beck found a combustion rate of 1.3 $mm \cdot s^{-1}$ for some

burning compositions propagated in open stainless steel channels with a cross-sectional area of 6 mm × 4 mm, but it failed in Al tubes. The slowest rate was 0.82 $mm \cdot s^{-1}$ for a composition (Sb : $Ba(NO_3)_2$ = 1 : 1) that only burned in an open stainless steel channel. This was attributed to the heat balance of the cross-sectional area being a critical factor for the combustion performance. While the cross-sectional area was fixed, container materials with a low thermal diffusivity had a marked effect on the burning rate, such as plastic materials, which was promised for slow-burning compositions in unconfined systems (Beck and Brown, 1986b). The combustion rate of compositions, including W fuel loading in the range of 40-60 wt-%, increased 142 – 175 % compared to the same diameter of pellets combusted in the open air. However, only a composition at 60 wt-% fuel was ignited in the stainless steel tube and the combustion rate decreased to around 18.5% compared to that of the Al tube. This was due to the different thermal conductivity of the housing materials (12 – 45 $W \cdot m^{-1} \cdot s^{-1}$) for stainless steel vs. 205 $W \cdot m^{-1} \cdot s^{-1}$ for Al (Koenig et al., 2017). When wall material with high thermal conductivity and high volumetric capacity was selected, the combustion rate of a fast-burning system (Si-Pb_3O_4) was significantly enhanced, while the volumetric capacity of tube walls with low thermal conductivity had a little effect the combustion rate (Montgomery et al., 2017a). The combustion rate of compositions compressed in lead tubes was faster than that in Al tubes, but was not affected when the fuel loading was over 25 wt-% (Kalombo, 2008).

Besides the metallic wall, other materials are selected in some cases such as ceramic and polymetric wall, although heat-resistant polymers are not suitable for pyrotechnic delays.Ceramic containers are used and could have a benign effect on marginal situations (Ellern, 1968). It is well understood that the combustion rate of the same formulation pressed in polymetric tube walls is higher than that in metallic containers due to their relatively high thermal conductivity. However, Beck found a dramatic decrease in the combustion rate of compositions pressed in poly(methyl methacrylate) tubes compared to Al tubes, especially for finer particle powders (Beck and Brown, 1986b). To date, fewer studies have been published on the effects of these factors on the combustion rate of pyrotechnic time-delay compositions.

2.4.6 Ambient temperature

Many thermal parameters such as activation energy, heat capacity, thermal convection and radiation heat transfer rate, are always dependent on the temperature. When the ambient temperature increases apart from systems with constant activation energy, the combustion

rate of the pyrotechnic delay elements increases as the activation energy decreases. It is noted that the difference between the ambient temperature and the ignition temperature is reduced as the initiation temperature increases. Less energy should be required to ignite the unreacted composition that is close to the combustion front and the combustion rate would generally get faster at an elevated temperature. However, the current understanding of the relationship between combustion rate and the environmental temperature is not very clearly clarified for pyrotechnic delay elements. For most gasless delay compositions, the combustion rate of different formulations would be 25 % faster/slower at the higher/lower temperature compared to that at room temperature (Kosanke et al., 2004). However, fewer effects on the temperature variations were generated for gassy delay compositions (Kosanke et al., 2004).

The linear relationship between ambient temperature and combustion rate was found for the B-Pb_3O_4 system, and a 50 ℃ decrease in temperature caused the combustion rate to decrease in the range of 3.1% – 8.2 % with varying B content (Li et al., 2010). With a similar temperature design condition, the combustion rate decreased by 8.2 % (Jakubko, 1997). Boddington and La Ye (1987) investigated the effect of varying temperature on the burning characteristics of three gasless pyrotechnic compositions. Montgomery investigated the relationship between combustion rate and factors such as ambient temperature, geometry and materials of the tubes by experiments and modelling. The combustion rate increased by 9.4 % for each 50 ℃ increase in the ambient temperature (Montgomery et al., 2017a).

3. EXPERIMENTAL

3.1Raw Reagents

Raw reagents in this study were used as received from the manufacturers without further processing. The detailed information of these reagents is listed in **Table 3-1** and the characteristic values were obtained through those instruments described in Section 3.4.

Table 3-1： General details of the raw materials

Name	**Manufacturer**	**Particle size (μm)**			**BET ($m^2 \cdot g^{-1}$)**	**Density ($g \cdot cm^{-3}$)**
		D_{10}	D_{50}	D_{90}		
Al	Grinman	6.00 ± 0.03	13.2 ± 0.03	29.0 ± 0.13	0.34	2.70
Ni	Sigma Aldrich	4.74 ± 0.04	10.6 ± 0.03	24.2 ± 0.45	0.24	8.91
Sn	Sigma Aldrich	2.01 ± 0.04	4.25 ± 0.08	8.20 ± 0.27	0.34	7.63
Mn	Atlantic Equipment Engineers	9.19 ± 0.12	24.6 ± 0.3	51.7 ± 0.78	0.29	7.21
NiO	Sigma Aldrich	2.86 ± 0.02	5.36 ± 0.05	9.45 ± 0.11	0.76	6.67
Bi_2O_3	Hunan JinWang Bismuth Industry Co Ltd, China	3.08 ± 0.04	7.48 ± 0.09	17.6 ± 0.67	0.53	8.90

3.2Preparations of time-delay elements

Binary mixtures were prepared by combing the metal fuel and oxidiser or another metal. They were combined in different mass proportions through the brush-mixing technique. Weighed-out reagents were brushed through a 45-μm sieve and repeated five times individually. This facilitated the disintegration of any agglomerates present and ensured good mixing. Either of two different sets of binary mixtures or one set of binary blends and a new metal were chosen to be combined in different ratios to make up the ternary compositions. All sets of binary base mixtures are shown in **Table 3-2**.

Table 3-2： Details of the different base mixtures

Powder/Group	**A-1**	**A-2**	**B-1**	**B-2**	**B-3**
Oxidiser	NiO		Bi_2O_3	Bi_2O_3	
Metal I	Al	Al	Sn	Mn	Sn
Metal II		Ni			Mn
Metal I, wt-%	20 - 55	13.8, 31.5	25 - 55	25 - 40	81.2
ID × OD of glass tubes, mm	4.0 × 6.0	-	-	-	-
	5.95 × 8.0	-	6.0 × 8.0	6.0 × 8.0	-
TMD of powders, %	40 ± 1	-	48 ± 2	48 ± 2	-
Starter	Yes	-	-	-	-

3.2.1 Glass tube delay elements

The well-mixed formulations were loaded into 50 mm long borosilicate glass tubes. The tubes were closed at one end using a small amount of Prestik putty. Small increments of the mixed powders (75 ± 5 mg) were dispensed into the tubes. The loaded powder was consolidated by repeated tapping before adding the next increment. The filling process (only for the Al / NiO / Ni system) was completed by topping the tube column off with a certain amount (about 25 mg for the smaller inner diameter tube and 75 mg for the larger diameter tube) of a starter composition containing Al, Si, Bi_2O_3 and CuO in the ratios of 10:20:20:50 by mass. The sizes of the glass tubes used here and the TMD of the compositions in the glass tubes are shown in **Table 3-2**.

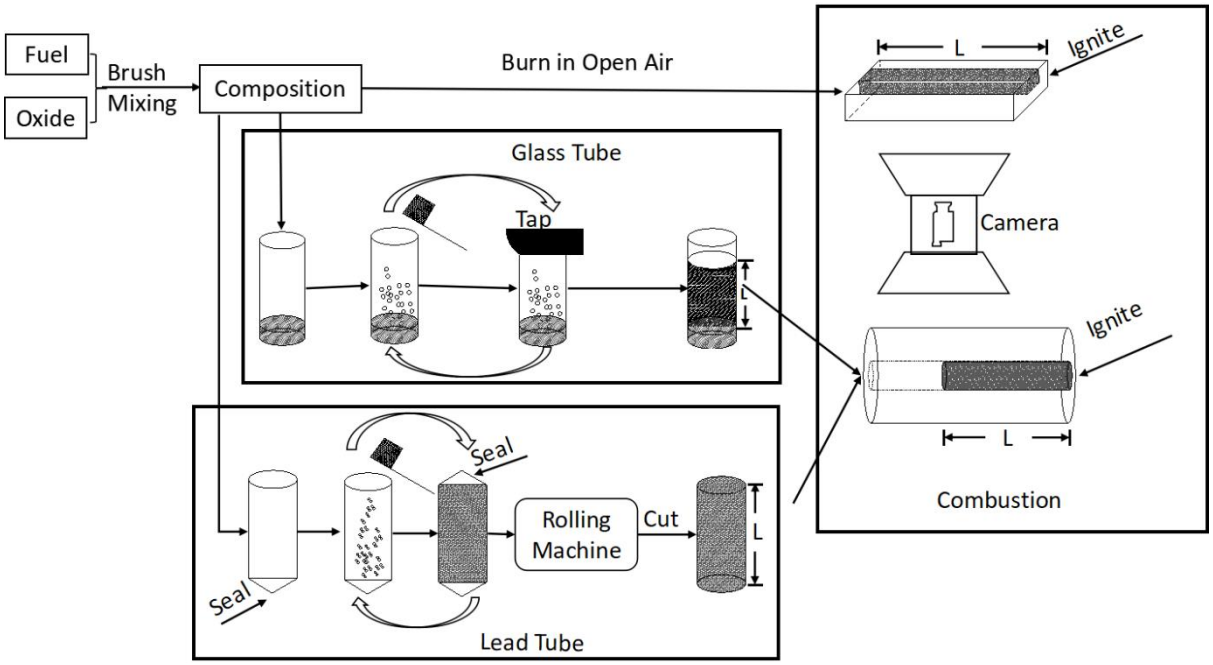

Figure 3-1： Schematic flowchart of the experimental design

3.2.2 Lead tube delay elements

Only six samples that were burned in lead tubes were prepared in a similar fashion. The length and size of starting lead tubes and the components and mass proportion of the compositions used here are listed in **Table 3-3**. Well-mixed powders were tap-filled in the tube with the one end sealed by a crimp. The composition in the tubes were consolidated by applying a series of consecutive rolling operations on a proprietary tube-rolling machine. During each rolling operation, the sealed tube was passed through a hole with a smaller diameter. The rolled lead tubes were then cut to the desired length to form the delay elements.

Then, a portion of the composition was removed at one end to a depth of about 4 mm and replaced by the starter composition described above (only for the Al / NiO / Ni system).

Table 3-3： The compositions and details of the lead tube delay elements

Compositions	**Starting lead tubes**		**Starting powder**	**Lead delay element**		
	Length, mm	ID × OD, mm	Mass, g	Length, mm	ID × OD, mm	TMD, %
35 Al/65NiO	150	7.0 × 11.5	10.0 ± 0.3	40 ± 2	5.5 × 9.5, 5.0 × 9.0, 4.5 × 8.5	54 ± 1
60 (37.6 Al/62.4 NiO) + 40 (31.5 Al/68.5 Ni)						
27.65 Sn/72.35 Bi_2O_3	155		16.0 ± 0.6	38 ± 2	6.0 × 10.0	40.4
30 Sn/70 Bi_2O_3						42.8
50 (27.65 Sn/72.35 Bi_2O_3) + 50 (45 Mn/55 Bi_2O_3)						48.1
50 (30 Sn/70 Bi_2O_3) + 50 (45 Mn/55 Bi_2O_3)						44.6

3.3Burn Rate Measurements

Combustion test of each composition in open air was conducted inside a fume hood. Grooves (depth × width = 2 mm × 4 mm) were machined into pyrophyllite blocks. The well-mixed compositions were placed inside these slots and mildly compacted with the assistance of a small stainless steel spatula. The length of the mixtures was set to around 40 mm. A small amount of the starter composition was placed at one end and ignited with a butane torch.

As for the combustion test of lead tube delay elements, the compacted lead tube elements were clamped in a horizontal position. The filled glass tube was placed inside a second, slightly larger, glass tube serving as a horizontal holder. Ignition was trigged with an electrical fuse positioned in contact with the starter composition.

The burning events for both tests were recorded with a digital camera at a frame rate of 240 Hz. The burning rate was estimated from the burn time, extracted from the video recording, and the effective burn length.

3.4Characterisation

3.4.1 Scanning electron microscope

The micro-scale morphology of the raw reagent particles was studied with a Zeiss Ultra Plus 55 scanning electron microscope fitted with an in-lens detector. The voltage setting was 1 kV. The samples were carbon-coated with an Emitech K950X coater before scanning.

3.4.2 Particle size and BET surface area

Particle size distributions were measured by using a Malvern Mastersizer 3000. The Brunauer-Emmett-Teller (BET) surface area of the powders was studied using the 5-point technique with a Micromeritics TriStar II 3020 instrument. The powders were degassed for 8 hours at 100 ℃ in the Micromeritics Vac Prep 061 Sample Degas System. Thereafter, the samples were loaded onto the instrument and measurement runs were conducted to completion. A summary of the particle size and BET data are given in **Table 3-1**.

3.4.3 X-ray diffractions (XRD) and X-ray fluorescence (XRF)

X-ray diffraction (XRD) analyses were performed with a Bruker D8 ADVANCE instrument for raw materials and the residues that were collected after combustion. The burn residue slags were milled into fine powders using a tungsten carbide mill as the residues were very hard. The samples (including the raw materials and the milled residue slags) were prepared according to the standardised Panalytical backloading system, which provides nearly random distribution of the particles. The samples were analysed using a PANalytical X'Pert Pro powder diffractometer in θ-θ configuration with an X'Celerator detector and variable divergence and fixed receiving slits with Fe filtered Co-Kα radiation (λ= 1.789 Å). The mineralogy was determined by selecting the best-fitting pattern from the ISCD database compared to the measured diffraction pattern using X'Pert Highscore plus software. The relative phase amounts (weight % of crystalline portion) were estimated using the Rietveld method (X'Pert Highscore plus software).

X-ray fluorescence spectroscopy (XRF) analyses were performed on the raw material powders using the Thermo Fisher ARL Perform'X Sequential XRF instrument with Uniquant software. The samples were prepared as boric acid pellets, mixed with 3 drops Movol (PVA), and pressed to 10 tons. The obtained values were normalised as no changes in the crystal water were determined. Meanwhile, a standard sample material was prepared and analysed in the same manner as for the samples.

3.4.4 Bomb calorimeter measurement

Energy output measurements of selected compositions were conducted in a Parr 6200 bomb calorimeter. A proprietary starter (200 mg) with known energy output was used to initiate the Mn-Bi_2O_3 samples, weighing between 2 and 3 g. For the Sn-Bi_2O_3 mixtures, the sample size was about 5-6 g with no starter. Ignition was accomplished with an electrically heated 30-

gauge (0.25 mm) nichrome wire initiator. The tests were conducted in an inert helium atmosphere at a starting pressure of 3.0 MPa. Measurements were carried out in three times. The reported results were corrected for the effect contributed by the starter.

3.4.5 EKVI simulations

Thermodynamic simulated calculations were undertaken to determine the adiabatic reaction temperature, predicted products and changes in phase fractions versus the fuel-to-oxidizer or fuel-to-second metal ratio. All of the above were obtained with the EKVI Release 4.30 thermodynamics software. The stoichiometric reactions were obtained based on the construction of the reaction criteria, which contained specifying components in the reagents, and the pressure, temperature and potential products (based on the software database).

A summary of the EKVI calculation settings is given below:

(i) The units for the amount of the reagents used and the resulting energy outputs were gram and kJ, respectively.

(ii) The pressure of the system was always set at 1 atm for each run.

(iii) The amount of reactants was varied from 0.02 g to 0.98 g, with increments of 0.02 g for the fuel (Al or Sn) and a concomitant decrease of 0.02 g for the oxidiser (NiO and Bi_2O_3).

(iv) For the Mn-Bi_2O_3 binary system, the reagent amounts ranged from 0.05 g to 0.95 g with increments of 0.05 g for the Mn fuel and a concomitant decrease of 0.05 g for the Bi_2O_3 oxidiser.

(v) The “find the maximum temperature” function was activated since no temperature constraints were specified.

(vi) Simulations were run with the “auto-select-species” function activated, allowing them to utilize the EKVI database that contains approximately 3000-4000 chemical compounds in both gas and condensed phases as part of the calculation. This enabled the simulation to make use of the EKVI database that contains3000 – 4000 chemical compounds in gas and condensed phase.

4. RESULTS AND DISCUSSION

4.1 Al-NiO-Ni TERNARY SYSTEMS

4.1.1 Powder Characteristics

All the reagents were used without further processing. **Figure 4-1** shows the particle size distribution and the X-ray diffraction (XRD) spectrum of the nickel oxide, aluminium and nickel. X-ray diffraction analysis confirmed the high purity of the starting reagents. The particle size distribution of the Al and Ni metal grains were fairly broad and had D_{50} values of 13.2 ± 0.03 μm and 10.6 ± 0.03 μm, respectively. The NiO powder had a narrower range and presented a D_{50} of 5.36 ± 0.05 μm.

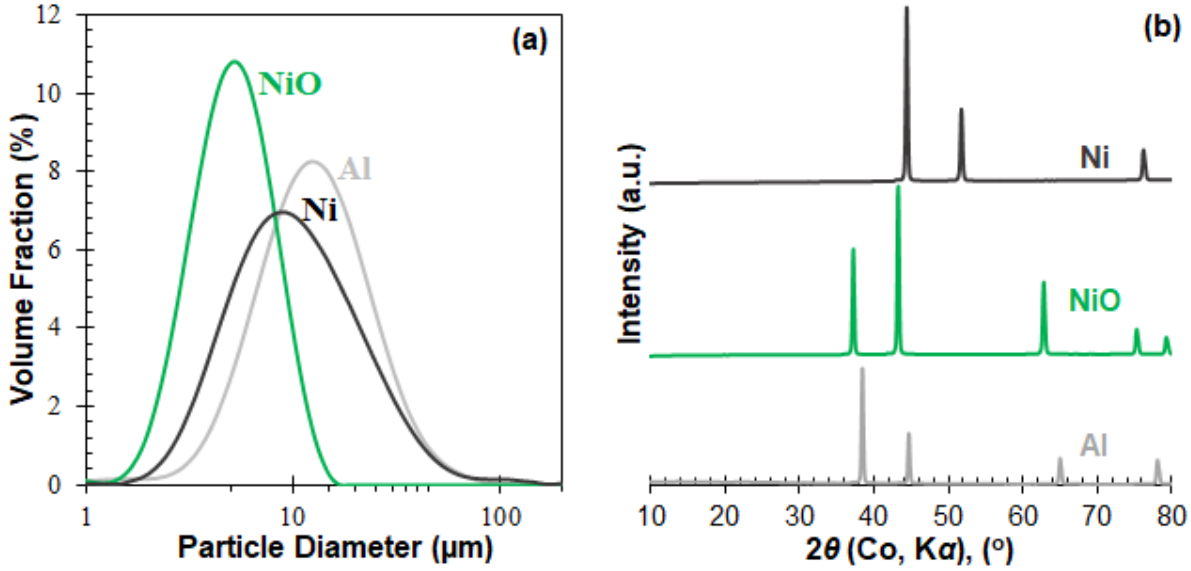

Figure 4-1: The particle size distributions (a) and the XRD results for the nickel oxide, aluminium and nickel (b)

Figure 4–2 shows the SEM images of these three raw powders. Obvious agglomerations were illustrated from the surface morphologies of the Ni and NiO powders by much smaller primary crystals. It is noted that approximately 12 vol.% of the particles were larger than 25 μm for the Al and Ni powders.

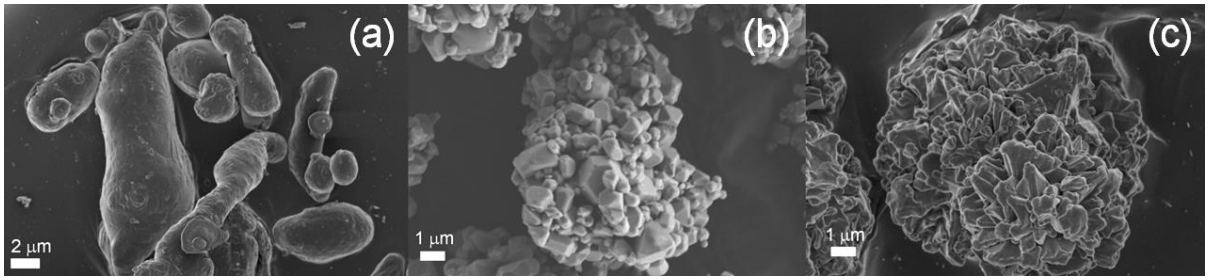

Figure 4-2： SEM graphs of the Al (a), NiO (b) and Ni particles (c)

4.1.2 EKVI Simulations

4.1.2.1 Al-NiO thermite system

The EKVI simulated results of the Al-NiO thermite system versus the metal-fuel mass fraction are shown in **Figure 4-3**. The peak of the adiabatic reaction temperature (T_{ad}) was about 3100 K at 19.8 wt-% Al loading. This corresponded to the predicted typical exothermic reaction 2 Al + 3 NiO → Al_2O_3 + 3 Ni. However, the peak temperature of this binary system was predicted at ca. 3181 K at 19.4 wt-% Al loading when using Factsage software (Shaw, 2020). This small difference could be due to differences in information in the databases used by the different software. However, the main reaction was similar (2 Al + 3 NiO → Al_2O_3 + 3 Ni). It is apparent that there was an adiabatic temperature plateau at ca. 3090 K with a fuel loading range between 20 wt-% and 38 wt-%. A possible reason for this observation is the intermetallic reaction between Ni and Al, which resulted in increased NiAl generation with an increase in the fuel-mass ratio. The T_{ad} decreases as the amount of Al increases beyond 38 wt-%. This was accompanied by the formation of higher-order intermetallic species of Al and Ni (Bochenek and Basista, 2015).

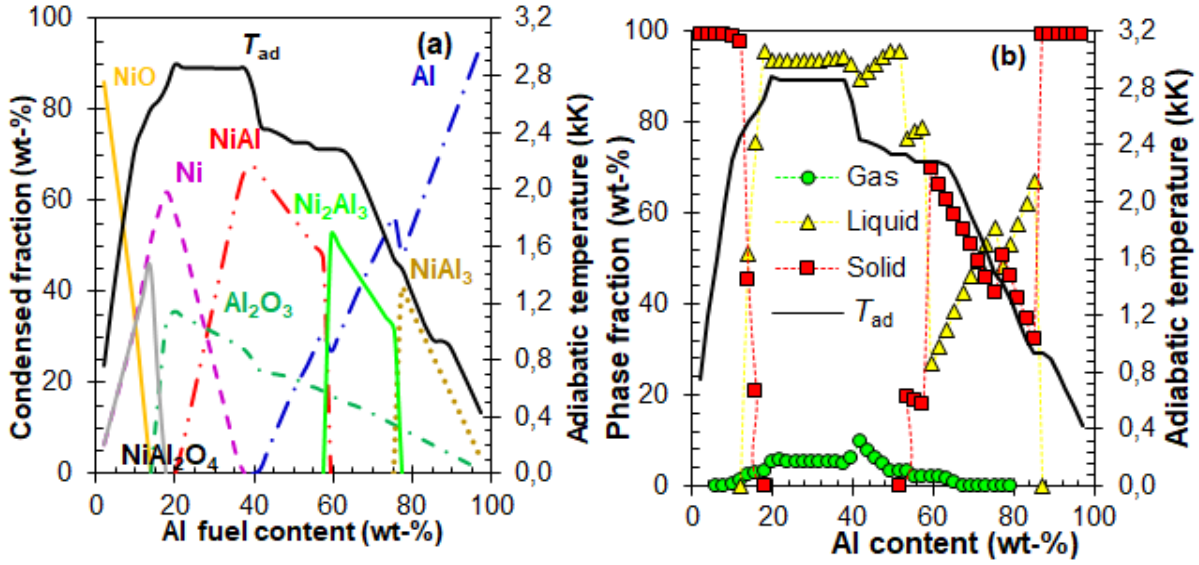

Figure 4-3： EKVI simulation results for the Al-NiO thermite blends: adiabatic reaction temperature and the expected condensed products (a), and phase mass percentage (b)

The Ni-Al binary phase diagram includes the well-known five intermetallic compounds, i.e. Ni_3Al, NiAl, Ni_2Al_3, Ni_5Al_3 and $NiAl_3$. Ni_3Al is remarkably undetected in the EKVI calculation. This may be attributed to its thermodynamic instability in the presence of the $NiAl_2O_4$ and Al_2O_3 phases. Intermetallic compounds, like NiAl, Ni_2Al_3 and $NiAl_3$, were estimated to have formed at a higher Al loading. Compositions prepared using 40 wt-% Al or more featured unreacted fuel in the predicted product mixture. This gives an indication of the stoichiometric ratios of this composition.

Figure 4-3(b) shows that the reaction mixture predominately consisted of liquid and gas (>92 wt-% liquid) phases when the Al composition ranged from 20 wt-% to 55 wt-%. Since T_{ad} was above the melting point of Al (933.5 K), the potential theoretical reaction, 4 Al (l) + Al_2O_3 (s) → 3 Al_2O (g), was estimated to have occurred (Porter et al., 1955). The expected gaseous components generated under isothermal conditions were O_2, Ni, Al and Al_2O. However, the actual reaction temperatures will most likely not reach the theoretical adiabatic temperature as a result of the lateral heat losses. The presence of gaseous product was therefore negligible in the actual combustion events.

4.1.2.2 Al-Ni binary system

Figure 4-4 provides the EKVI calculations of the Al-Ni metal system. It shows the gradual formation of four intermetallic products Ni_3Al, NiAl, Ni_2Al_3, and $NiAl_3$ as the amount of Al fuel increased. Changes in adiabatic temperature and phase generally reflect changes in the target intermetallic product. When the Al fuel content was less than 14 wt-%, the condensed products were a blend of Ni and Ni_3Al. The corresponding reaction was Al + 3 Ni → Ni_3Al

with a charge of ca. 13.3 wt-% Al loading, while the Ni reacted completely. At this point, all compounds remain in a solid state. Between 14 wt-% and 32 wt-% Al, Ni_3Al and NiAl compounds co-existed. It corresponds to the reaction Al + Ni → NiAl at ca. 31.5 wt-% Al, and simultaneously, the liquid fraction of the product attained a maximum of ca. 73 wt-%. When the Al fuel percentage was between 32 wt-% and 42 wt-%, NiAl and Ni_2Al_3 co-existed. As the T_{ad} reached 2200 K, Ni_2Al_3 was the main product at ca. 40.8 wt-% Al due to the reaction 3 Al + 2 Ni → Ni_2Al_3. However, the peak temperature of the same binary system was predicted at ca. 2254 K at 41 wt-% Al loading when using Factsage software (Shaw, 2020). This small difference could be due to differences in information in the databases used by the different software. It is however worth noting that the same main reaction was identified (3 Al + 2 Ni → Ni_2Al_3). Over 58 wt-% of the Al percentage, the primary product was $NiAl_3$ which corresponded to the reaction 3 Al + Ni → $NiAl_3$. At the same time, the unreacted Al remained in the system. The reaction products were liquefied between 24 wt-% and 76 wt-% Al. No gases were evolved throughout the system.

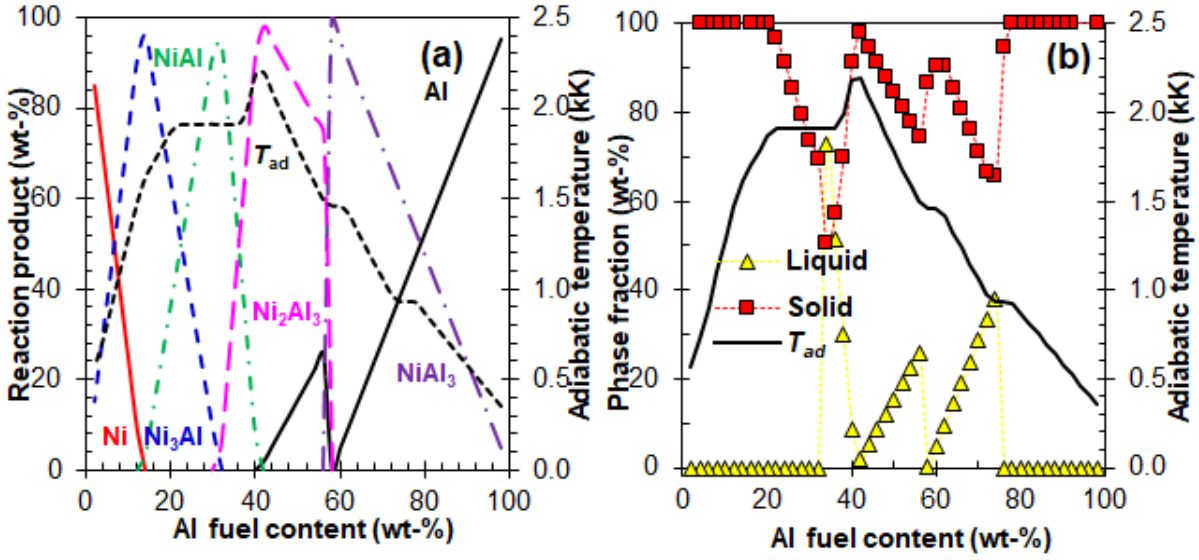

Figure 4-4: EKVI calculations of the Al-Ni metal systems: adiabatic reaction temperature and the expected condensed products (a), phase mass percentage (b)

4.1.2.3 Al-Ni-NiO ternary system

Figure 4-5 illustrates the effect of Al-Ni blend on the adiabatic reaction temperature for EKVI-predicted intermetallic product obtained from the Al-NiO binary system. **Table 4-1** provides details of the linear combination of the Al-Ni blend used here with the Al-NiO thermite blend. The parameters of locus x or y refer to the mass ratio of the compositions required for the thermite reaction **Ia** or **IIa**. It is convenient to compute from the equations $x = 1/[1/(M_{NiO}/M_{Ni})(w_{Ni}/w_{NiO})]$ or $y = 1/1/[1 + 3\ (M_{NiO}/M_{Ni})(w_{Ni}/w_{NiO})]$, where M_i and w_i are the

molar mass and the mass fraction of component *i* in the composition, respectively. Then, ternary I and ternary II are obtained, which displayed a curved line in **Figure 4-5(b)**. When *x* =0 or *y* =0, ternary systems would be changed to the Al-NiO binary thermitic systems, and Al-Ni binary intermetallic systems when *x* =1 or *y* =1. The adiabatic temperature of ternary systems was between the peak temperature of the predicted thermite reaction and intermetallic reaction, namely 1464 K -3092 K and 1587 K – 3088 K for ternary I and II system, respectively. As the mass fraction of the thermite blends increased, the adiabatic temperature decreased for ternary I system. When *x* was in the range of 46 – 72 wt-%, a temperature plateaus occurred because there was no contribution from the thermite reaction. Meanwhile, the ternary II system featured two temperature plateaus when *y* was in the range of 22 – 40 wt-% and 87 – 100 wt-%.

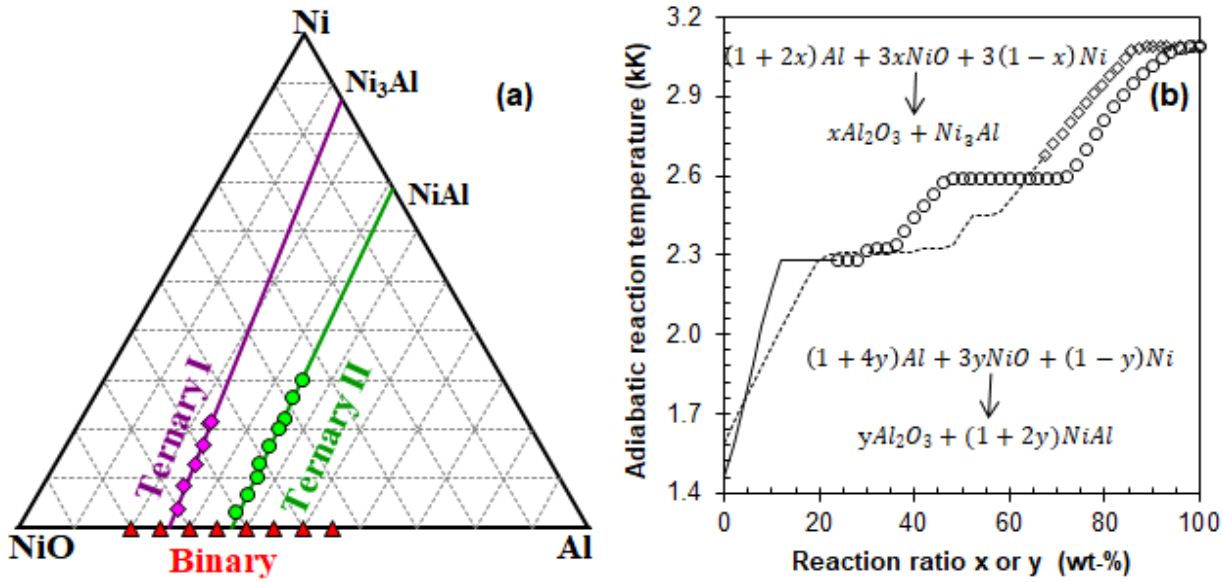

Figure 4-5: (a) Experimental design with binary and ternary composition presently under consideration; (b) effect of Al-Ni mixtures on the projected adiabatic reaction temperature of the EKVI simulation. The symbols (-Δ-, -◊- and -○-) indicate compositions that have been successfully ignited and burned for the Al-NiO binary blend, the Ni_3Al and the NiAl ternary blend, respectively.

When the adiabatic reaction temperature reached about 3090 K, the intermetallic Ni_3Al and NiAl occurred in the thermite binary systems detailed in **Figure 4-4**. However, the adiabatic reaction temperature for these two expected outputs of the Al-Ni binary system is approximately 1465 K and 1590 K, respectively. Not surprisingly, the T_{ad} decreased with an increase in the mass fraction of the Al-Ni blend required. A small decreasing temperature plate occurred when the temperature was around ca. 1460 K, which was attributed to the formation of $NiAl_3$ that occurred as a result of a reaction between Ni_2Al_3 and excessive Al

fuel. Another small temperature plate occurred at a temperature of ca. 933 K, this was likely due to the melting transition of the excessive Al fuel. It is worth noting that the simulated results obtained in this study were almost similar to those obtained using Factsage (Shaw, 2020). Since the pure thermite reaction remained at the same temperature, a different tendency was estimated to have occurred due to different Al-Ni intermetallic products. For the Ni_3Al as a target product, the combustion of the mixtures stopped after the expected T_{ad} decreased to less than 2700 K. However, the combustion of the other ternary system was not sustained when T_{ad} fell below 2300 K.

Table 4-1： Overview of linear thermite reactions

Scheme	Thermite Reaction		Reagents, wt-%		
			NiO	**Al**	**Ni**
4-I	Ia:	$3Al + 3NiO \rightarrow Al_2O_3 + Ni_3Al$	73.5	26.5	-
	Ib:	$Al + 3Ni \rightarrow Ni_3Al$	-	13.3	86.7
	Net:	$(1+2x)Al + 3xNiO + 3(1-x)Ni \rightarrow xAl_2O_3 + Ni_3Al$			
4-II	IIa:	$5Al + 3NiO \rightarrow Al_2O_3 + 3NiAl$	62.5	37.5	-
	IIb:	$Al + Ni \rightarrow NiAl$	-	31.5	68.5
	Net:	$(1+4y)Al + 3yNiO + (1-y)Ni \rightarrow yAl_2O_3 + (1+2y)NiAl$			

4.1.3 Burning Rate

Self-sustaining combustion in the solid state will not be maintained if the adiabatic reaction temperature is below 1800 K (Merzhanov, 1994). No experiments with the Al/Ni binary mixtures have been carried out in this section based on the EKVI simulation. The pre-test Al/NiO binary samples were made by increasing the fuel charge with an increment of 5 wt-% between 10 wt-% and 90 wt-%. Yet only the compositions, including the 20 to 55 wt-% Al fuel charge, were successfully ignited and burned in glass tubes, and plotted as discrete symbols in **Figure 4-5(a)**. Moreover, the linear burning rates of these mixtures were reported in **Figure 4-6(a)**, within an experimental error. The plots were parabolic and the rates were independent of the diameters of the glass tube. In addition, the maximum open-air combustion rate was 740 ± 1 mm^{-1}. It was nearly four times faster than the highest rate obtained in the 4.0 mm ID glass tube, i.e. 191 ± 31 mm^{-1}. The Al fuel contents (ca. 26.5 wt-% and 37.5 wt-%) were associated with the thermite reactions **Ia** (3 Al + 3 NiO → Al_2O_3 + Ni_3Al) and **IIa** (5 Al + 3 NiO → Al_2O_3 + 3 NiAl).

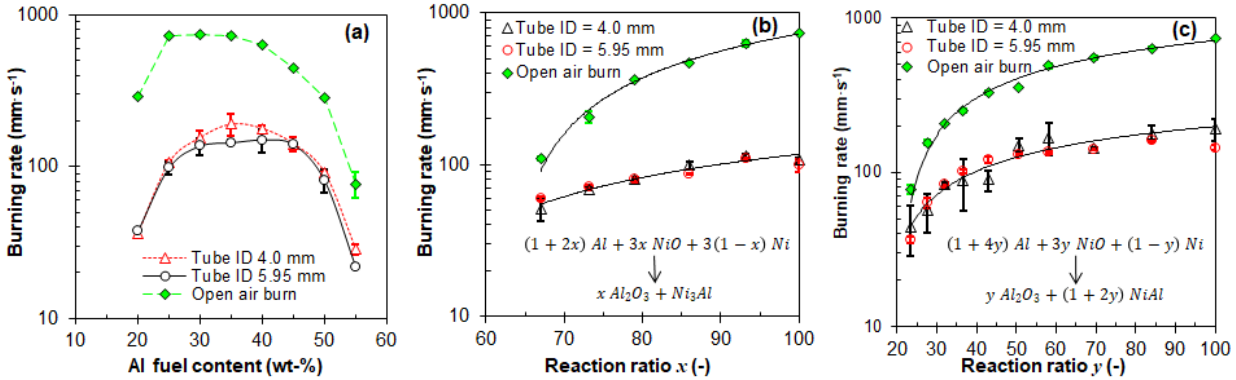

Figure 4-6： Linear burning rate for different mixtures: thermite Al-NiO (a), Ternary I system (b) and Ternary II system (c). The markers (-○-, -Δ-, and -◊-) indicate the open air burning and burning in glass tubes with ID = 4.0 mm and ID = 5.95 mm, respectively.

The bulk density of the filled reagents in the glass tubes was ca. 40 ± 1 % TMD. The measured linear combustion rates for the ternary compositions are presented in Figures **4-6 (b)** and **(c)**. As with the Al-NiO thermite system, the burning rates of open-air combustion were much faster than that packed inside the glass tubes, and non-sensitive to the diameter of the tubes. Linear burning rates in these two ternary systems decreased as the thermite mixtures (mass ratio *x* or *y*) increased. When Ni_3Al was considered as an expected intermetallic product, only compositions comprising more than two-thirds of the thermite mixtures ignited and burned successfully in the glass tubes, with a minimum sustainable rate of 45 ± 16 $mm \cdot s^{-1}$. In the case of the NiAl intermetallic, the sustainable combustion window extended over a larger compositional range, and the lowest rate was 36 ± 2 $mm \cdot s^{-1}$. The combustion burning rates were slightly slower in lead tubes than compositions in glass tubes. It was worth noting that the different burning rates were caused by the wall material's physical properties and the tubes' thickness (2.0 mm and 1.0 mm for the rolled lead tubes and glass tubes, respectively).

Table 4-2： Burning rates ($mm \cdot s^{-1}$) of a binary and ternary composition in the different types of delay elements

Type	ID × OD, mm	Binary[1]	Ternary[2]
Open[3] burn	4.0 × 2.0	734 ± 18	156 ± 6
Glass tubes	5.95 × 8.0	144 ± 5	65 ± 5
	4.0 × 6.0	191 ± 31	57 ± 16
Lead tubes	5.5 × 9.5	140 ± 7	46 ± 3
	5.0 × 9.0	172 ± 6	49 ± 2
	4.5 × 8.5	183 ± 20	48 ± 3

[1]Binary: 5Al/3NiO blend; [2]Ternary: 60 wt-% (5Al/3NiO) + 40 wt-% (Al/Ni); [3]Width × Depth.

Table 4-2 provides a comparison of the combustion rate of the two samples selected in this section. The binary blend consisted of 35 wt-% Al and 65 wt-% NiO (5 Al +3 NiO), whereas

the ternary composition contained 60 wt-% (5 Al + 3 NiO) and 40 wt-% (Al + Ni). The compact density was 40 ± 1 % and 54 ± 1 % TMD in glass tubes and lead tubes, respectively. The measured burning rates in the lead tubes were slightly slower than those in the glass tubes. Moreover, the lead housings were badly damaged due to the lower melting point of the lead and higher burning temperature. The remarkable results obtained, that it was somehow faster to burn in both glass and lead tubes with a smaller inner diameter, would be explained in the latter part of the thesis.

The excessive heat generated by the binary mixture caused the lead tubes to melt completely. This only happened after the very fast burning front had passed through. In contrast, the tubes containing the ternary mixture remained intact. This was expected since this combined thermite-intermetallic system features a much lower adiabatic temperature.

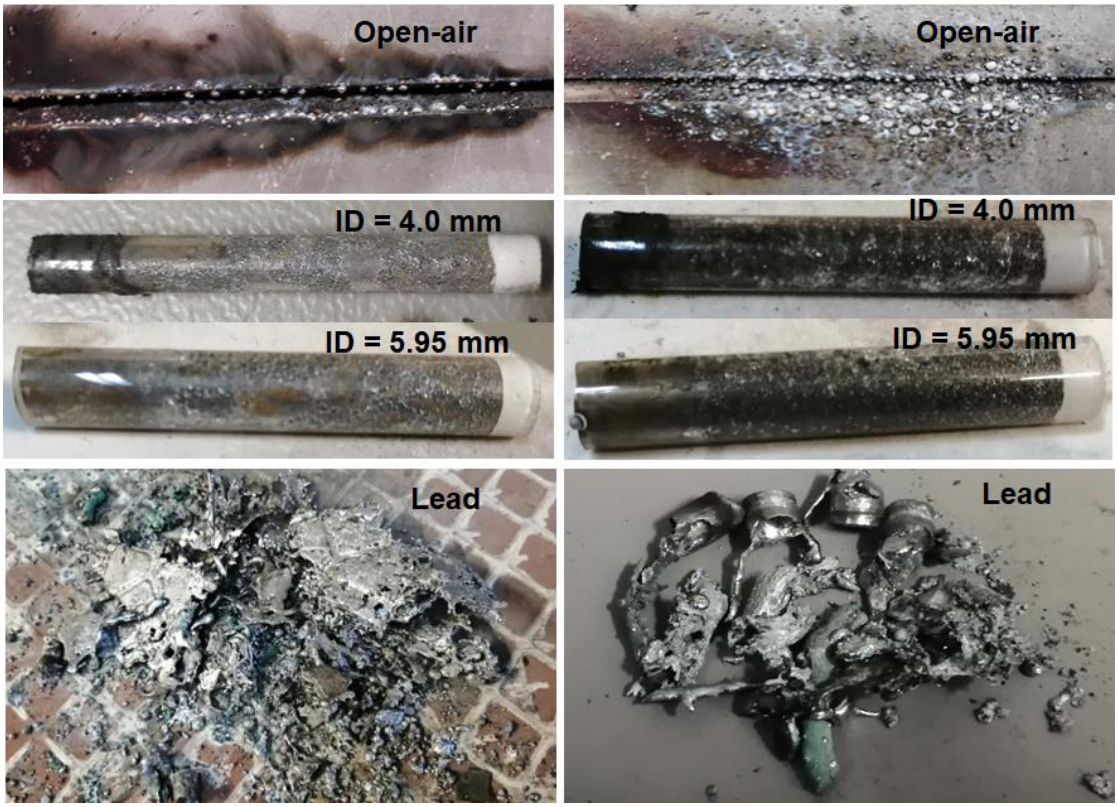

Figure 4-7： Photographs of the residues after complete combustion under various conditions: open-air burning (upper), glass-tube burning (middle) and lead-tube burning (bottom); the left side refers to a 5Al/3NiO blend and the right to a ternary blend containing 60 wt-% (5Al/3NiO) with 40 wt-% (Al/Ni); the ID of lead tubes tested was increased from left to right in each bottom image.

Photographs were taken after the burning events, as shown in **Figure 4-7**. The lead tubes melted completely when a very fast combustion front passed through, due to the excessive heat produced by the binary blend. However, the lead tubes with the ternary sample remained

partially intact. This was caused by the fact that the heat generated was slower than the binary sample, which was attributed to a lower adiabatic reaction temperature of the nature of the combined thermite-intermetallic system.

4.1.4 XRD Results of Residues

The XRD results can be found in **Figure 4-8**. Contaminated reflections were posted in the window due to the original shape and hardness of the burning residues collected after the completed combustion in the glass tube. Before scanning, the residual slags should be milled into fine powders using tungsten carbide (WC). As a whole, the XRD results are qualitatively consistent with the EKVI simulation results. At 20 wt-% Al fuel loading, the reduced and oxidised products were Ni metal(2θ = 52.2° and 61.1°) and alumina (2θ = 29.9°, 41.1° and 50.9°). The occurrence of the Ni_3Al (2θ = 51.5° and 60.1°) and NiAl (2θ = 36.5° and 52.4°) phase was evident in the burn residues obtained with 25 wt-% and 35 wt-% Al fuel loading, respectively. At 50 wt-% and Al as a fuel, additional intermetallic phases, including $NiAl_3$, NiAl and Ni_2Al_3, were observed. This may be attributed to the presence of the unreacted Al and phase transfer during the cooling process.

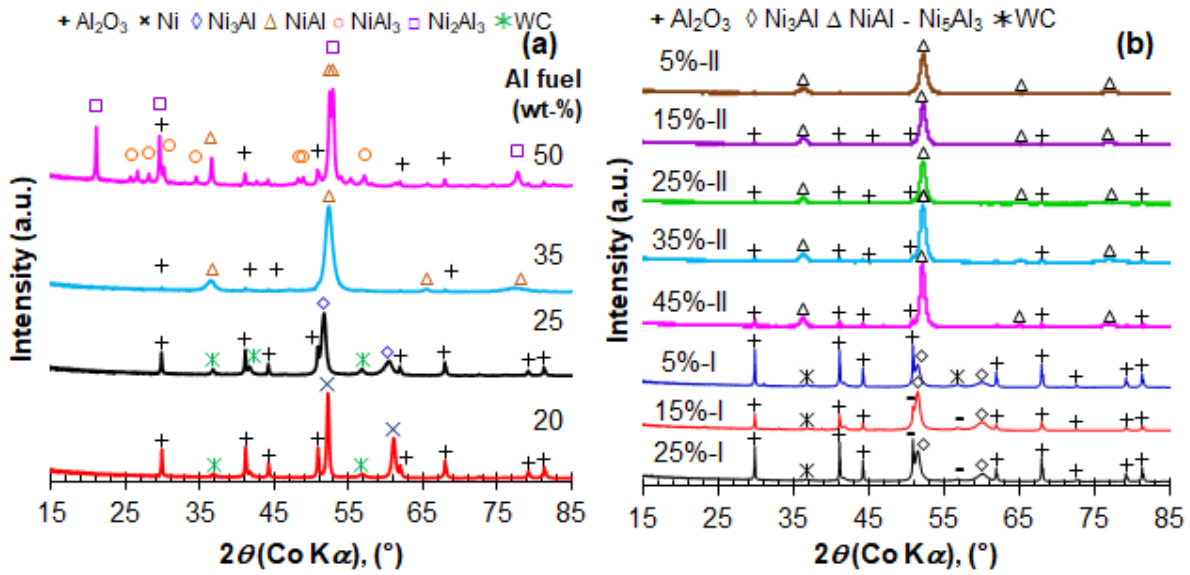

Figure 4-8: XRD spectrum for residues collected after combustion of Al-NiO binary blend (a) and Al-NiO-Ni ternary mixtures (b) in glass tubes

Intermetallic products produced from the ternary system, NiAl, Ni_3Al and Ni_5Al_3, were observed in **Figure 4-8(b)**. For the ternary **I** system, the dominant intermetallic Ni_3Al (2θ = 51.5° and 60.1°) was detected at 5 wt-% with Al/3Ni mixtures as an additive. Remarkably, the presence of Ni_5Al_3 (2θ= 50.8° and 56.8°) makes it evident that phase transfer happened during the cooling process when the mass fraction of the Al/3Ni mixtures were less than 70

wt-% (Robertson and Wayman, 1984), while for the ternary **II** system, the dominant products are only NiAl and Al_2O_3.

4.2 Sn-Bi_2O_3-Mn TERNARY SYSTEMS

4.2.1 Powder Characteristics

None of the reagents used have undergone further processing. **Figure 4-9** shows the particle size distribution and the X-ray diffraction (XRD) spectrum of the bismuth trioxide, manganese and tin. All three reactants have a narrow particle size distribution range, and the D_{50} particle sizes for the Bi_2O_3, Mn and Sn powders are 7.48 ± 0.09 μm, 24.6 ± 0.3 μm and 4.25 ± 0.08 μm, respectively. The median diameter of the manganese powder correlate with the large size revealed by the SEM images.

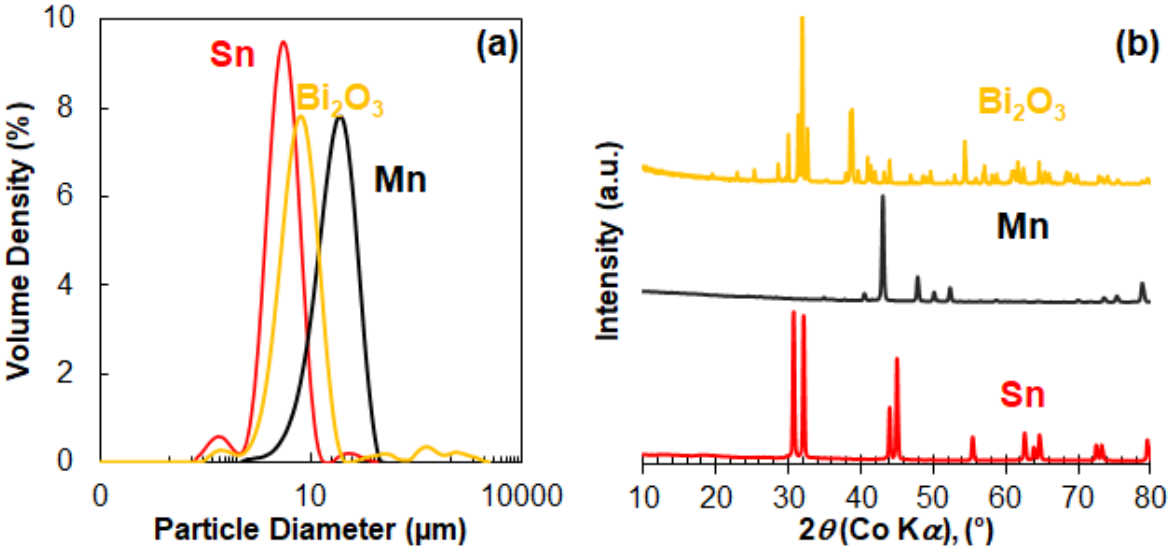

Figure 4-9： The particle size distribution (a) and the XRD results for bismuth trioxide, manganese and tin (b)

X-ray diffraction analysis established the high purity of the starting reagents, with the two metallic reagents containing more than 99 wt-% main element and 96 wt-% for the monoclinic Bi_2O_3 (namely bismite). The major elementary impurities present were phosphorus and platinum astonishingly for the oxide, lead and molybdenum for Sn, and sodium for Mn (**Table 4-3**).

Table 4-3： XRF analysis results for the Bi_2O_3, Mn and Sn powders used (values are given in wt-%)

Bi_2O_3	P_2O_5	PtO_2	CaO	As_2O_3	Rb_2O	Na_2O	ZrO_2	Ag_2O
96.05	1.08	1.020	0.704	0.441	0.183	0.167	0.156	0.042
MoO_3	PuO_2	SrO	K_2O	TiO_2				**Total**
0.034	0.026	0.019	0.016	0.010				**99.95**
Mn	Na	Mg	Tb	Sm	Al	Si	Bi	Ni
99.52	0.15	0.08	0.06	0.05	0.03	0.02	0.01	<0.01
Sn	Ca	Fe	Co	Cu	Hf	Pb	Mo	**Total**
<0.01	<0.01	<0.01	<0.01	<0.01	<0.01	<0.01	<0.01	**99.90**
Sn	Pb	Mo	Mn	Ni	Bi	Al	Fe	Si
99.35	0.22	0.11	0.03	0.03	0.03	0.02	0.02	0.01
Na	Mg	Ca	Co	Cu	Sm	Tb	Hf	**Total**
<0.01	<0.01	<0.01	<0.01	0.03	<0.01	<0.01	<0.01	**99.83**

The scanning electronic microscope images of these three starting reagents are shown in **Figures 4-10 (a)-(d)**. The findings are summarised as follows:

(i) **Figures 4-10 (a) - (b)** indicate that the manganese has a considerably large, irregular particle shape with sharp contours, while some small and needle-like crystals were found on the surfaces of larger powders when observed at higher magnifications.

(ii) **Figure 4-10 (c)** showed that the Bi_2O_3 powders have a smooth surface and irregular shapes and different sizes.

(iii) **Figure4-10 (d)** demonstrated that the Sn powders have a smooth surface with a spherical shape and slight aggregation caused by the smaller primary particles when the SEM images are carefully examined.

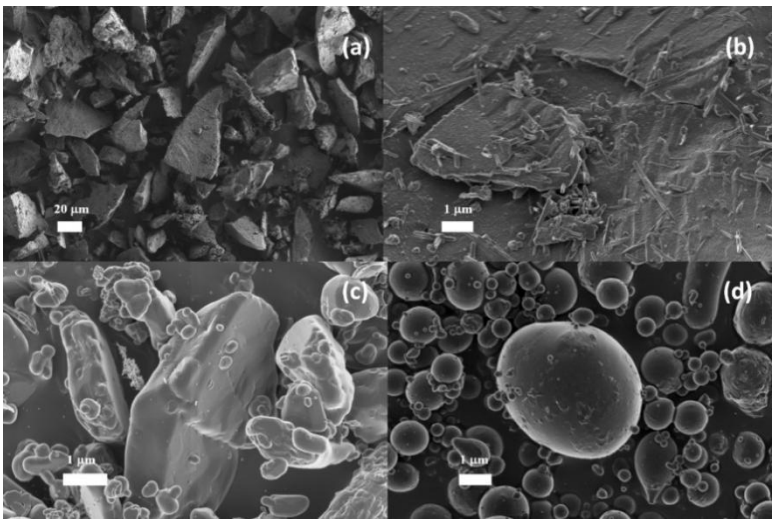

Figure 4-10： Scanning electron micrographs of the manganese (a, b), bismuth trioxide(c), and tin particles (d)

4.2.2 EKVI Simulations

4.2.2.1 Typical thermite binary systems

Two typical thermite binary systems are described in this part, namely Sn-Bi_2O_3 compositions and Mn-Bi_2O_3 compositions.

***Sn-Bi_2O_3 thermite system*.** The EKVI simulation results, including the adiabatic reaction temperature and the condensed products fraction, are shown in **Figures 4-11 (a) - (b)**. T_{ad} rose sharply as the fuel loading increased in the first stage. When the fuel loading reached 26.75 wt-%, the oxide diminished and the peak of T_{ad} occurred approximately at 1756 K, implying a stoichiometric reaction **4-III** (3 Sn + 2 Bi_2O_3 → 4 Bi + 3 SnO_2, shown in **Table 4-11**). Meanwhile, the peak temperature of this binary system was predicted to be ca. 1769 K at 27 wt-% Sn loading when using Factsage software (Shaw, 2020). This small difference could be due to differences in information in the databases used by the different software. The main reaction was similar for both software (3 Sn + 2 Bi_2O_3 → 4 Bi + 3 SnO_2). Meanwhile, the maximum local value of the solid fraction (34.93 wt-%) was generated. Along with the peak of the Bi curve, a certain amount of Bi and Bi_2 gas were generated at this stage (see **Figure 4-11 (b)**). When in excess of the stoichiometric amount of the fuel, T_{ad} dropped sharply and went on a small plateau (the fuel content within the range of 30 - 38 wt-%). In this range, the system had excess Sn and there was no oxide for it to react with. Based on the EKVI simulations, the temperature plateaus possibly occurred as a result of phase change of Sn from a solid to a liquid. Then, it kept falling linearly as the fuel content increased. The unreacted Sn was detected in the product window at this stage.

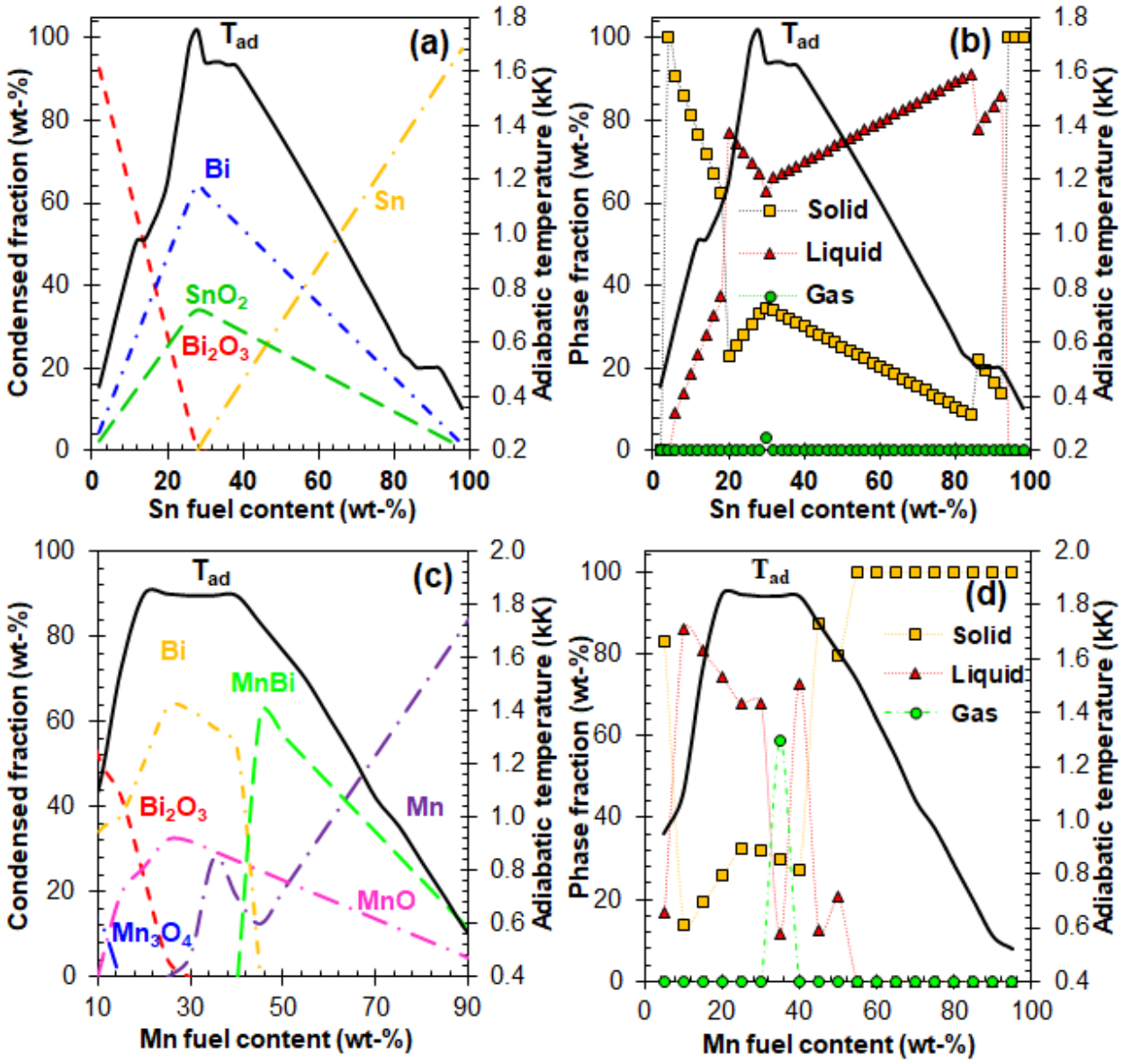

Figure 4-11: EKVI simulation results of typical thermite binary systems: the adiabatic reaction temperature and reaction products (a); the phase amount fraction (b) for the Sn-Bi_2O_3 compositions; the adiabatic reaction temperature and reaction products (c); and the phase amount fraction (d) for the Mn-Bi_2O_3 compositions.

***Mn-Bi_2O_3 thermite system*. Figures 4-11 (c) - (d)** summarise the calculated theoretical plots consisting of the adiabatic reaction temperature, condensed products and phase fraction as a function of the Mn fuel content. It was apparent that a wider plateau of the adiabatic reaction temperature (approximately 1836 K) occurred at a fuel range of 20 to 40 wt-%, corresponding to the formation of the main reduced products (Bi and MnBi). The stoichiometric reaction **4-IV**, 3 Mn + Bi_2O_3 → 2 Bi + 3 MnO (see **Table 4-11**), reacted at ca. 26.1 wt-% Mn and the predicted temperature was ca. 1844 K. Meanwhile, the peak temperature of this binary system was predicted at ca. 1843 K at 26 wt-% Mn loading when

using Factsage software (Shaw, 2020). This small difference could be due to differences in information in the databases used by the different software. But it had no effect on the predicted stoichiometric reaction (3 Mn + Bi_2O_3 → 2 Bi + 3 MnO). The maximum amount of Bi obtained here and certain bismuth gases (Bi and Bi_2) occurred simultaneously (see **Figure 4-11(d)**). After this point, Mn that did not react at lower concentration began to react in the system. However, the intermetallic-type reaction **4-V**, 5 Mn + Bi_2O_3 → 2 MnBi + 3 MnO (see **Table 4-11**), occurred at ca. 37.1 wt-% Mn. Although Mn_3O_4 was generated at less than 15 wt-% Mn, the principal oxidised product was MnO. Meanwhile, T_{ad} fell linearly while the amount of fuel content rose.

4.2.2.2 **Typical intermetallic binary systems**

In this part, there are only two intermetallic binary systems, Mn-Sn and Mn-Bi. For the Sn-Bi system, no intermetallic products were estimated from the software and they were not proven from the binary phase diagram (Mei and Morris, 1992; Lee et al., 1996).

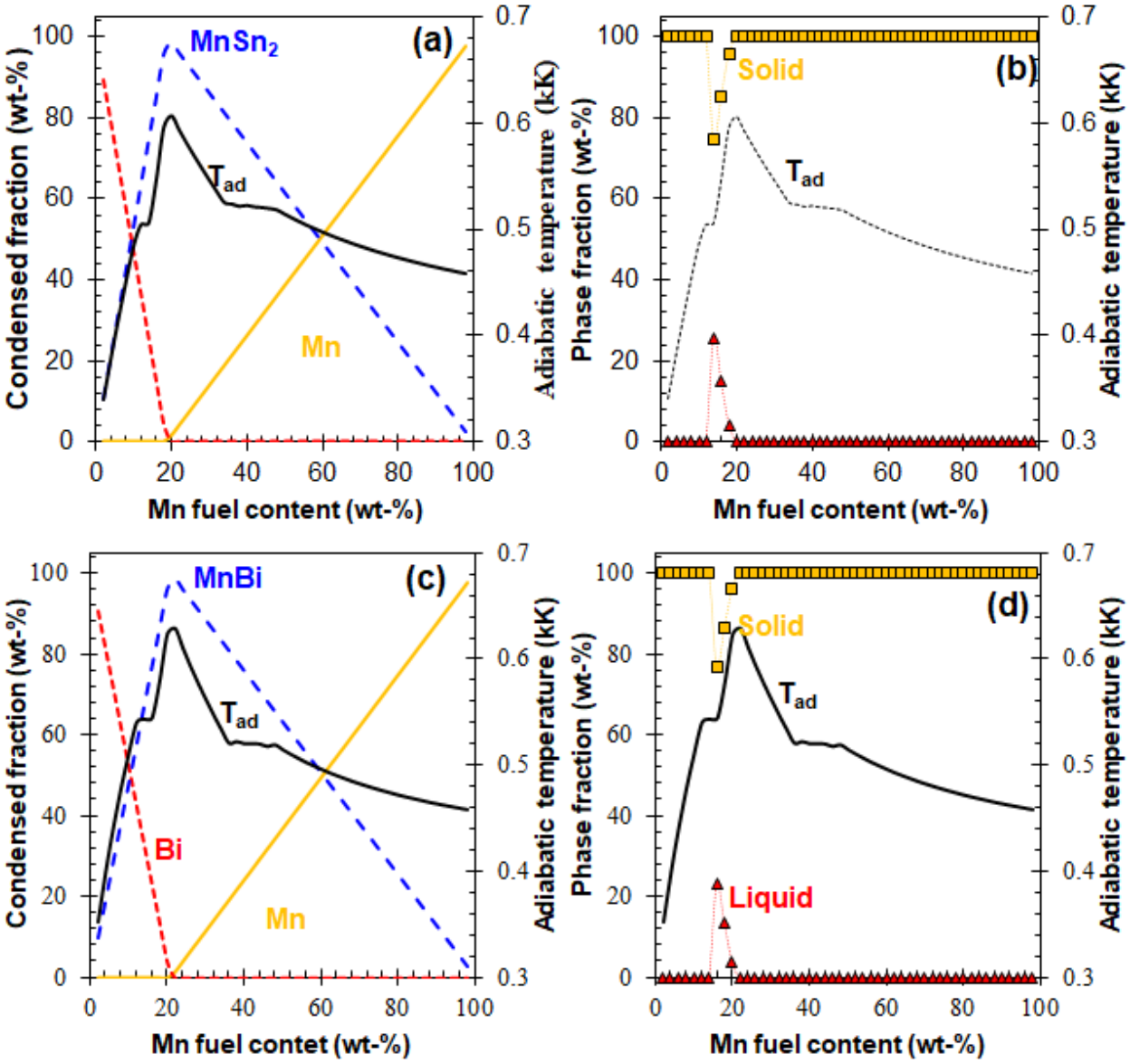

Figure 4-12: EKVI simulation results of the typical intermetallic binary systems: (a) the adiabatic reaction temperature and reaction products; (b) the phase amount fraction for the Sn-Bi_2O_3 compositions; (c) the adiabatic reaction temperature and reaction products; (d) the phase amount fraction for the Mn-Bi_2O_3 compositions

Figures 4-12 (a)-(d) provide the EKVI simulation results for two intermetallic-type binary systems (Mn-Sn and Mn-Bi). Remarkably, these two mixtures demonstrated a similar pattern in the adiabatic reaction temperature and the phase fraction based on Mn content. The peak of the T_{ad} plot was 606 K and 628 K at ca. 18.8 wt-% and 20.8 wt-% Mn, respectively, corresponding to the stoichiometric reactions Mn + 2 Sn → $MnSn_2$ and Mn + Bi → MnBi, respectively (see **Figures 4-12 (a) - (c)**). While other intermetallic manganese-tin products appeared in its phase diagram, such as Mn_3Sn and Mn_3Sn_2 (Okamoto, 1999), only $MnSn_2$ can be located in the EKVI database. Only a narrow range of the Mn loading demonstrated the

state of solid-liquid coexistence, and the maximum adiabatic temperature occurred in the solid state (see **Figures 4-12 (b) - (d)**).

4.2.2.3 Sn-Mn-Bi_2O_3 ternary system

Figures 4-13 (a)-(b) show the EKVI simulation results which indicate the effect of the reagents on the adiabatic reaction temperature for the theoretical design of the ternary systems. The reagents used to design these systems are listed in **Table 4-4**. Interestingly, the adiabatic reaction temperature was constant at around 1836 K for the ternary **II** system (composed of reactions **4-III** and **4-IV**). It agreed well with the experimental combustion rate that the combustion was interrupted before reaching the end of the glass tubes when the Bi_2O_3 content was more than ca. 70 wt-% overall for the systems. The coloured symbols shown in **Figure 4-13 (a)** indicate the binary compositions that ignited and burned completely in the glass tubes; however, the black -▲- indicates the interrupted burning of Mn/Bi_2O_3 system in the glass tubes.

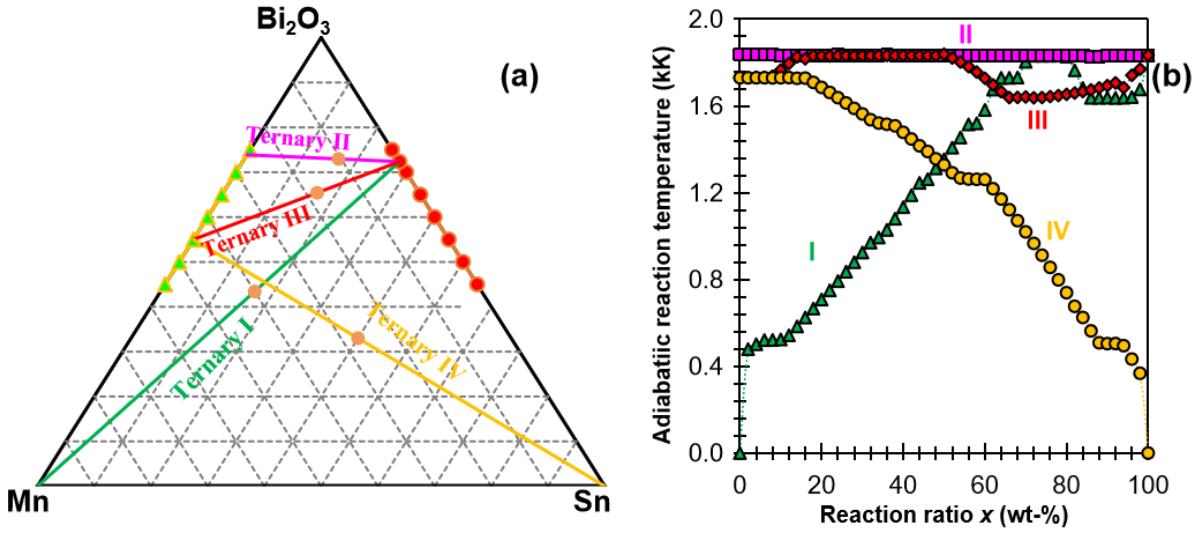

Figure 4-13: (a) Theoretical design for the Sn/Mn/Bi_2O_3 ternary systems; (b) different factors of the metal or binary blend on the projected adiabatic reaction temperature of the EKVI simulations. The symbols (-○- and -Δ-) indicate that the Sn/Bi_2O_3 and Mn/Bi_2O_3 compositions burned completely.

T_{ad} for the ternary II system was in the range of ca. 1833 K – 1836 K (may be considered as a constant), while a visibly varying trend is shown for other ternary systems in **Figure 4-13 (b)**. Based on the EKVI results, the dominant predicted products were Sn, Mn, Bi, MnO and SnO_2, as well as some amount of intermetallic MnBi and $MnSn_2$. When only metallic material was added, the varying trend of T_{ad} was dependent on the melting point of the added metals, of which T_{ad} increased as Mn with a high melting point (1519 K) increased in the ternary **I** system, while T_{ad} decreased as Sn with a low melting point (505.08 K) increased in the

ternary **IV** system. When T_{ad} was less than 1730 K, the combustion flame in the glass tubes were interrupted based on the experimental data at a Bi_2O_3 content of less than ca. 49 wt-% (see **Figure 4-14**). All the ternary **III** compositions ignited and burned successfully through the glass tubes.

Table4-4： The projected reagents inferred from the different systems in the EKVI simulations

System	Binary I	Binary II	Binary III	Ternary I	Ternary II	Ternary III	Ternary IV
Reagent I wt-%	Sn 27.65 %	Mn 26.13%	Mn 45 %	Binary I *x* %	Binary I *x* %	Binary I *x* %	Binary III *x* %
Reagent II wt-%	Bi_2O_3 72.65 %	Bi_2O_3 73.87 %	Bi_2O_3 55 %	Mn (1-*x*) %	Binary II (1-*x*) %	Binary III (1-*x*) %	Sn (1-*x*) %

4.2.3 Burning Rate

Table 4-5 lists the values of the experimental burning rates and the compaction density, expressed as the theoretical maximum density (TMD), for all the samples tested in glass tubes. Two thermites were prepared using Sn and Mn fuels and Bi_2O_3 as the oxidiser. For the Sn-Bi_2O_3 binary system, 8 samples were prepared with the Bi_2O_3 contents ranging from 45 to 75 wt-% and compacted at a density of approximately 45.2 ± 0.5 %. The fastest burning rate was 13.7 ± 1.1 mm·s^{-1} at a Bi_2O_3 content of 70 wt-%, and the slowest rate was 3.8 ± 0.7 mm·s^{-1} at 45 wt-% Bi_2O_3. For the Mn-Bi_2O_3 binary system, only 4 samples were prepared with the Bi_2O_3 content ranging from 60 to 75 wt-%, and the compaction density was maintained around 47.3 ± 0.2 %. The fastest burning rate was 11.2 ± 0.8 mm·s^{-1} at a Bi_2O_3 content of 70 wt-% and the slowest rate was 6.3 ± 1.8 mm·s^{-1} at a Bi_2O_3 content of 60 wt-%. When measuring the combustion rate in open air, successful ignition and combustion performance were detected in the Mn-Bi_2O_3 binary system with an oxidant content in a range of 45 to 75 wt-%. The slowest combustion rate in open air was 2.5 mm·s^{-1} for a sample containing 45 wt-% Bi_2O_3 (**Table 4-6**). However, the combustion flame was quenched when it travelled down the glass tubes, even with an ID of 6.0 mm when the Bi_2O_3 loading was lower than ca. 60 wt-%.

Table 4-5： Burning rates and compaction density of samples tested in glass tubes

Composition, wt-%			Burning rate, $mm \cdot s^{-1}$	Compaction, %	Energy output
Bi_2O_3	Mn	Sn	$u \pm \sigma$	TMD $\pm \sigma$	$MJ \cdot kg^{-1}$
75	0	25	12.1 ± 1.2	45.0 ± 0.2	
72.4	0	27.7	12.7 ± 0.5	45.0 ± 0.0	0.484 ± 0.008
70	0	30	13.7 ± 1.1	45.2 ± 0.8	0.464 ± 0.026
65	0	35	13.4 ± 0.6	45.2 ± 0.8	0.479 ± 0.029
60	0	40	9.5 ± 0.6	45.0 ± 0.2	0.444 ± 0.027
55	0	45	9.4 ± 0.1	45.3 ± 0.9	
50	0	50	7.0 ± 0.8	45.3 ± 1.0	
45	0	55	3.8 ± 0.7	45.5 ± 1.3	
75	25	0	8.0 ± 0.4	47.6 ± 0.4	0.95
70	30	0	11.2 ± 0.8	47.8 ± 0.4	1.04
65	35	0	8.9 ± 1.2	47.6 ± 0.1	1.15
60	40	0	6.3 ± 1.8	47.9 ± 0.1	0.92
56.7	40.5	2.8	2.9 ± 0.6	50.6 ± 0.4	
50	35	15	3.0 ± 0.1	51.8 ± 0.5	
56.5	40.5	3	3.2 ± 0.3	49.9 ± 0.1	
49.5	42.4	8.1	3.4 ± 0.3	50.5 ± 0.3	0.823
49.5	40.5	10	3.5 ± 0.4	50.5 ± 0.4	
59.3	33.8	6.9	3.6 ± 0.1	52.3± 2.7	
62.5	22.5	15	4.0 ± 0.2	49.7 ± 0.7	0.832 ± 0.023
50	20	30	4.0 ± 0.2	49.1 ± 0.3	
63.7	22.5	13.8	4.1 ± 0.7	49.6 ± 0.5	0.921 ± 0.030
54	23	23	4.4 ±0.4	48.7 ± 0.2	
56	27	17	4.5 ± 0.1	48.7 ± 0.2	
50	30	20	4.6 ± 0.2	50.6 ± 0.3	
58.7	33.8	7.5	4.6 ± 0.9	50.2 ± 0.2	0.977 ± 0.008
56	17	27	5.1 ± 0.3	47.3 ± 0.1	
68	11.3	20.7	5.5 ± 0.5	46.7 ± 0.2	
66.3	11.3	22.5	6.8 ± 0.3	49.4 ± 0.9	0.788 ± 0.052
68.5	4.5	27	9.4 ± 0.9	46.3 ± 0.2	
63	1.9	35.1	10.5 ± 0.4	46.4 ± 0.3	0.824 ± 0.010
63	10	27	10.9 ± 0.8	46.7 ± 0.2	
50	10	40	-	-	
46	37	17	-	-	
46	27	27	-	-	
46	17	37	-	-	

In addition, 23 ternary samples were tested in the glass tubes, with the compaction density varying from 46.3 ± 0.2 % to 52.3 ± 2.7 %. This was attributed to the mixing levels and the theoretical maximum density based on different mass fraction of the reagents. The fastest and slowest combustion rates obtained were 10.9 ± 0.8 $mm \cdot s^{-1}$ and 2.9 ± 0.6 $mm \cdot s^{-1}$, respectively.

Table 4-6： Burning rates of the Sn-Bi_2O_3 and Mn-Bi_2O_3 binary compositions in open air

Composition, wt-%			Burning rate, $mm \cdot s^{-1}$
Bi_2O_3	Mn	Sn	$u \pm \sigma$
80	0	20	4.4 ± 0.4
75	0	25	20.8 ± 0.5
72.4	0	27.7	59.8 ± 4.4
70	0	30	104.5 ± 0.6
65	0	35	66.2 ± 12.3
60	0	40	45.3 ± 8.0
55	0	45	22.0 ± 3.9
50	0	50	13.4 ± 0.4
45	0	55	8.3 ± 0.3
75	25	0	9.3 ± 1.6
70	30	0	11.0 ± 1.5
65	35	0	8.9 ± 1.7
60	40	0	8.1 ± 1.2
55	45	0	6.6 ± 0.6
50	50	0	3.5 ± 0.2
45	55	0	2.5 ± 0.2

Table 4-7： Comparison of the burning rates obtained in glass and lead tubes

	Formulation:	**A**	**B**	**C**	**A+C (1:1)**	**B+C (1:1)**
Composition	Bi_2O_3	73.25	70.0	55.0	63.7	62.5
	Mn	-	-	45.0	22.5	22.5
	Sn	26.75	30.0	-	13.8	15
Open burn	*u*, $mm \cdot s^{-1}$	60 ± 5	105 ± 1	6.6 ± 0.6	16 ± 4	18 ± 7
Glass tubes	*u*, $mm \cdot s^{-1}$	12.7 ± 0.5	13.7 ± 1.1	-	4.1 ± 0.6	4.0 ± 0.2
	TMD, %	45.1 ± 0.0	45.2 ± 0.6	-	49.6 ± 0.4	49.7 ± 0.2
Lead tubes	*u*, $mm \cdot s^{-1}$	17.7 ± 1.4	14.5 ± 0.8	-	6.5± 1.0	6.5 ± 0.8
	TMD, %	40.4	42.8	-	48.1	44.6

Table 4-7 lists the details of the selected binary blends and a comparison of the experimental combustion rates conducted in the glass and lead tubes. The selection principle was a specific fuel-oxide ratio where the maximum mass fraction of SnO_2 and MnBi was produced in Sn-Bi_2O_3 and Mn- Bi_2O_3 binary systems, respectively. They are the stoichiometric ratio of the Bi_2O_3-Sn binary and the detected mass ratio of the intermetallic product MnBi for the Bi_2O_3-Mn binary mixture. All the formulations selected burnt somewhat slower in the glass tubes than those in the lead tubes. This result was attributed to the materials of the tube wall: the thermal conductivity of glass and lead were 1 $W \cdot m^{-1} \cdot K^{-1}$ and 35 $W \cdot m^{-1} \cdot K^{-1}$, respectively.

Along the combustion route, the heat transfer was faster in the lead tubes and the burning rate in the lead tubes was relatively higher than that in the glass tubes.

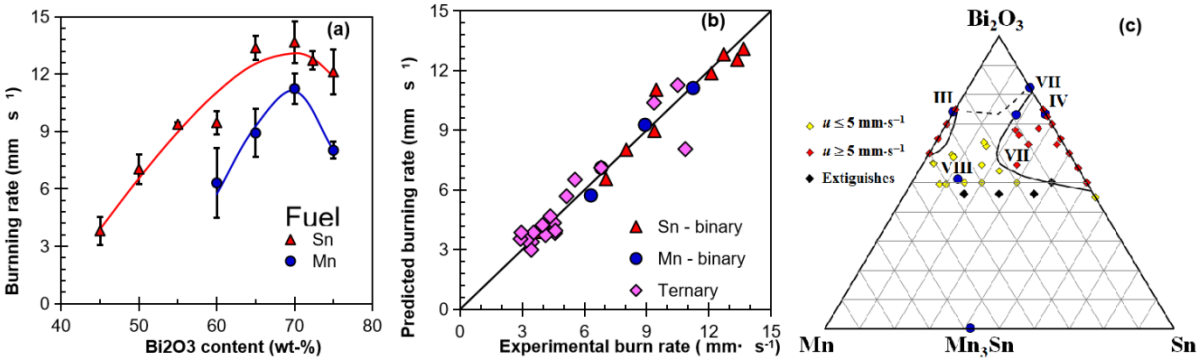

Figure 4-14: (a) Effect of the mass proportion of oxide on the burning rates of the Bi_2O_3-Sn and Bi_2O_3-Mn binaries; (b) comparison of the combustion rates predicted by the Padè mixture model; (c) the experimental formulations plotted (solid and broken lines) and the dominant reactions (Roman numbers) shown in the ternary diagram

Figure 4-14 (a) shows the effect of the variation of mass fraction of the oxide in binaries on the burning rates of the composition. The burning rates illustrate highly non-linear variation with the binary mixtures. Both binaries feature a maximum burning rate at a Bi_2O_3 content of ca. 70 wt-%. Compositions based on tin as the fuel burn slightly faster and over a wider stoichiometric range. The lowest burning rate measured of binary systems was just 3.8 $mm \cdot s^{-1}$. Padè mixture models are families of rational polynomials based on Scheffe K-polynomials (Focke & Du Plessis, 2004). They are eminently suitable for correlating complex mixture property behaviour (Focke, 2007, Focke and Du Plessis, 2004). Consequently, the data were correlated using the Padè mixture model shown in equation 4-1:

$$u = \sum_{i,j,k} a_{ijk} w_i w_j w_k \Big/ \sum_{i,j} b_{ij} w_i w_j$$
$$= \begin{pmatrix} a_{111}w_1^3 + 3a_{112}w_1^2 w_2 + 3a_{113}w_1^2 w_3 + \\ a_{222}w_2^3 + 3a_{122}w_1 w_2^2 + 3a_{223}w_2^2 w_3 + \\ a_{333}w_3^3 + 3a_{133}w_1 w_3^2 + 3a_{113}w_2 w_3^2 + 6a_{123}w_1 w_2 w_3 \end{pmatrix} \Big/ \begin{pmatrix} b_{11}w_1^2 + b_{22}w_2^2 + b_{33}w_3^2 + \\ 2a_{12}w_1 w_2 + 2a_{13}w_1 w_3 + 2a_{123}w_1 w_2 w_3 \end{pmatrix} \quad (4\text{-}1)$$

where u is the burning rate in $mm \cdot s^{-1}$ and the w_i is a mass fraction of each component corresponding to the ternary system Bi_2O_3 (1) - Mn (2) - Sn (3). a_{ijk}s and b_{ij}s are adjustable model constants. In this model, the ratios a_{iii}/b_{ii} indicate the contribution of component i to the burning rate while the parameters quantify interactions between the components. Note that the parameter values in this model are, in a relative sense, not completely independent variables. Therefore, the constant b_{33} was assigned a value of unity to fix their relative magnitudes. The values for the other constants were established using the least squares

regression shown in **Table 4-8**. The correlation coefficient was 0.974 (seen in **Figure 4-14 (b)**).

Table 4-8： Mixture model coefficients

a_{111}	a_{112}	a_{113}	a_{221}	a_{222}	a_{223}
-0.849	1.099	-1.069	-0.060	-2.737	6.485
a_{331}	a_{332}	a_{333}	a_{123}		
13.685	-7.616	-23.900	-1.558		
b_{11}	b_{22}	b_{33}	b_{12}	b_{13}	b_{23}
0.00000	0.10765	1.00000	0.00010	0.00004	0.26929

Figure 4-14 (b) shows plots that compare the experimentally determined burning rates with the predictions of the model. The mean absolute deviation was 12 % and the maximum deviation was 16 %. It is evident from **Figure 4-14 (b)** that there is an outlier in the data set that was nevertheless included in the regression analysis. The lowest burning rate measured of all samples was 2.9 $mm \cdot s^{-1}$.

Figure 4-14 (c) plots the experimental formulations on a ternary composition diagram that burned in the glass tubes. The solid and broken lines indicate the model-predicted contours of the constant burning rate corresponding to u = 5 $mm \cdot s^{-1}$ and u = 0 $mm \cdot s^{-1}$ (flame extinction), respectively. The Roman numbers indicate the reagent ratios corresponding to the reaction schemes shown in **Table 4-11**. The plotted burning rates are colour-coded according to whether the measured burning rate was less or higher than u = 5 $mm \cdot s^{-1}$. Also shown are model-predicted contours for a constant burning rate at this value, as well as the predicted contour for interrupted burning. Interestingly, the model predicts that, with both fuels present, burning is sustained at lower oxidant concentrations than are possible with the binary systems. Also, compositions based on mixtures of the two metal fuels also tend to burn slower. The actual ternary compositions tested confirmed these two conclusions. Therefore, both the experimental data and the model support the expectation that reliable burning rates lower than u = 5 $mm \cdot s^{-1}$ should be possible in this composition range.

In the ternary system, slow-burning pyrotechnic compositions comprising bismuth trioxide as the oxidant and manganese and tin as the fuels were found. The binary systems behaved as expected for standard thermite reactions in which the bismuth trioxide is reduced to the metal and the oxides MnO or SnO_2 are formed. The reaction products in the ternary system depend strongly on the relative proportions of the reagents. Manganese is preferentially oxidised

compared to tin. If sufficient oxidiser is present, both fuels are oxidised and manganese stannate forms instead of the separate metal fuel oxides. At low manganese and very high Bi_2O_3 contents, the formation of bismuth stannate was observed. At high manganese-to-bismuth ratios and low oxidiser contents, the intermetallic compound Mn_3Sn was formed. The slowest burning compositions were those associated with the formation of this intermetallic compound.

4.2.4 XRD Results of Residues

Tables 4-9 and **4-10** present the results of the XRD analysis of the combustion residues removed from the glass tubes. The primary products of the Sn-Bi_2O_3 compositions are metal Bi and SnO_2, based on the data of samples A3 to A6 in **Table 4-9**, correspond to the Scheme **4-III** in **Table 4-11**. For Mn-Bi_2O_3 mixtures, the primary products are metal Bi and MnO at a Mn fuel content of less than 40 wt-%; they will be MnO and MnBi at a fuel loading of more than 45 wt-%. These reactions are explained by the Scheme **4-IV** and **4-V** in **Table 4-11** respectively. This confirms that the formation of MnBi required a greater fuel content in the binary composition (Tichapondwa et al., 2021). The Schemes **4-III** and **4-IV** are the classic thermite-type reactions in which the metal fuel is oxidised into its most stable oxide while the bismuth trioxide is reduced to the metal state. The generation of MnBi confirms that more Mn reacted following the production of metal Bi, which is explained by the typical intermetallic thermitic reaction. This is consistent with the EKVI simulations to a certain extent.

For the ternary Sn-Mn-Bi_2O_3 compositions, sample A1 confirms that Mn is oxidised preferably and completely as only MnO was detected (no SnO_2) and Sn did not react. At higher concentrations of bismuth trioxide, the reaction with Sn yields bismuth stannate ($Bi_2O_3 \cdot 2SnO_2$) as shown in Scheme **4-VI.** This was noted for sample A11 in **Table 4-11**. For samples A7 to A10 in **Table 4-9**, the formation of manganese stannate ($2MnO \cdot SnO$) was led by similar amounts of the two fuels when reacted with the bismuth trioxide (see Scheme **4-VII** in Table **4-11**). Although there are many manganese-tin intermetallic compounds based on the phase diagram of manganese-tin, only Mn_3Sn was detected as a reaction product. It was produced when the tin proportion was significantly less than that of the manganese. Some of the manganese was oxidised to MnO and the rest reacted with the tin to produce the intermetallic product as shown in Scheme **4-VIII** in **Table 4-11**. This occurred as a primary reaction compound from the XRD product spectra for compositions **B1** to **B6** in **Table 4-10**.

It is worth noting that these six samples had the slower burning rates which were less than 5 $mm \cdot s^{-1}$.

Table 4-9： Compositions with oxides or metal stannates as products

Reagents	**A1**	**A2**	**A3**	**A4**	**A5**	**A6**	**A7**	**A8**	**A9**	**A10**	**A11**
Bi_2O_3	62.5	63.7	72.4	70.0	60.0	50.0	68.5	68.0	66.2	63.0	63.0
Mn	22.5	22.5					4.5	11.3	11.3	10.0	5.8
Sn	15.0	13.8	27.7	30.0	40.0	50.0	27.0	20.7	22.5	27.0	31.2
Products											
Bi	**51.5**	**46.1**	**33.9**	**36.7**	**43.4**	**43.9**	**45.8**	**52.0**	**30.7**	**56.9**	**46.2**
MnO	**41.0**	**34.6**					1.2	2.1	2.0	1.1	
SnO_2			**45.1**	**46.5**	**48.5**	**29.8**	**33.8**	**12.5**	**16.6**	**7.9**	**35.1**
$2MnO{\cdot}SnO_2$		4.9					**10.0**	**28.5**	**46.9**	**24.6**	
$Bi_2O_3{\cdot}2SnO_2$			1.0	2.1	3.2		2.2				**18.2**
Unreacted reagents											
Bi_2O_3		**5.6**	**20.0**	**14.6**	**4.9**		**7.1**		0.9		
Sn	**7.5**					**26.4**		1.6		**9.4**	0.5
Mn								0.1			
Minor products											
$Bi_{0.05}Sn_{0.95}$		8.9							3.0		
$MnO{\cdot}SnO_2$								3.3			

4.2.5 Energy Output

Table 4-5 also shows the energy outputs, determined by the bomb calorimeter, for selected formulations. The energy of reaction (ΔH) for the Bi_2O_3-Sn binary compositions changed slightly. It varied from 0.44 to 0.48 $MJ{\cdot}kg^{-1}$ as the Bi_2O_3 content increased from ca. 55 to 72 wt-%. These values were almost half those of the other binary compositions. The energy of the reaction of the Bi_2O_3-Mn binary blends decreased from 1.15 to 0.53 $MJ{\cdot}kg^{-1}$ as the oxidant content increased from 45 to 70 wt-% (Tichapondwa et al., 2021). The values of the energy outputs conducted for the Bi_2O_3-Mn-Sn ternary compositions are also around those values for the Bi_2O_3-Mn binary blends. It is surmised that the secondary exothermic reaction occurs as both fuels are assumed to be still present in the mixtures after the first exothermic reaction, such as the reactions **4-VII** and **4-VIII** in **Table 4-11**. The intermetallic reaction **4-VIII** between manganese stannate and Sn is significant at a relatively low Sn content and a low Bi_2O_3 concentration. As the total metal fuel concentration was near the equimolar quantities, the manganese stannate was produced at a high Bi_2O_3 content. This is possibly evidence showing that these reactions maintained the exothermic reactions at adequate levels, supporting slow yet sustainable burning of these compositions.

Table 4-10： Compositions with MnO and the intermetallic compound Mn_3Sn as products

Reagents	**B1**	**B2**	**B3**	**B4**	**B5**	**B6**
Bi_2O_3	56.5	56.7	49.5	58.7	59.3	49.5
Mn	40.5	40.5	40.5	33.8	33.8	42.4
Sn	3.0	2.8	10.0	7.5	6.9	8.1
Products						
Bi	**29.1**	**41.9**	**37.6**	**38.9**	**33.3**	**31.9**
MnO	**53.2**	**44.9**	**41.3**	**47.6**	**47.6**	**46.7**
SnO_2	1.2				1.0	
Mn_3Sn	**11.5**	**13.3**	**19.3**	**12.6**	**12.0**	**18.5**
MnBi	**1.8**			0.9	2.3	1.7
Unreacted reagents						
Bi_2O_3	1.5				1.4	
Sn	1.3				1.1	
Mn	0.4		1.8		1.4	1.2

Table 4-11： Dominant reactions inferred from the quantitative XRD results

Scheme	**Reaction**	**Reagents, wt-%**		
		Bi_2O_3	**Mn**	**Sn**
4-III	$2Bi_2O_3 + 3Sn \rightarrow 4Bi + 3SnO_2$	72.35	-	26.75
4-IV	$Bi_2O_3 + 3Mn \rightarrow 2Bi + 3MnO$	73.87	26.13	-
4-V	$Bi_2O_3 + 5Mn \rightarrow 2MnBi + 3MnO$	62.91	37.09	-
4-VI	$7Bi_2O_3 + 6Sn \rightarrow 3Bi_2O_3 \cdot 6SnO_2 + 8Bi$	82.08	-	17.92
4-VII	$Bi_2O_3 + Mn + Sn \rightarrow 2Bi + MnO \cdot SnO_2$	72.85	8.59	18.56
4-VIII	$Bi_2O_3 + 6Mn + Sn \rightarrow 2Bi + 3MnO + Mn_3Sn$	50.96	36.05	12.98

5. CONCLUSIONS AND RECOMMENDATIONS

Al-NiO-Ni Ternary System

The binary thermite of an Al-NiO system which undergoes a standard oxidation-reduction reaction and was studied for potential use in a conventional pyrotechnic time-delay element. A maximum adiabatic reaction temperature was estimated from EKVI thermodynamic simulation, and the value was ca. 3100 K at an Al fuel content of 19.8 wt-%, which predicted the association with the following standard thermite reaction: $2Al + 3NiO \rightarrow Al_2O_3 + 3Ni$. Compared to the melting point of commercial tube materials (e.g. 933.5 K and 600.6 K for Al and Pb, respectively), this temperature is too high for an Al-NiO binary system compressed or compacted in a delay element. In addition, different products were predicted at varying Al concentrations. When taking into account of an intermetallic reaction which can generate NiAl or Ni_3Al products, the EKVI simulation for an Al-Ni binary system indicated a maximum adiabatic reaction temperature of ca. 2200 K at an Al content of 40.8 wt-%. Hence, it was possible to reduce the reaction temperature by up to 800 K through a combination of a standard thermite reaction, and an intermetallic reaction, i.e. NiAl and Ni_3Al were the main intermetallic products in Al-NiO-Ni ternary systems.

Burning rates were measured in borosilicate glass and lead tubes with compacted binary and ternary delay compositions. The overall combustion plots were shown in a parabola-like shape and the burning rates were insensitive to the inner diameter of the tubes for Al-NiO binary systems. Burning rates were determined in a range between 22 ± 1 $mm \cdot s^{-1}$ and 191 ± 31 $mm \cdot s^{-1}$ for Al-NiO compositions, including 20 – 55 wt-% fuel content, and they were slightly higher than the same formulations compacted in lead tubes. Meanwhile, for ternary systems in which the main intermetallic products were NiAl and Ni_3Al, the burning rates decreased linearly as the concentration of Al-Ni compositions increased. The maximum decrease of the burning rates was 146 $mm \cdot s^{-1}$ for formulations containing a 5Al/3NiO blend and an Al/Ni blend compacted in glass tubes. Similarly, the burning rates were slightly slower in lead tubes than compositions in glass tubes. The XRD results obtained after the burning tests confirmed the thermite reaction and thermite-intermetallic reaction of the products, e.g. Al_2O_3, NiAl and Ni_3Al, although the tested residues were collected after cooling down.

Sn-Bi_2O_3-Mn Ternary System

Two standard thermic binary systems based on bismuth oxide (Bi_2O_3) were investigated. The Sn-Bi_2O_3 binary system had a maximum adiabatic reaction temperature of ca. 1756 K at a fuel content of 26.75 wt-% Sn. XRD results confirmed the main products to be SnO_2 and Bi. The energy output showed a slight decrease as the fuel content increased. For the Mn-Bi_2O_3 binary system, visible plateaus of adiabatic reaction temperature were around 1836 K for fuel content in a range of 22 – 40 wt-%. XRD results confirmed that the main products were Bi, MnO and MnBi. The intermetallic product MnBi was detected for a composition with more than 40 wt-% Mn loading. The energy output decreased as the fuel content increased. Burning rates of 13 ± 1 $mm \cdot s^{-1}$ were obtained in a fuel range of 25 – 35 wt-% Sn. The burning rate decreased even further to 3.8 ± 0.7 $mm \cdot s^{-1}$ when the fuel loading was 55 wt-% Sn. The Mn-Bi_2O_3 system had successful ignition and stable combustion in the fuel range of 25 – 40 wt-% Mn. Combustion rates between 6.3 ± 1.8 $mm \cdot s^{-1}$ and 11.2 ± 0.8 $mm \cdot s^{-1}$ were observed. The combustion rates for both formulations were faster in the lead tubes compared to those in the glass tubes.

Ternary systems were formulated by adding reactive metals, i.e. Sn to the Mn-Bi_2O_3 system or Mn to the Sn-Bi_2O_3 system. This resulted in a change in the adiabatic reaction temperature profiles predicted using EKVI software. The formulation containing 3Sn/2Bi_2O_3 blended with Mn/Bi_2O_3 (mass ratio was 45:55) and resulted in an estimated adiabatic reaction temperature of ca. 1836 K. The slowest burning rate of the constructed ternary systems was 2.9 ± 0.6 $mm \cdot s^{-1}$ and the maximum value was less than 11 $mm \cdot s^{-1}$. XRD results confirmed that the reaction products were strongly dependent on the relative proportion of the binary blends. Both fuels were oxidised and manganese stannate formed instead of their own oxides under conditions with sufficient oxidisers. At very high Bi_2O_3 and low manganese contents, bismuth stannate was observed in XRD spectra. In addition, at high manganese-to-bismuth ratios, the intermetallic product Mn_3Sn was favoured.

Recommendations

The design of ternary systems investigated in this work was based on taking advantage of the intermetallic reactions that may occur in a fuel-rich thermite reaction state. The main hypothesis was that the adiabatic reaction temperature of a typical thermite reaction could be reduced, resulting in the desired burning rates while improving the ignitability of the

composition by inducing secondary intermetallic reactions. The results from the formulations investigated in this study showed that it is possible to replace traditional compositions with more environmentally benign materials while achieving the same delay performance. The present study focused on the effect of the ratios of reactants in the various formulations. However, other key factors that influence the burning rates such as the fuels selected, particle size and distribution, packing density, addition of binders and the use of inert additives should be considered. Additionally, it is recommended that appropriate kinetic models should be applied to these ternary systems to enable the prediction of burning rates and ignition temperatures.

REFERENCES

AHMAD, S. R. & RUSSELL, D. A. 2005. Laser ignition of pyrotechnics–effects of wavelength, composition and confinement. *Propellants, Explosives, Pyrotechnics: An International Journal Dealing with Scientific and Technological Aspects of Energetic Materials,* 30**,** 131-139.

AHMAD, S. R. & RUSSELL, D. A. 2008. Studies into laser ignition of confined pyrotechnics. *Propellants, Explosives, Pyrotechnics: An International Journal Dealing with Scientific and Technological Aspects of Energetic Materials,* 33**,** 396-402.

AI-KAZRAJI, S. S. & REES, G. J. 1979. The fast pyrotechnic reaction of silicon and red lead: heats of reaction and rates of burning. *Fuel,* 58**,** 139-143.

ALDUSHIN, A. & KHAIKIN, B. 1974. Combustion of mixtures forming condensed reaction products. *Combustion, Explosion and Shock Waves,* 10**,** 273-280.

ALENFELT, P. 2000. Chemical analysis of consumer fireworks. *Journal of Pyrotechnics***,** 11-15.

ANASTAS, P.T. & WARNER, J. C. 1998. Green chemistry: theory and practice. *Oxford [England], New York: Oxford University Press,* 11**,** 1394013941.

ARMSTRONG, R. 1990. Models for gasless combustion in layered materials and random media. *Combustion Science and Technology,* 71**,** 155-174.

BARKLEY, J. 1978. Pyrotechnica 1978. *IV,* 16**,** 18.

BECK, M., BROWN, M. & CAWTHORNE, D. 1984. Pyrotechnic delay composition. *ChemSA* June.

BECK, M. W. & BROWN, M. E. 1986a. Burning of antimony/potassium permanganate pyrotechnic compositions in closed systems. *Combustion and Flame,* 65**,** 263-271.

BECK, M. W. & BROWN, M. E. 1986b. Modification of the burning rate of antimony/potassium permanganate pyrotechnic delay compositions. *Combustion and Flame,* 66**,** 67-75.

BECK, M. W. & FLANAGAN, J. 1992. Delay composition and device. Google Patents.

BERGER, B. 2005. Parameters influencing the pyrotechnic reaction. *Propellants, Explosives, Pyrotechnics: An International Journal Dealing with Scientific and Technological Aspects of Energetic Materials,* 30**,** 27-35.

BOCHENEK, K. & BASISTA, M. 2015. Advances in processing of NiAl intermetallic alloys and composites for high temperature aerospace applications. *Progress in Aerospace Sciences,* 79**,** 136-146.

BOCKMON, B., PANTOYA, M., SON, S., ASAY, B. & MANG, J. 2005. Combustion velocities and propagation mechanisms of metastable interstitial composites. *Journal of Applied Physics,* 98**,** 064903.

BODDINGTON, T., COTTRELL, A. & LAYE, P. 1989. A numerical model of combustion in gasless pyrotechnic systems. *Combustion and Flame,* 76**,** 63-69.

BODDINGTON, T. & LA YE, P. 1987. Temperature dependence of the burning velocity of gasless pyrotechnics. *Thermochimica Acta,* 120**,** 203-206.

BODDINGTON, T., LAYE, P., TIPPING, J. & WHALLEY, D. 1986. Kinetic analysis of temperature profiles of pyrotechnic systems. *Combustion and Flame,* 63**,** 359-368.

BODDINGTON, T., LAYE, P. G., PUDE, J. & TIPPING, J. 1982. Temperature profile analysis of pyrotechnic systems. *Combustion and Flame,* 47**,** 235-254.

BOHLOULI-ZANJANI, G., WEN, J. Z., HU, A., PERSIC, J., RINGUETTE, S. & ZHOU, Y. N. 2013. Thermo-chemical characterization of an Al nanoparticle and NiO nanowire composite modified by Cu powder. *Thermochimica Acta,* 572**,** 51-58.

BRENT, G. F. & HARDING, M. D. 1993. Shock tube initiator. Google Patents.
BUCHANAN, B. J. 2005. Gunpowder: Alchemy, Bombards, and Pyrotechnics--The history of the explosive that changed the world. *Technology and Culture,* 46**,** 405-406.
CHARSLEY, E., CHEN, C.-H., BODDINGTON, T., LAYE, P. & PUDE, J. 1980. Differential thermal analysis and temperature profile analysis of pyrotechnic delay systems: ternary mixtures of silicon, boron and potassium dichromate. *Thermochimica Acta,* 35**,** 141-152.
CHEN, X., ZHAO, J., PAN, G. P. & LV, H. P. 2012. Experimental study of PTFE powder size impact to Mg/PTFE pyrotechnic composition. *Advanced Materials Research.*Trans Tech Publ, 281-285.
CONKLING, J. A. & MOCELLA, C. J. 2019. Chemistry of pyrotechnics: basic principles and theory. *Boca Raton, FL: CRC press*.
DANALI, S., PALAIAH, R. & RAHA, K. 2010. Developments in Pyrotechnics. *Defence Science Journal,* 60.
DAVITT, A. L. & YUILL, K. A. 1983. Delay composition for detonators. Google Patents.
DEAN, S., PANTOYA, M. L., GASH, A., STACY, S. & HOPE-WEEKS, L. 2010. Enhanced convective heat transfer in nongas generating nanoparticle thermites. *Journal of heat transfer,* 132.
DRENNAN, R. L. & BROWN, M. E. 1992. Binary and ternary pyrotechnic systems of Mn and/or Mo and BaO_2 and/or SrO_2: Part 2. Combustion studies. *Thermochimica Acta,* 208**,** 223-246.
DUBROVINSKAIA, N., DUBROVINSKY, L., CRICHTON, W., LANGENHORST, F., & RICHTER, A. 2005. Aggregated diamond nanorods, the densest and least compressible form of carbon. *Applied Physics Letters*, 87(8), 083106.
DUNMEAD, S. D., READEY, D. W., SEMLER, C. E. & HOL, J. B. 1989. Kinetics of combustion synthesis in the Ti-C and Ti-C-Ni systems. *Journal of the American Ceramic Society,* 72**,** 2318-2324.
EBRAHIMZADEH, S. J. & ZIARATI, M. 2020. Preparation and evaluation of pyrotechnic mixture containing Fe_2O3/Zr delay composition. *Journal of energetic msaterials,* 15, 47-52.
ELISCHER, P. P., CLEAL, G. & WILSON, M. 1986. The development of a boron and iron oxide delay system. *Materials Research Labs Ascot Vale (Australia)*.
ELLERN, H. 1961. Modern pyrotechnics; fundamentals of applied physical pyrochemistry [M]. Chemical publishing company.
ELLINGHAM, H. 1944. Transactions and communications. *J. Soc. Chem. Ind.,* 63**,** 125.
EPA, U. S. *Green Chemistry* [Online]. Available: https://www.epa.gov/greenchemistry [Accessed September 2022].
EPA, U. S. Environmental Protection Agency, Lead Air Pollution [online]. Available: https://www.epa.gov/lead-air-pollution/basic-information-about-lead-air-pollution#health [Accessed February 2023].
FATHOLLAHI, M. & AZIZI-TOUPKANLOO, H. 2019. Thermal characterization and kinetic analysis of nano-and micro-Al/NiO thermites: Combined experimental and molecular dynamics simulation study. *Journal of the Chinese Chemical Society,* 66**,** 909-918.
FATHOLLAHI, M. & BEHNEJAD, H. 2015. A comparative study of thermal behaviors and kinetics analysis of the pyrotechnic compositions containing Mg and Al. *Journal of Thermal Analysis and Calorimetry,* 120**,** 1483-1492.
FOCKE, W. W. 2007. Mixture model for correlating excess enthalpy data. *Journal of Chemical Engineering of Japan,* 40**,** 295-303.

FOCKE, W. W. & DU PLESSIS, B. 2004. Correlating multicomponent mixture properties with homogeneous rational functions. *Industrial & Engineering Chemistry Research,* 43**,** 8369-8377.

FOCKE, W. W., TICHAPONDWA, S. M., MONTGOMERY, Y. C., GROBLER, J. M. & KALOMBO, M. L. 2019. Review of gasless pyrotechnic time delays. *Propellants, Explosives, Pyrotechnics,* 44**,** 55-93.

FORDHAM, S. 2013. High explosives and propellants.*Oxford: Elsevier*.

GERLICH, M. & WOJEWóDKA, A. 2020. Study of gasless compositions used in time-delay elements. *Journal of Thermal Analysis and Calorimetry,* 139**,** 3473-3479.

GIBOT, P., COMET, M., VIDAL, L., MOITRIER, F., LACROIX, F., SUMA, Y., SCHNELL, F. & SPITZER, D. 2011. Synthesis of WO_3 nanoparticles for superthermites by the template method from silica spheres. *Solid State Sciences,* 13**,** 908-914.

GILLARD, P. 2007. Laser diode ignition of pyrotechnic mixtures: experimental and numerical studies. *Journal of Pyrotechnics,* 26**,** 53.

GRANIER, J. J. & PANTOYA, M. L. 2004. Laser ignition of nanocomposite thermites. *Combustion and Flame,* 138**,** 373-383.

GROBLER, J. M., COWGILL, A. W., FOCKE, W. W. & LABUSCHAGNE, G. 2018. Extrudable Gassy Pyrotechnic Time Delay Compositions. *Central European Journal of Energetic Materials,* 15.

HAN, B., GNANAPRAKASH, K., PARK, Y. & YOH, J. J. 2020. Understanding the effects of hygrothermal aging on thermo-chemical behaviour of Zr-Ni based pyrotechnic delay composition. *Fuel,* 281**,** 118776.

HAN, B. H., KIM, Y., JANG, S.-G., YOO, J. & YOH, J. J. 2019. Thermochemical characterization of Zr/Fe2O3 pyrotechnic mixture under natural aging conditions. *Journal of Applied Physics,* 126**,** 105113.

HAN, T. F. & YAN, S. L. 2014. Effects of the binders on the storage stability of the silicon delay composition. *Advanced Materials Research.. Trans Tech Publ,* 135-140.

HEDGER, J. 1983. Factors influencing the pyrotechnic reaction of silicon and red lead. *Propellants, Explosives, Pyrotechnics,* 8**,** 95-98.

HICKS, R., DE CALDAS, L., DARE, P. & HEWITT, P. 1986. Cardiotoxic and bronchoconstrictor effects of industrial metal fumes containing barium. *Archives of Toxicology,* Supplement, 9, 416-420.

HOPE, K. S., LLOYD, H. J., WARD, D., MICHALCHUK, A. A. & PULHAM, C. R. 2015. Resonant acoustic mixing: its applications to energetic materials. *Proceedings of New Trends in Research of Energetic Materials, Czech Republic***,** 134-143.

HOSSEINI S G, ESLAMI A. 2011. Investigation on the reaction of powdered tin as a metallic fuel with some pyrotechnic oxidizers[J]. *Propellants, Explosives, Pyrotechnics,* 36(2): 175-181.

HOWE, P. & WATTS, P. 2005. Concise international chemical assessment document 65: Tin and inorganic tin compounds. *World Health Organization,* 65.

HOWLETT, S. & MAY, F. G. J. 1973. Ignition and Reaction of Boron Fueled Pyrotechnic Delay Compositions. Part 1. Boron-potassium dichromate and boron-silicon-potassium dichromate systems. *Defence Standards Labs Maribyrnong (Australia).*

HUANG, S., DENG, S., JIANG, Y. & ZHENG, X. 2019. Experimental effective metal oxides to enhance boron combustion. *Combustion and Flame,* 205**,** 278-285.

ILUNGA, K., DEL FABBRO, O., YAPI, L. & FOCKE, W. W. 2011. The effect of Si–Bi2O3 on the ignition of the Al–CuO thermite. *Powder Technology,* 205**,** 97-102.

JAKUBKO, J. 1997. Pressure and temperature effects on burning rate of the silicon-red lead system. *Journal of Energetic Materials,* 15**,** 151-161.

JAKUBKO, J. 1999. Combustion of the silicon-red lead system. Temperature of burning, kinetic analysis and mathematical model. *Combustion Science and Technology,* 146**,** 37-55.

JAKUBKO, J. & ČERNOŠKOVá, E. 1997. Differential thermal analysis of the mixtures of silicon and red lead. *Journal of Thermal Analysis and Calorimetry,* 50**,** 511-515.

JOHNSON, D. M. 1965. Ignition Theory: Application to the Design of New Ignition Systems. *NAVAL AMMUNITION DEPOT CRANE IN.*

KALOMBO, L. 2008. *Evaluation of Bi2O3 and Sb6O13 as oxidants for silicon fuel in time delay detonators.* University of Pretoria.

KALOMBO, L., DEL FABBRO, O., CONRADIE, C. & FOCKE, W. W. 2007. Sb6O13 and Bi2O3 as oxidants for Si in pyrotechnic time delay compositions. *Propellants, Explosives, Pyrotechnics: An International Journal Dealing with Scientific and Technological Aspects of Energetic Materials,* 32**,** 454-460.

KAPPAGANTULA, K. S., CLARK, B. & PANTOYA, M. L. 2011. Flame propagation experiments of non-gas-generating nanocomposite reactive materials. *Energy & fuels,* 25**,** 640-646.

KELLY, C. J. N., MORROW, W. C. & ZAPPALORTI, A. 1975. Fuse and its method of manufacture. Google Patents.

KHAIKIN, B. & MERZHANOV, A. 1966. Theory of thermal propagation of a chemical reaction front. *Combustion, Explosion and Shock Waves,* 2**,** 22-27.

KLAPÖTKE, T. M. 2019. Chemistry of High-Energy Materials Sixth Edition. *Munich: Germany: de Gruyter.*

KOENIG, J. T., SHAW, A. P., PORET, J. C., ECK, W. S. & GROVEN, L. J. 2017. Performance of W/MnO_2 as an environmentally friendly energetic time delay composition. *ACS Sustainable Chemistry & Engineering,* 5**,** 9477-9484.

KOGA, N. & CRIADO, J. M. 1998. Kinetic analyses of solid-state reactions with a particle-size distribution. *Journal of the American Ceramic Society,* 81**,** 2901-2909.

KOSANKE, K. 2004. Pyrotechnic Chemistry. *Whitewater, CO: Journal of Pyrotechnics Inc*.

KOSANKE, K., KOSANKE, B., STURMAN, B., SHIMIZU, T., WILSON, M., VON MALTITZ, I., HANCOX, R., KUBOTA, N., JENNINGS-WHITE, C. & CHAPMAN, D. 2004. Pyrotechnic chemistry, pyrotechnic reference series, No. 4. *Journal of Pyrotechnics, Inc.,* Whitewater, CO.

KRONE, U. & LANCASTER, R. 2000. Pyrotechnics. *Ullmann's Encyclopedia of Industrial Chemistry*. New York: Wiley.

KUMAR, R. V., CHIVALL, J., BROOK, D., BARBER, B. & SALLOWS, L. . 2008. *Ellingham Diagram* [Online]. Available: https://www.doitpoms.ac.uk/tlplib/ellingham_diagrams/ellingham.php [Accessed September 2022].

KWON, Y.-S., GROMOV, A. A. & STROKOVA, J. I. 2007. Passivation of the surface of aluminum nanopowders by protective coatings of the different chemical origin. *Applied Surface Science,* 253**,** 5558-5564.

LAYE, P. 1997. Tying up loose ends. *Thermochimica Acta,* 300**,** 237-245.

LAYE, P. & CHARSLEY, E. 1987. Thermal analysis of pyrotechnics. *Thermochimica Acta,* 120**,** 325-349.

LEE, B.-J., OH, C.-S. & SHIM, J.-H. 1996. Thermodynamic assessments of the Sn-In and Sn-Bi binary systems. *Journal of electronic materials,* 25**,** 983-991.

LI, J.-S., LIN, C.-H., HWANG, C.-C., LU, K.-T. & YEH, T.-F. 2018. Investigation of the burning properties of low-toxicity B/CuO delay compositions. *Combustion Science and Technology*.

LI, J., GUAN, H., SONG, D., WANG, Q. & DU, J. 2015. Effects of gas production on acoustic radiation characteristics of underwater pyrotechnic combustion. *Journal of Low Frequency Noise, Vibration and Active Control,* 34**,** 1-8.

LI, Y., CHENG, Y., HUI, Y.-L. & YAN, S. 2010. The effect of ambient temperature and boron content on the burning rate of the B/Pb_3O_4 delay compositions. *Journal of Energetic Materials,* 28**,** 77-84.

MA, X., LI, Y., HUSSAIN, I., SHEN, R., YANG, G. & ZHANG, K. 2020. Core–shell structured nanoenergetic materials: preparation and fundamental properties. *Advanced Materials,* 32**,** 2001291.

MCLAIN, J. H. 1980. Pyrotechnics: From the Viewpoint of Solid State Chemistry. *Philadelphia: Franklin Institute Press.*

MEI, Z. & MORRIS, J. 1992. Characterization of eutectic Sn-Bi solder joints. *Journal of Electronic Materials,* 21**,** 599-607.

MERZHANOV, A. 1994. Solid flames: discoveries, concepts, and horizons of cognition. *Combustion Science and Technology,* 98**,** 307-336.

MERZHANOV, A. & ABRAMOV, V. 1981. Thermal explosion of explosives and propellants. A review. *Propellants, Explosives, Pyrotechnics,* 6**,** 130-148.

MIKLASZEWSKI, E. J. 2014a. Microchannel combustion dynamics of low gas, environmentally friendly time delay compositions. *Purdue University.*

MIKLASZEWSKI, E. J., SHAW, A. P., PORET, J. C., SON, S. F. & GROVEN, L. J. 2014a. Performance and aging of Mn/MnO_2 as an environmentally friendly energetic time delay composition. *ACS Sustainable Chemistry & Engineering,* 2**,** 1312-1317.

MIKLASZEWSKI, E. J., PORET, J. C., SHAW, A. P., SON, S. F., & GROVEN, L. J. 2014b. Ti/C ‐ 3Ni/Al as a replacement time delay composition. *Propellants, Explosives, Pyrotechnics,* 39(1), 138-147.

MOGHADDAM, A. Z. & REES, G. J. 1981. The fast pyrotechnic reaction of silicon with lead oxides: Differential scanning calorimetry and hot-stage microscopy studies. *Fuel,* 60**,** 629-632.

MONOGAROV, K., MEEROV, D., FROLOV, Y. V. & PIVKINA, A. 2019. Combustion features of nanothermites in pyrotechnic heaters. *Russian Journal of Physical Chemistry B,* 13**,** 610-614.

MONTGOMERY, Y. C. 2018. Measuring and modelling of pyrotechnic time delay element burn rates. *University of Pretoria.*

Montgomery, Y. C., Focke, W. W., Atanasova, M., Del Fabbro, O., & Kelly, C. (2016). Mn+ Sb_2O_3 thermite/intermetallic delay compositions. *Propellants, Explosives, Pyrotechnics,* 41(5), 919-925.

MONTGOMERY, Y. C., FOCKE, W. W. & KELLY, C. 2017a. Measurement and modelling of pyrotechnic time delay burning rates: application and prediction of a fast burning delay composition. *Propellants, Explosives, Pyrotechnics,* 42**,** 1289-1295.

MONTGOMERY, Y. C., FOCKE, W. W. & KELLY, C. 2017b. Measurement and modelling of pyrotechnic time delay burning rates: Method and model development. *Propellants, Explosives, Pyrotechnics,* 42**,** 1161-1167.

MORGAN, C. G. & RIMMINGTON, C. 2012. Manufacture of pyrotechnic time delay compositions. Google Patents.

MORSI, K. 2001. Review: reaction synthesis processing of Ni-Al intermetallic materials.. *Materials Science & Engineering,* 299(9), 01407-6.

MUI, S., TAM, S., SHING, G., CHEUNG, K. & WAN, R. 2015. The use of electronic detonators in vibration control for blasting. Hong Kong: Drainage Services Department, The Government of the Hong Kong .

MUNIR, Z. A. & ANSELMI-TAMBURINI, U. 1989. Self-propagating exothermic reactions: the synthesis of high-temperature materials by combustion. *Materials Science Reports,* 3**,** 277-365.

NACU, S. 2011. Practical aspects on using polytetrafluorethylene (PTFE) in pyrotechnic compositions. *Rev. Chim.(Bucharest),* 62**,** 113.

NAUD, D. L., HISKEY, M. A., SON, S. F., BUSSE, J. R. & KOSANKE, K. 2003. Feasibility study on the use of nanoscale thermites for lead-free electric matches. *Journal of Pyrotechnics***,** 65-78.

NELLUMS, R. R., TERRY, B. C., TAPPAN, B. C., SON, S. F. & GROVEN, L. J. 2013. Effect of solids loading on resonant mixed Al-Bi_2O_3 nanothermite powders. *Propellants, Explosives, Pyrotechnics,* 38**,** 605-610.

OKAMOTO, H. 1999. Mn-Sn (manganese-tin). *Journal of Phase Equilibria and Diffusion,* 20**,** 542.

OSORIO, J. G. & MUZZIO, F. J. 2015. Evaluation of resonant acoustic mixing performance. *Powder Technology,* 278**,** 46-56.

OUYANG, D.-H. 2013. Effect of different binders on the combustion characteristics of Ba (NO_3) 2/Mg-containing pyrotechnic mixtures. *Central European Journal of Energetic Materials,* 10.

PEREZ-MAQUEDA, L., CRIADO, J. & SANCHEZ-JIMENEZ, P. 2006. Combined kinetic analysis of solid-state reactions: a powerful tool for the simultaneous determination of kinetic parameters and the kinetic model without previous assumptions on the reaction mechanism. *Journal of Physical Chemistry A,* 110**,** 12456-12462.

PICHOT, V., COMET, M., MIESCH, J. & SPITZER, D. 2015. Nanodiamond for tuning the properties of energetic composites. *Journal of Hazardous Materials,* 300**,** 194-201.

PICKARD, J. M. 2002. Critical ignition temperature. *Thermochimica Acta,* 392**,** 37-40.

PORET, J. C., SHAW, A. P., CSERNICA, C. M., OYLER, K. D. & ESTES, D. P. 2013. Development and performance of the W/Sb2O3/KIO4/lubricant pyrotechnic delay in the US Army hand‐held signal. *Propellants, Explosives, Pyrotechnics,* 38**,** 35-40.

PORET, J. C., SHAW, A. P., GROVEN, L. J., CHEN, G. & OYLER, K. D. 2012. Environmentally benign pyrotechnic delays. *Army Armament Research Development And Engineering Center Picatinny Arsenal.*

PORET, J. C., SHAW, A. P., MIKLASZEWSKI, E. J., GROVEN, L. J., CSERNICA, C. M. & CHEN, G. 2014. Environmentally benign energetic time delay compositions: Alternatives for the US Army hand-held signal. *Army Armament Research Development And Engineering Center Picatinny Arsenal*.

PORTER, R. F., SCHISSEL, P. & INGHRAM, M. G. 1955. A mass spectrometric study of gaseous species in the Al–Al_2O_3 system. *Journal of Chemical Physics,* 23**,** 339-342.

POTGIETER, G., FOCKE, W. W., DEL FABBRO, O., LABUSCHAGNÉ, G. D. & KELLY, C. 2016. Fluoroelastomer pyrotechnic time delay compositions. *Journal of Thermal Analysis and Calorimetry,* 126**,** 1363-1370.

POURMORTAZAVI, S., HAJIMIRSADEGHI, S., KOHSARI, I., FATHOLLAHI, M. & HOSSEINI, S. 2008. Thermal decomposition of pyrotechnic mixtures containing either aluminum or magnesium powder as fuel. *Fuel,* 87**,** 244-251.

REN, H., JIAO, Q. & CHEN, S. 2010. Mixing Si and carbon nanotubes by a method of ball-milling and its application to pyrotechnic delay composition. *Journal of Physics and Chemistry of Solids,* 71**,** 145-148.

RICCO, I., FOCKE, W. & CONRADIE, C. 2004. Alternative oxidants for silicon fuel in time-delay compositions. *Combustion Science and Technology,* 176**,** 1565-1575.
ROBERTSON, I. & WAYMAN, C. 1984. Ni_5Al_3 and the nickel-aluminum binary phase diagram. *Metallography,* 17**,** 43-55.
ROSSI, C., ZHANG, K., ESTEVE, D., ALPHONSE, P., TAILHADES, P. & VAHLAS, C. 2007. Nanoenergetic materials for MEMS: a review. *Journal of Microelectromechanical Systems,* 16**,** 919-931.
ROSSOL, M. 2001. Brief survey of chromium toxicity. *Journal of Pyrotechnics***,** 61-62.
RUGUNANAN, R. A. & BROWN, M. E. 1991. Reactions of powdered silicon with some pyrotechnic oxidants. *Journal of Thermal Analysis and Calorimetry,* 37**,** 1193-1211.
SABATINI, J. J. 2014. Advances toward the development of "Green" pyrotechnics. *Green Energetic Materials***,** 63-102.
SANDERS, V. E., ASAY, B. W., FOLEY, T. J., TAPPAN, B. C., PACHECO, A. N. & SON, S. F. 2007. Reaction propagation of four nanoscale energetic composites (Al/MoO_3, Al/WO_3, Al/CuO, and Bi_2O_3). *Journal of Propulsion and Power,* 23**,** 707-714.
SARAWADEKAR, R. & AGRAWAL, J. 2008. Nanomaterials in Pyrotechnics. *Defence Science Journal,* 58.
SHAW, A. P., PORET, J. C., GILBERT JR, R. A., DOMANICO, J. A. & BLACK, E. L. 2013. Development and performance of boron carbide-based smoke compositions. *Propellants, Explosives, Pyrotechnics,* 38**,** 622-628.
SHAW, A.P.G. 2020. *Thermitic Thermodynamics*, 674, 834, 937, 1055, CRC Press.
SHAW, A. P., PORET, J. C., GILBERT, R. A., MORETTI, J. D., SABATINI, J. J., OYLER, K. D. & CHEN, G. 2012. Pyrotechnic smoke compositions containing boron carbide. *Picatinny Arsenal Dover Nj Pyrotechnics Lab.*
SHAW, A. P., PORET, J. C., GRAU JR, H. A. & GILBERT JR, R. A. 2015a. Demonstration of the $B_4C/NaIO_4$/PTFE delay in the US army hand-held signal. *ACS Sustainable Chemistry & Engineering,* 3**,** 1558-1563.
SHAW, A. P., SADANGI, R. K., PORET, J. C. & CSERNICA, C. M. 2015b. Metal-element compounds of titanium, zirconium, and hafnium as pyrotechnic fuels. *Army Armament Research Development and Engineering Center Picatinny Arsenal NJ*.
SIJIMOL, M. & MOHAN, M. 2014. Environmental impacts of perchlorate with special reference to fireworks—a review. *Environmental Monitoring and Assessment,* 186**,** 7203-7210.
ŠIMON, P. 2005. Considerations on the single-step kinetics approximation. *Journal of Thermal Analysis and Calorimetry,* 82**,** 651-657.
SON, S., HISKEY, M., NAUD, D., BUSSE, J. & ASAY, B. 2002. Lead-free electric matches. *Los Alamos National Lab. (LANL), Los Alamos, NM (United States).*
STEINHAUSER, G. & KLAPÖTKE, T. M. 2008. "Green" pyrotechnics: a chemists' challenge. *Angewandte Chemie International Edition,* 47**,** 3330-3347.
SUKUMAR, A. & SUBRAMANIAN, R. 1992. Trace elements in scalp hair of manufacturers of fireworks from Sivakasi, Tamil Nadu. *Science of the Total Environment,* 114**,** 161-168.
SWANEPOEL, D., DEL FABBRO, O., FOCKE, W. W. & CONRADIE, C. 2010. Manganese as fuel in slow-burning pyrotechnic time delay compositions. *Propellants, Explosives, Pyrotechnics,* 35**,** 105-113.
TCHOUNWOU, P. B., YEDJOU, C. G., PATLOLLA, A. K. & SUTTON, D. J. 2012. Heavy metal toxicity and the environment. *Molecular, clinical and environmental toxicology***,** 133-164.
THURESON, G. R. & GLADDEN, E. L. 1988. *Nonelectric blasting initiation signal control system, method and transmission device therefore*. European Patent No.: 0250582B1.

TICHAPONDWA, S., FOCKE, W., FABBRO, O. D., SANDENBERGH, R. & MULLER, E. 2014. Suppressing hydrogen evolution by aqueous silicon powder dispersions through the introduction of an additional cathodic reaction. *Chemical Engineering Communications,* 201**,** 501-515.

TICHAPONDWA, S. M., FOCKE, W. W., DEL FABBRO, O. & KELLY, C. 2015. Calcium sulfate as a possible oxidant in "green" silicon-based pyrotechnic time delay compositions. *Propellants, Explosives, Pyrotechnics,* 40**,** 518-525.

TICHAPONDWA, S. M., FOCKE, W. W., DEL FABBRO, O. & LABUSCHAGNE, G. 2016. The Effect of Additives on the Burning Rate of Silicon-Calcium Sulfate Pyrotechnic Delay Compositions. *Propellants, Explosives, Pyrotechnics,* 41**,** 732-739.

TICHAPONDWA, S. M., GUO, S. & ROUX, W. E. 2021. Performance of Mn/Bi_2O_3 pyrotechnic time delay compositions.

TREUMANN, H. Ein Ordnungs-und Dokumentationssystem für die Pyrotechnik. *Pyrotechnik,* 1975. 407-422.

TRIBELHORN, M. J. 1994. Reactions of iron-and zinc-fuelled pyrotechnic systems. *Rhodes University.*

TRIBELHORN, M. J., BLENKINSOP, M. G. & BROWN, M. E. 1995a. Combustion of some iron-fuelled binary pyrotechnic systems. *Thermochimica Acta,* 256**,** 291-307.

TRIBELHORN, M. J., VENABLES, D. S. & BROWN, M. E. 1995b. Combustion of some zinc-fuelled binary pyrotechnic systems. *Thermochimica Acta,* 256**,** 309-324.

TSANG, K.-L. 2005. The initiation process inside a detonation delay element. *International Journal of Applied Mathematics and Mechanics,* 1**,** 12-39.

TULIS, A. J. 1980. Flowability techniques in the processing of powdered explosives, propellants, and pyrotechnics. *Journal of Hazardous Materials,* 4**,** 3-10.

VAZ, N. G., & PANTOYA, M. L. 2022. Silicon alloying enhances fast heating rate combustion of aluminum particles. Combustion and Flame, 241, 112156.

UMBRAJKAR, S. M., SCHOENITZ, M. & DREIZIN, E. L. 2006. Control of structural refinement and composition in $Al\text{-}MoO_3$ nanocomposites prepared by arrested reactive milling. *Propellants, Explosives, Pyrotechnics: An International Journal Dealing with Scientific and Technological Aspects of Energetic Materials,* 31**,** 382-389.

URBANSKY, E. T. 2000. Perchlorate in the Environment. *New York: Kluwer Academic.*

VERMA, H. K. & THOTE, N. 2013. Investigation of delay time precision in pyrotechnic detonators. *J. Rock Mech. Tunn. Technol,* 19**,** 19-28.

WALTERS, I. T. & GROVEN, L. J. 2019. Environmentally friendly boron-based pyrotechnic delays: an additive manufacturing approach. *ACS Sustainable Chemistry & Engineering,* 7**,** 4360-4367.

WANG, J., HU, A., PERSIC, J., WEN, J. Z. & ZHOU, Y. N. 2011. Thermal stability and reaction properties of passivated Al/CuO nano-thermite. *Journal of Physics and Chemistry of Solids,* 72**,** 620-625.

XUE, X.-C., MA, L.-Z. & YU, Y.-G. 2020. Effects of Mg/PTFE pyrotechnic compositions on reignition characteristics of base bleed propellants and heating mechanism. *Defence Technology,* 18(1).

ZHANG, Y. & STANGLE, G. C. 1993. Ignition criteria for self-propagating combustion synthesis. *Journal of Materials Research,* 8**,** 1703-1711.

ZHAO, W., JIAO, Q., CHEN, P., YAN, S., ZHU, Y., ZHANG, B., ZENG, X., LIU, D., OU, Y. & WANG, F. 2022. Synergetic energetic kinetics of Mg-Zn alloys and pyrotechnics. *Combustion and Flame,* 240**,** 112000.

ZHU, P., SHEN, R., FIADOSENKA, N., YE, Y. & HU, Y. 2011. Dielectric structure pyrotechnic initiator realized by integrating Ti/CuO-based reactive multilayer films. *Journal of Applied Physics,* 109**,** 084523.

PUBLICATIONS

Journal Articles

Tichapondwa S. M*., **Guo S.**, Roux W. E. Performance of the Mn/Bi_2O_3 Pyrotechnic Time Delay Composition [J]. *Central European Journal of Energetic Materials*, 2021, 18(EPA): 46-62. DOI: 10.22211/cejem/134798.

Guo, S., Focke W. W.*, Tichapondwa S. M. Sn/Mn/Bi_2O_3 Ternary Pyrotechnic Time Delay Compositions [J]. *ACS Sustainable Chemistry & Engineering*, 2020, 8(38): 14524 – 14530. DOI: 10.1021/acssuschemeng.0c04958.

Guo, S., Focke W. W.*, Tichapondwa S.M. Al-Ni-NiO Pyrotechnic Time-Delays [J]. *Propellants, Explosives, Pyrotechnics*, 2020, 45(4): 665-670. DOI: 10.1002/prep.201900304.

Conference Papers Presented

Guo, S., Focke W.W.*, Tichapondwa S. M. Pyrotechnic time-delays: Al-Ni-NiO system. *Proceedings of the 23rd seminar on New trends in Research of Energetic Materials*, Pardubice, Czech Republic, 1-3rd April 2020.

APPENDICES

Appendix A: XRD analysis for the combustion residues of Al-NiO-Ni system

Table S 1: Details of reagents in the glass tubes before combustion

Sample Code	Component (amounts in wt-%)
SG021	20Al/80NiO
SG025	25Al/75NiO
SG026	35Al/65NiO
SG024	50Al/50NiO
SG037	35Al/35NiO/30Ni
SG039	35.5Al/41.5NiO/23Ni
SG041	36Al/47.5NiO/16.5Ni
SG043	37Al/53NiO/10Ni
SG045	37Al/56.5NiO/6.5Ni
SG047	23Al/55.5NiO/21.5Ni
SG049	24.5Al/62.5NiO/13Ni
SG051	26Al/70NiO/4Ni

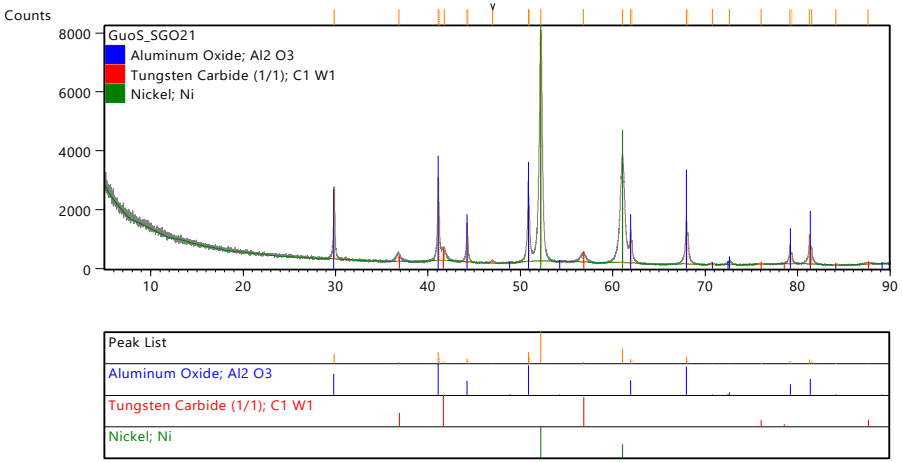
Counts
GuoS_SGO21
Aluminum Oxide; Al2 O3
Tungsten Carbide (1/1); C1 W1
Nickel; Ni
Peak List
Aluminum Oxide; Al2 O3
Tungsten Carbide (1/1); C1 W1
Nickel; Ni

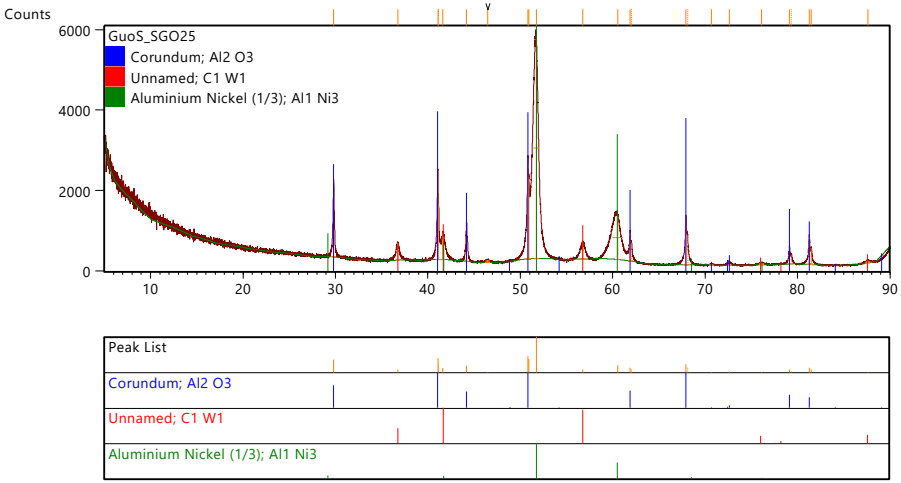
Counts
GuoS_SGO25
Corundum; Al2 O3
Unnamed; C1 W1
Aluminium Nickel (1/3); Al1 Ni3
Peak List
Corundum; Al2 O3
Unnamed; C1 W1
Aluminium Nickel (1/3); Al1 Ni3

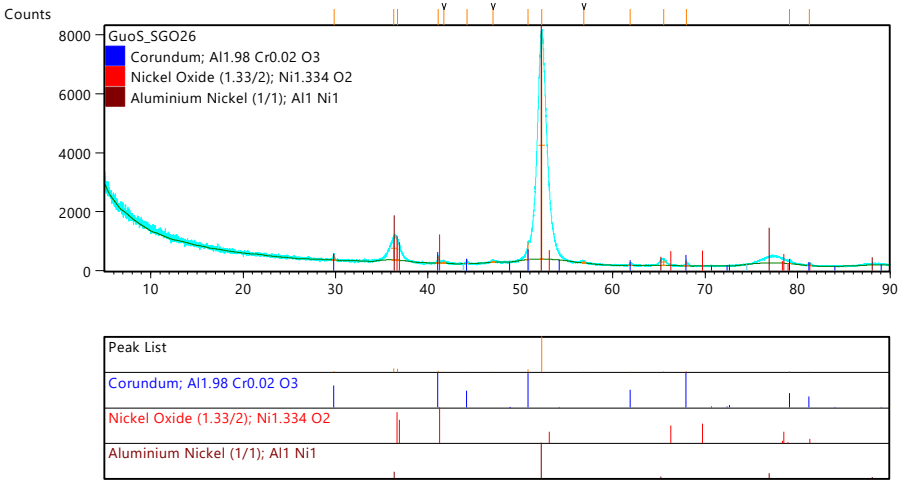
Counts
GuoS_SGO26
Corundum; Al1.98 Cr0.02 O3
Nickel Oxide (1.33/2); Ni1.334 O2
Aluminium Nickel (1/1); Al1 Ni1
Peak List
Corundum; Al1.98 Cr0.02 O3
Nickel Oxide (1.33/2); Ni1.334 O2
Aluminium Nickel (1/1); Al1 Ni1

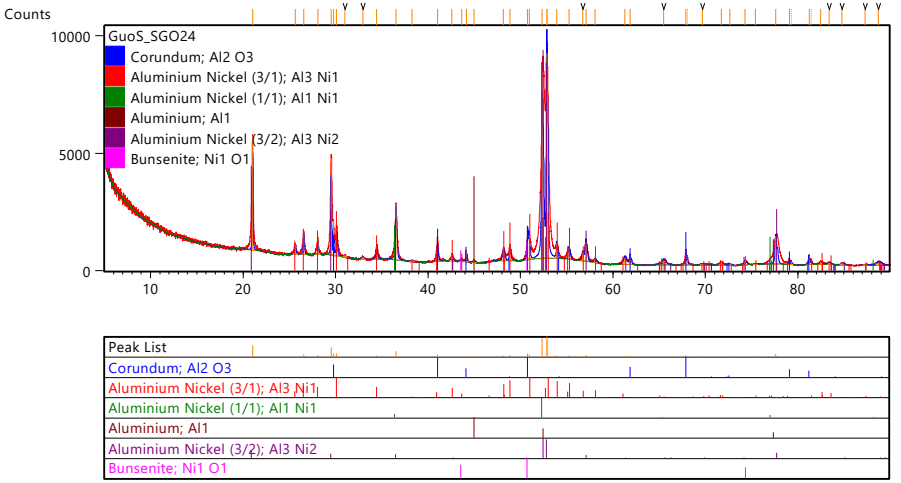
Counts
GuoS_SGO24
Corundum; Al2 O3
Aluminium Nickel (3/1); Al3 Ni1
Aluminium Nickel (1/1); Al1 Ni1
Aluminium; Al1
Aluminium Nickel (3/2); Al3 Ni2
Bunsenite; Ni1 O1
Peak List
Corundum; Al2 O3
Aluminium Nickel (3/1); Al3 Ni1
Aluminium Nickel (1/1); Al1 Ni1
Aluminium; Al1
Aluminium Nickel (3/2); Al3 Ni2
Bunsenite; Ni1 O1

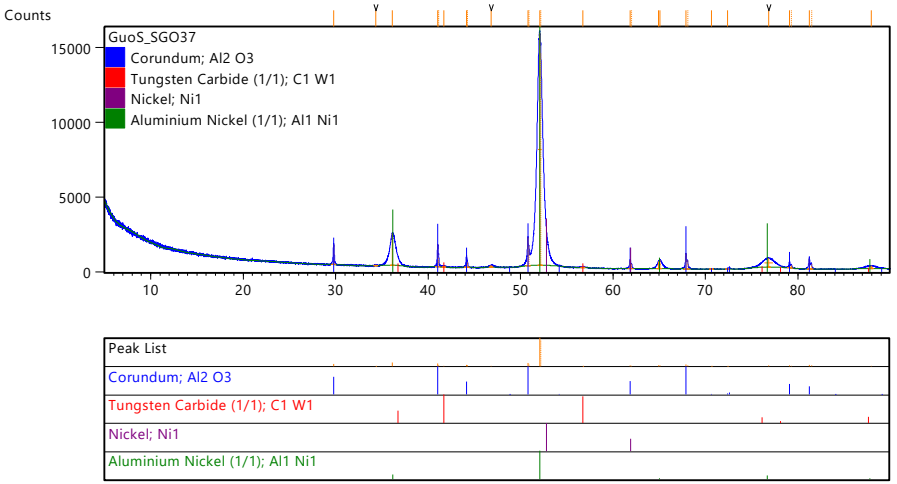
Counts
GuoS_SGO37
Corundum; Al2 O3
Tungsten Carbide (1/1); C1 W1
Nickel; Ni1
Aluminium Nickel (1/1); Al1 Ni1
15000
10000
5000
0
10
20
30
40
50
60
70
80
Peak List
Corundum; Al2 O3
Tungsten Carbide (1/1); C1 W1
Nickel; Ni1
Aluminium Nickel (1/1); Al1 Ni1

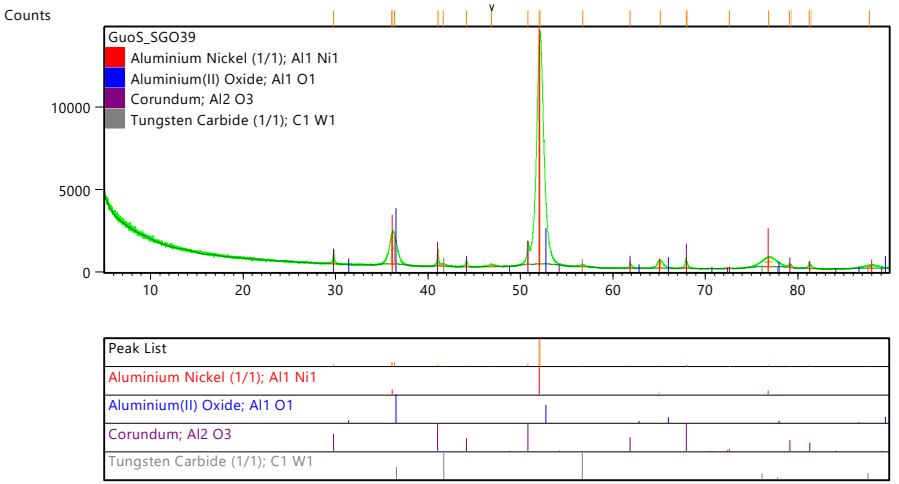
Counts
GuoS_SGO39
Aluminium Nickel (1/1); Al1 Ni1
Aluminium(II) Oxide; Al1 O1
Corundum; Al2 O3
Tungsten Carbide (1/1); C1 W1
10000
5000
0
10
20
30
40
50
60
70
80
Peak List
Aluminium Nickel (1/1); Al1 Ni1
Aluminium(II) Oxide; Al1 O1
Corundum; Al2 O3
Tungsten Carbide (1/1); C1 W1

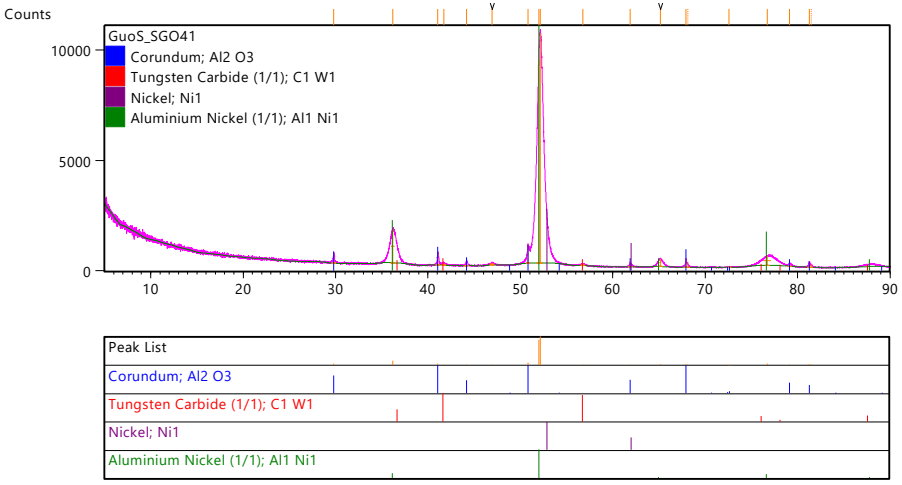
Counts
GuoS_SGO41
Corundum; Al2 O3
Tungsten Carbide (1/1); C1 W1
Nickel; Ni1
Aluminium Nickel (1/1); Al1 Ni1
10000
5000
0
10
20
30
40
50
60
70
80
90
Peak List
Corundum; Al2 O3
Tungsten Carbide (1/1); C1 W1
Nickel; Ni1
Aluminium Nickel (1/1); Al1 Ni1

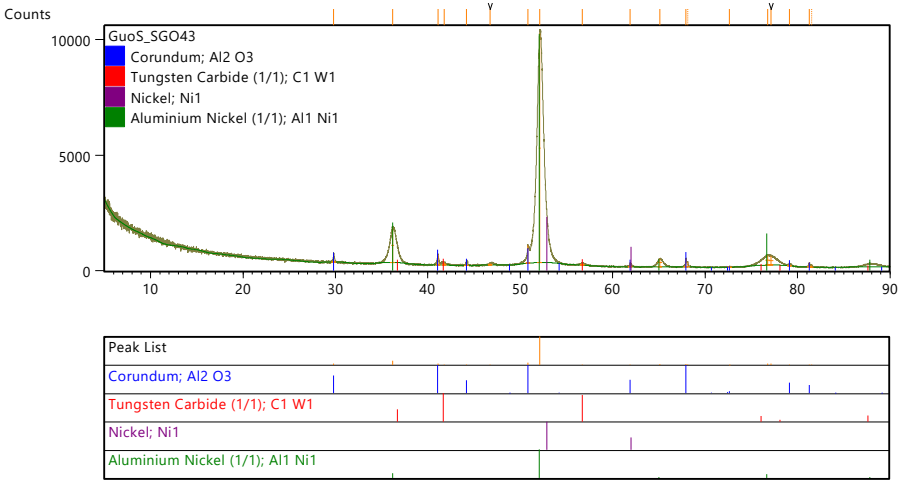
Counts
GuoS_SGO43
Corundum; Al2 O3
Tungsten Carbide (1/1); C1 W1
Nickel; Ni1
Aluminium Nickel (1/1); Al1 Ni1
10000
5000
0
10
20
30
40
50
60
70
80
90
Peak List
Corundum; Al2 O3
Tungsten Carbide (1/1); C1 W1
Nickel; Ni1
Aluminium Nickel (1/1); Al1 Ni1

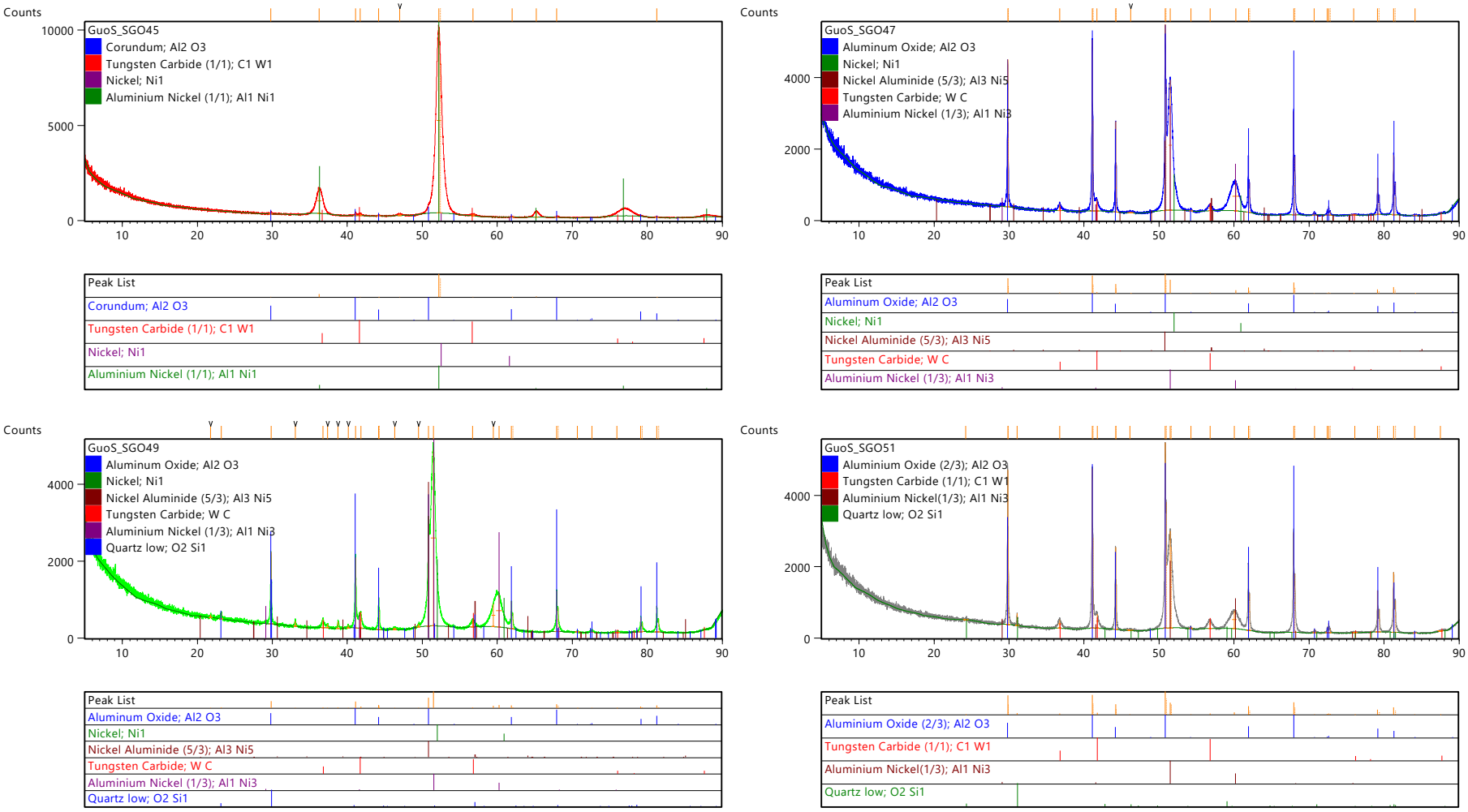

Figure S 1: XRD diffractograms of residues obtained after combustion in the glass tubes

Table S 2: XRF analysis results for the aluminium, nickel oxide and nickel powders used

Al	Mg	Fe	Si	Na	Ca	Ni	Mn	Sn
99.47	0.17	0.08	0.11	0.01	0.01	0.01	<0.01	<0.01
Co	Cu	Sm	Tb	Hf	Mo	Bi	Pb	**Total**
<0.01	<0.01	<0.01	<0.01	<0.01	<0.01	0.00	0.00	**99.86**
Ni	Na	Mg	Al	Si	Ca	Hf	Bi	Mo
99.62	0.16	0.06	0.05	0.01	0.01	0.02	0.01	0.01
Mn	Fe	Co	Cu	Sm	Tb	Pb	Sn	**Total**
<0.01	<0.01	<0.01	<0.01	<0.01	<0.01	<0.01	<0.01	**99.94**
NiO	MgO	Na_2O	SiO_2	CaO	Al_2O_3			**Total**
99.65	0.28	0.27	0.11	0.08	0.06			**100.5**

Appendix B: XRD analysis for the combustion residues of Sn-Bi_2O_3-Mn system

The burn residue slags were milled into fine powders using a B tungsten carbide mill before XRD scanning. The recorded samples are listed in **Table S3** and the estimated phase amounts in **Table S4**. The XRD spectra are shown in **Figure S2**.

Table S 3: Details of reagents in the glass tubes before combustion

Code in Paper	Sample Code	Component (Amounts in wt-%)
B3	Sample 1	27.7Sn/72.4Bi_2O_3
B4	Sample 2	30.0Sn/70.0 Bi_2O_3
B5	Sample 3	40.0Sn/60.0 Bi_2O_3
B6	Sample 4	50.0Sn/50.0 Bi_2O_3
B9	Sample 5	22.5Sn/11.3Mn/66.2Bi_2O_3
B1	Sample 6	15.0Sn/22.5Mn/62.5Bi_2O_3
B4	Sample 7	7.5Sn/33.8Mn/58.7Bi_2O_3
B11	Sample 8	31.2Sn/5.8Mn/63.0Bi_2O_3
B3	Sample 9	10.0Sn/40.5Mn/49.5Bi_2O_3
B6	Sample 10	8.1Sn/42.4Mn/49.5Bi_2O_3
B10	Sample 11	27.0Sn/10.0Mn/63.0Bi_2O_3
B8	Sample 12	20.7Sn/11.3Mn/68.0Bi_2O_3
B2	Sample 13	13.8Sn/22.5Mn/63.7Bi_2O_3
B5	Sample 14	6.9Sn/33.8Mn/59.3Bi_2O_3
B7	Sample 15	27.0Sn/4.5Mn/68.5Bi_2O_3
B1	Sample 16	3.0Sn/40.5Mn/56.5Bi_2O_3
B2	Sample 17	2.8Sn/40.5Mn/56.7Bi_2O_3
	Sample 18	17.0Sn/27.0Mn/56.0Bi_2O_3
	Sample 19	23.0Sn/23.0Mn/54.0Bi_2O_3
	Sample 20	27.0Sn/17.0Mn/56.0Bi_2O_3
	Sample 21	15.0Sn/35.0Mn/50.0Bi_2O_3
	Sample 22	20.0Sn/30.0Mn/50.0Bi_2O_3
	Sample 23	30.0Sn/20.0Mn/50.0Bi_2O_3
	Shepherd-40% Res	40Mn/60Bi_2O_3
	Mn-Bi_2O_3-Residue	45Mn/55Bi_2O_3
	Shepherd-50% Res	40Mn/60Bi_2O_3

Table S 4: Quantitative XRD analysis of the residues obtained after combustion in the glass tubes

Sample	1	2	3	4	5	6	7	8	9	10	11	12	13	14	15	16	17	18	19	20	21	22	23
Bi_2O_3	72.4	70.0	60.0	50.0	66.2	62.5	58.7	63.0	49.5	49.5	63.0	68.0	63.7	59.3	56.5	56.5	56.7	56.0	54.0	56.0	50.0	50.0	50.
Mn					11.3	22.5	33.8	5.8	40.5	42.4	10.0	11.3	22.5	33.8	4.5	40.5	40.5	27.0	23.0	17.0	35.0	30.0	20.0
Sn	27.7	30.0	40.0	50.0	22.5	15.0	7.5	31.2	10.0	8.1	27.0	20.7	13.8	6.9	27.0	3.0	3.0	17.0	23.0	27.0	15.0	20.0	30.0
Products																							
Bi	33.9	36.7	43.4	43.9	30.7	51.5	38.9	46.2	37.6	31.9	56.9	52.0	46.1	33.3	45.8	29.1	41.9	37.2	37.5	33.0	38.2	36.9	37.8
MnO					2.0	41.0	47.6		41.3	46.7	1.1	2.1	34.6	47.6	1.2	53.2	44.9	52.1	46.6	35.0	46.5	39.7	19.3
SnO_2	45.1	46.5	48.5	29.8	16.6			35.1			7.9	12.5		1.0	33.8	1.2							20.2
$2MnO{\cdot}SnO_2$					46.9						24.6	28.5	4.9		10.0					18.5			
$Bi_2O_3{\cdot}2SnO_2$	1.0	2.1	3.2	0.0				18.2							2.2								
MnBi							0.9			1.7				2.3		1.8							
Mn_3Sn							12.6		19.3	18.5				12.0		11.5	13.3				13.0	0.8	
$MnSn_2$																		2.7	2.1		1.3	6.2	1.2
Unreacted reagents																							
Bi_2O_3	20.0	14.6	1.9	0.0	0.9	7.5							5.6	1.4	7.1	1.5							
Sn	0.0	0.0	3.0	26.4				0.5			9.4	1.6		1.1		1.3		0.7		0.3	1.0		1.1
Mn									1.8	1.2		0.1		1.4		0.4							
Minor products																							
$Bi_{0.05}Sn_{0.95}$					3.0								8.9					7.3	12.5	13.2		2.7	20.4
$MnO{\cdot}SnO_2$												3.3											
Mn_3Sn_2																						13.8	
MnO2																			1.1				

Values are given in wt-%

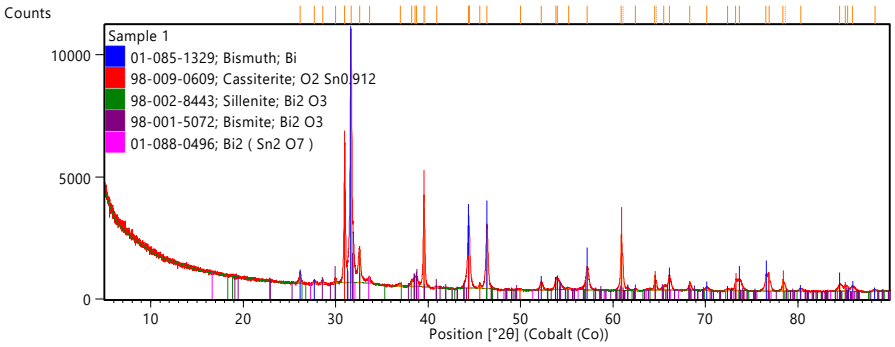
Counts
Sample 1
01-085-1329; Bismuth; Bi
98-009-0609; Cassiterite; O2 Sn0.912
98-002-8443; Sillenite; Bi2 O3
98-001-5072; Bismite; Bi2 O3
01-088-0496; Bi2 (Sn2 O7)
10000
5000
0
10
20
30
40
50
60
70
80
Position [°2θ] (Cobalt (Co))

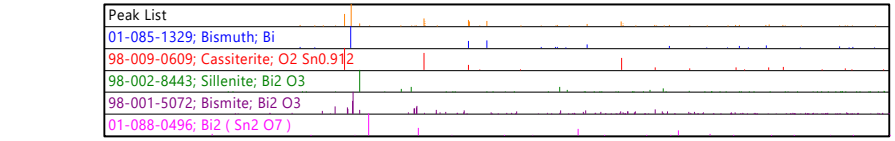
Peak List
01-085-1329; Bismuth; Bi
98-009-0609; Cassiterite; O2 Sn0.912
98-002-8443; Sillenite; Bi2 O3
98-001-5072; Bismite; Bi2 O3
01-088-0496; Bi2 (Sn2 O7)

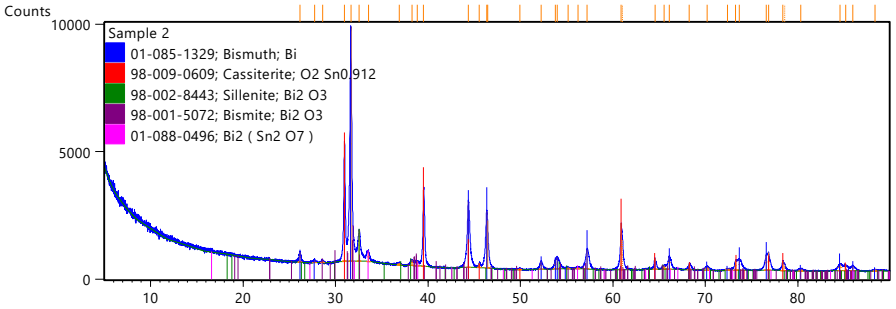
Counts
Sample 2
01-085-1329; Bismuth; Bi
98-009-0609; Cassiterite; O2 Sn0.912
98-002-8443; Sillenite; Bi2 O3
98-001-5072; Bismite; Bi2 O3
01-088-0496; Bi2 (Sn2 O7)
10000
5000
0
10
20
30
40
50
60
70
80

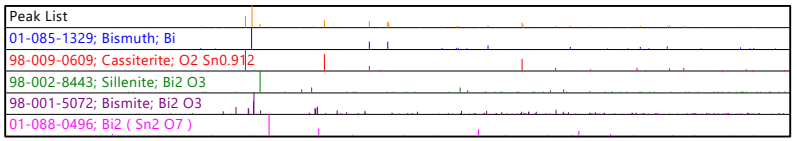
Peak List
01-085-1329; Bismuth; Bi
98-009-0609; Cassiterite; O2 Sn0.912
98-002-8443; Sillenite; Bi2 O3
98-001-5072; Bismite; Bi2 O3
01-088-0496; Bi2 (Sn2 O7)

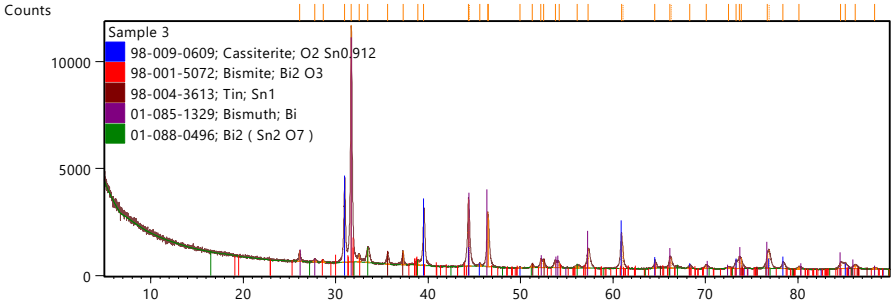
Counts
Sample 3
98-009-0609; Cassiterite; O2 Sn0.912
98-001-5072; Bismite; Bi2 O3
98-004-3613; Tin; Sn1
01-085-1329; Bismuth; Bi
01-088-0496; Bi2 (Sn2 O7)
10000
5000
0
10
20
30
40
50
60
70
80

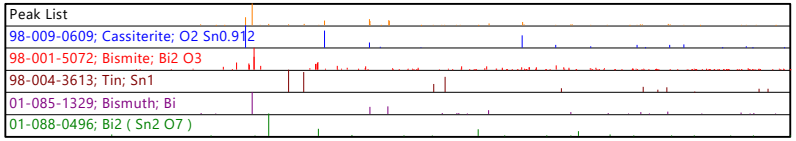
Peak List
98-009-0609; Cassiterite; O2 Sn0.912
98-001-5072; Bismite; Bi2 O3
98-004-3613; Tin; Sn1
01-085-1329; Bismuth; Bi
01-088-0496; Bi2 (Sn2 O7)

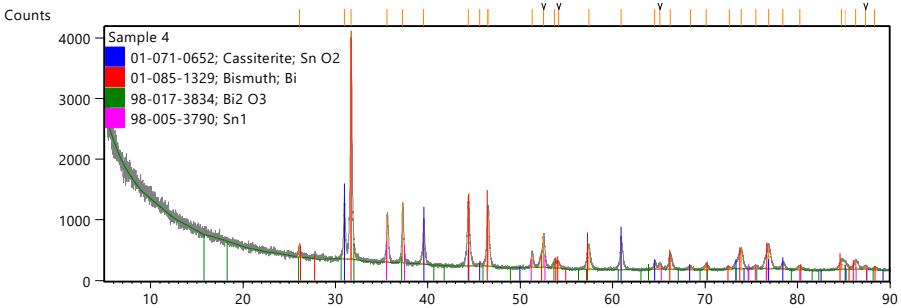
Counts
Sample 4
01-071-0652; Cassiterite; Sn O2
01-085-1329; Bismuth; Bi
98-017-3834; Bi2 O3
98-005-3790; Sn1
4000
3000
2000
1000
0
10
20
30
40
50
60
70
80
90

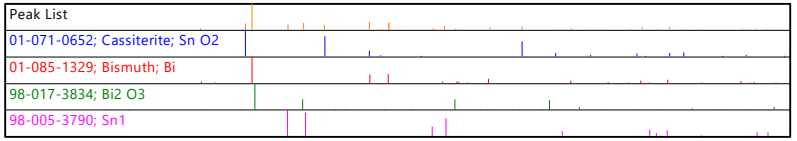
Peak List
01-071-0652; Cassiterite; Sn O2
01-085-1329; Bismuth; Bi
98-017-3834; Bi2 O3
98-005-3790; Sn1

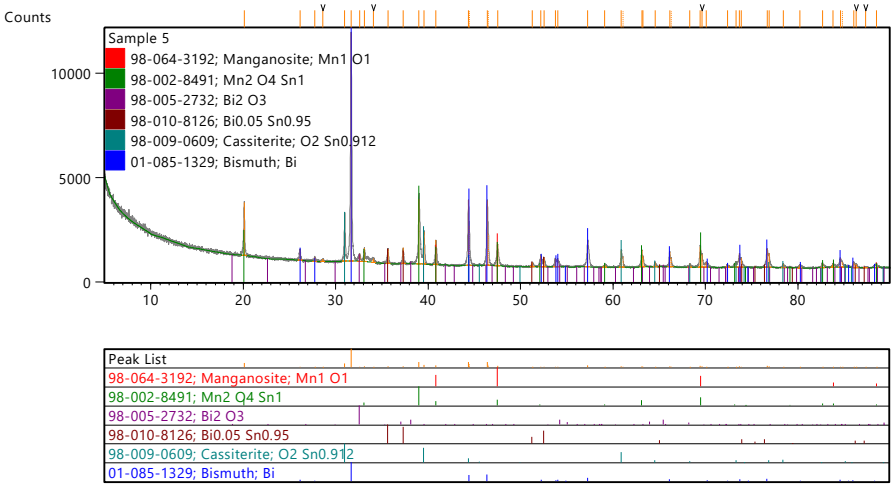
Counts
Sample 5
98-064-3192; Manganosite; Mn1 O1
98-002-8491; Mn2 O4 Sn1
98-005-2732; Bi2 O3
98-010-8126; Bi0.05 Sn0.95
98-009-0609; Cassiterite; O2 Sn0.912
01-085-1329; Bismuth; Bi
Peak List
98-064-3192; Manganosite; Mn1 O1
98-002-8491; Mn2 O4 Sn1
98-005-2732; Bi2 O3
98-010-8126; Bi0.05 Sn0.95
98-009-0609; Cassiterite; O2 Sn0.912
01-085-1329; Bismuth; Bi

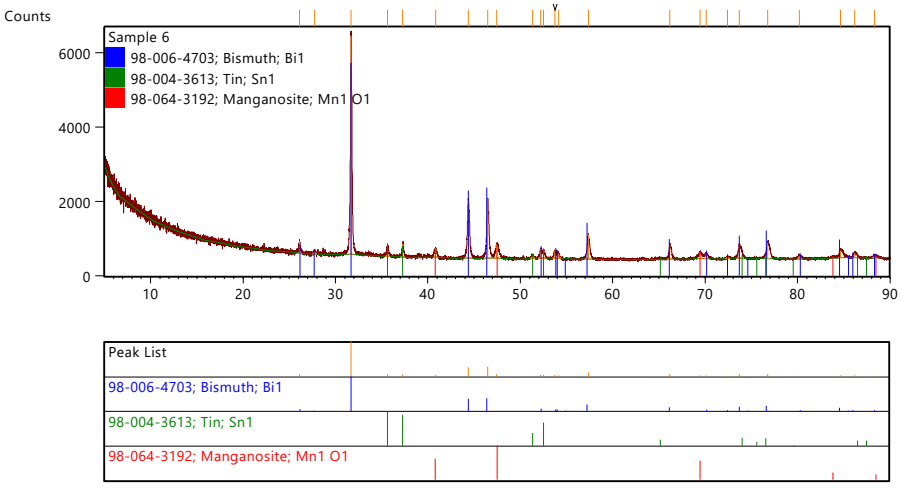
Counts
Sample 6
98-006-4703; Bismuth; Bi1
98-004-3613; Tin; Sn1
98-064-3192; Manganosite; Mn1 O1
Peak List
98-006-4703; Bismuth; Bi1
98-004-3613; Tin; Sn1
98-064-3192; Manganosite; Mn1 O1

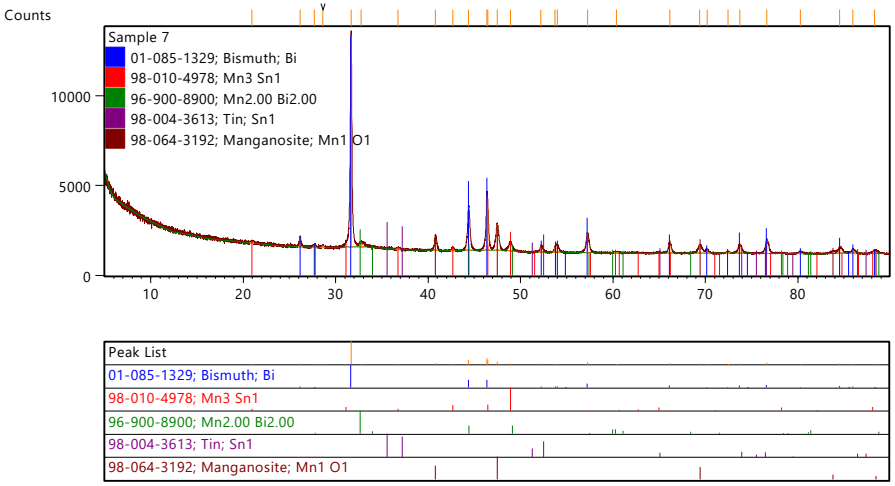
Counts
Sample 7
01-085-1329; Bismuth; Bi
98-010-4978; Mn3 Sn1
96-900-8900; Mn2.00 Bi2.00
98-004-3613; Tin; Sn1
98-064-3192; Manganosite; Mn1 O1
Peak List
01-085-1329; Bismuth; Bi
98-010-4978; Mn3 Sn1
96-900-8900; Mn2.00 Bi2.00
98-004-3613; Tin; Sn1
98-064-3192; Manganosite; Mn1 O1

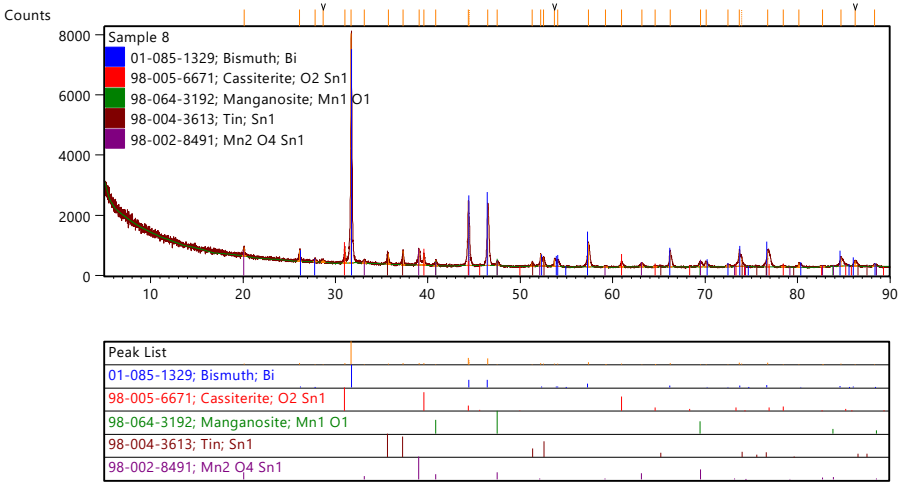
Counts
Sample 8
01-085-1329; Bismuth; Bi
98-005-6671; Cassiterite; O2 Sn1
98-064-3192; Manganosite; Mn1 O1
98-004-3613; Tin; Sn1
98-002-8491; Mn2 O4 Sn1
Peak List
01-085-1329; Bismuth; Bi
98-005-6671; Cassiterite; O2 Sn1
98-064-3192; Manganosite; Mn1 O1
98-004-3613; Tin; Sn1
98-002-8491; Mn2 O4 Sn1

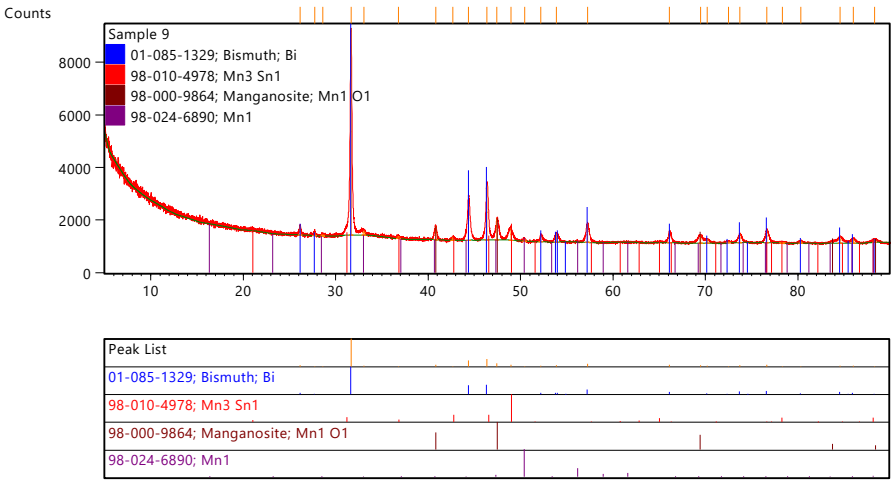
Counts
Sample 9
01-085-1329; Bismuth; Bi
98-010-4978; Mn3 Sn1
98-000-9864; Manganosite; Mn1 O1
98-024-6890; Mn1
Peak List
01-085-1329; Bismuth; Bi
98-010-4978; Mn3 Sn1
98-000-9864; Manganosite; Mn1 O1
98-024-6890; Mn1

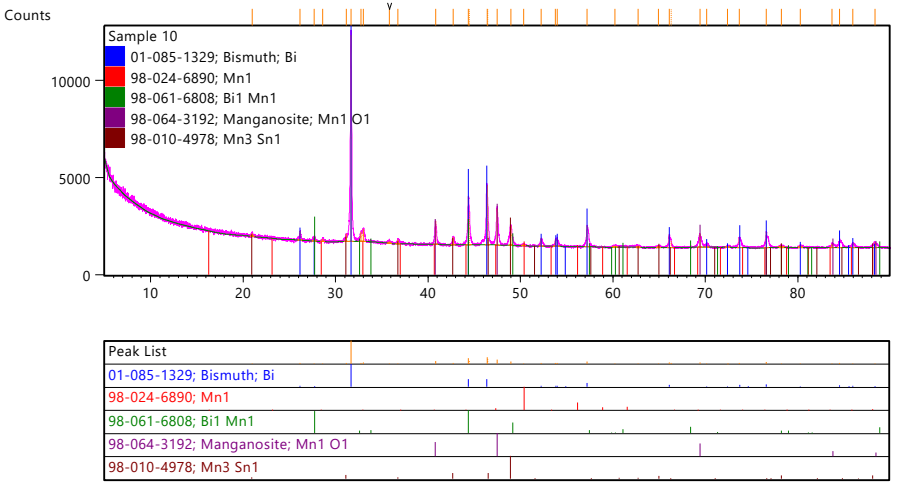
Counts
Sample 10
01-085-1329; Bismuth; Bi
98-024-6890; Mn1
98-061-6808; Bi1 Mn1
98-064-3192; Manganosite; Mn1 O1
98-010-4978; Mn3 Sn1
Peak List
01-085-1329; Bismuth; Bi
98-024-6890; Mn1
98-061-6808; Bi1 Mn1
98-064-3192; Manganosite; Mn1 O1
98-010-4978; Mn3 Sn1

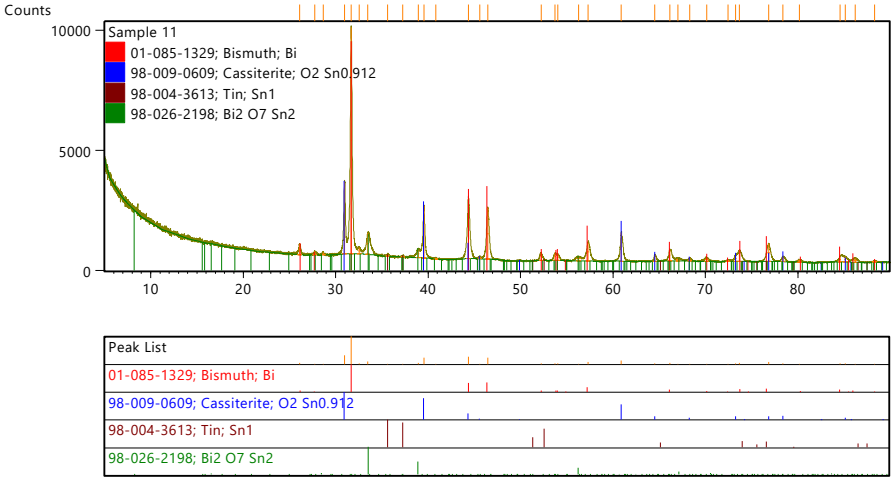
Counts
Sample 11
01-085-1329; Bismuth; Bi
98-009-0609; Cassiterite; O2 Sn0.912
98-004-3613; Tin; Sn1
98-026-2198; Bi2 O7 Sn2
Peak List
01-085-1329; Bismuth; Bi
98-009-0609; Cassiterite; O2 Sn0.912
98-004-3613; Tin; Sn1
98-026-2198; Bi2 O7 Sn2

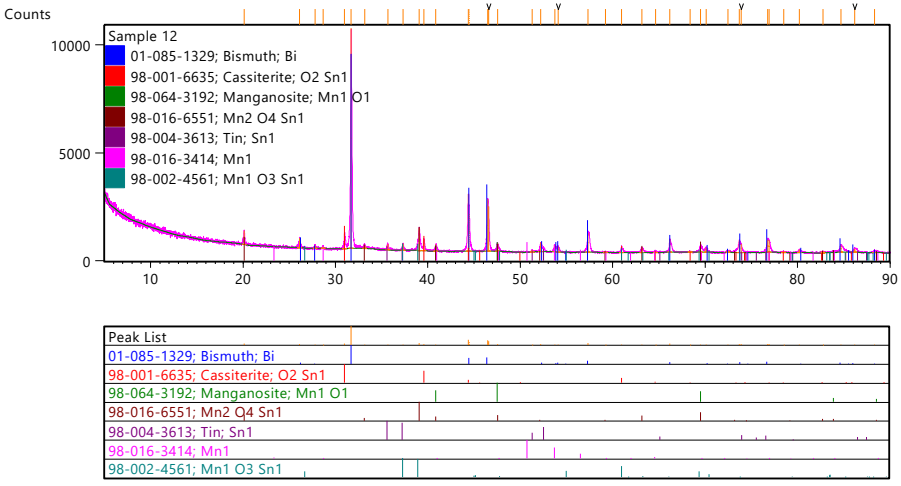
Counts
Sample 12
01-085-1329; Bismuth; Bi
98-001-6635; Cassiterite; O2 Sn1
98-064-3192; Manganosite; Mn1 O1
98-016-6551; Mn2 O4 Sn1
98-004-3613; Tin; Sn1
98-016-3414; Mn1
98-002-4561; Mn1 O3 Sn1
Peak List
01-085-1329; Bismuth; Bi
98-001-6635; Cassiterite; O2 Sn1
98-064-3192; Manganosite; Mn1 O1
98-016-6551; Mn2 O4 Sn1
98-004-3613; Tin; Sn1
98-016-3414; Mn1
98-002-4561; Mn1 O3 Sn1

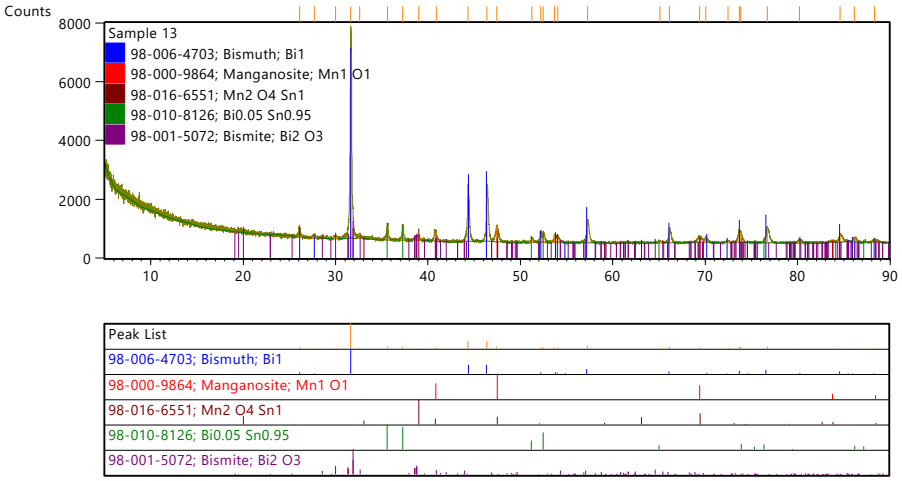
Counts
Sample 13
98-006-4703; Bismuth; Bi1
98-000-9864; Manganosite; Mn1 O1
98-016-6551; Mn2 O4 Sn1
98-010-8126; Bi0.05 Sn0.95
98-001-5072; Bismite; Bi2 O3
Peak List
98-006-4703; Bismuth; Bi1
98-000-9864; Manganosite; Mn1 O1
98-016-6551; Mn2 O4 Sn1
98-010-8126; Bi0.05 Sn0.95
98-001-5072; Bismite; Bi2 O3

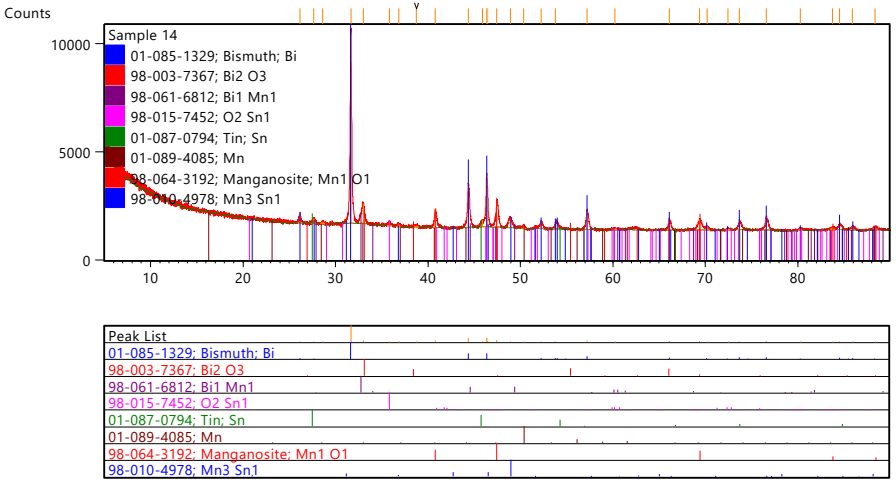
Counts
Sample 14
01-085-1329; Bismuth; Bi
98-003-7367; Bi2 O3
98-061-6812; Bi1 Mn1
98-015-7452; O2 Sn1
01-087-0794; Tin; Sn
01-089-4085; Mn
98-064-3192; Manganosite; Mn1 O1
98-010-4978; Mn3 Sn1
Peak List
01-085-1329; Bismuth; Bi
98-003-7367; Bi2 O3
98-061-6812; Bi1 Mn1
98-015-7452; O2 Sn1
01-087-0794; Tin; Sn
01-089-4085; Mn
98-064-3192; Manganosite; Mn1 O1
98-010-4978; Mn3 Sn1

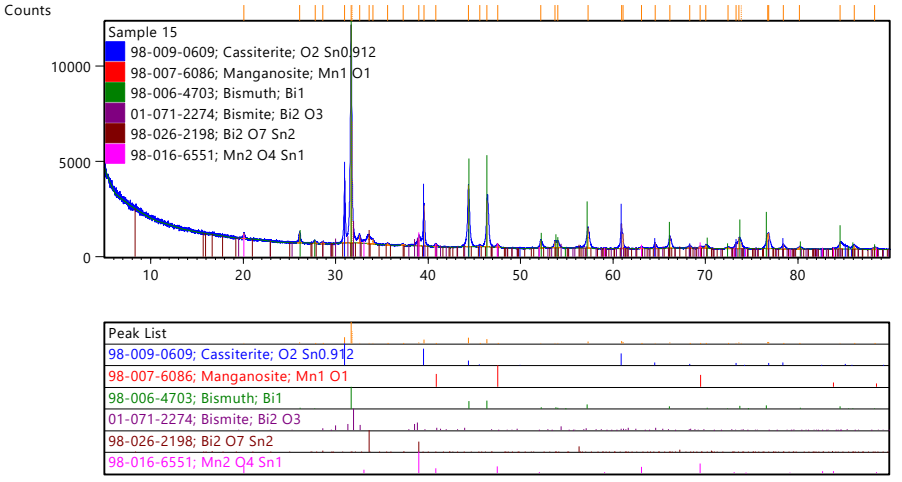
Counts
Sample 15
98-009-0609; Cassiterite; O2 Sn0.912
98-007-6086; Manganosite; Mn1 O1
98-006-4703; Bismuth; Bi1
01-071-2274; Bismite; Bi2 O3
98-026-2198; Bi2 O7 Sn2
98-016-6551; Mn2 O4 Sn1
Peak List
98-009-0609; Cassiterite; O2 Sn0.912
98-007-6086; Manganosite; Mn1 O1
98-006-4703; Bismuth; Bi1
01-071-2274; Bismite; Bi2 O3
98-026-2198; Bi2 O7 Sn2
98-016-6551; Mn2 O4 Sn1

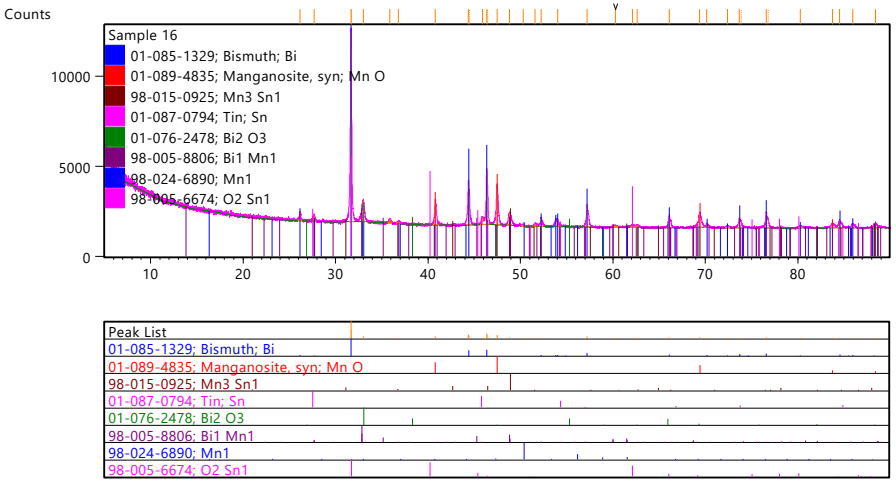
Counts
Sample 16
01-085-1329; Bismuth; Bi
01-089-4835; Manganosite, syn; Mn O
98-015-0925; Mn3 Sn1
01-087-0794; Tin; Sn
01-076-2478; Bi2 O3
98-005-8806; Bi1 Mn1
98-024-6890; Mn1
98-005-6674; O2 Sn1
Peak List
01-085-1329; Bismuth; Bi
01-089-4835; Manganosite, syn; Mn O
98-015-0925; Mn3 Sn1
01-087-0794; Tin; Sn
01-076-2478; Bi2 O3
98-005-8806; Bi1 Mn1
98-024-6890; Mn1
98-005-6674; O2 Sn1

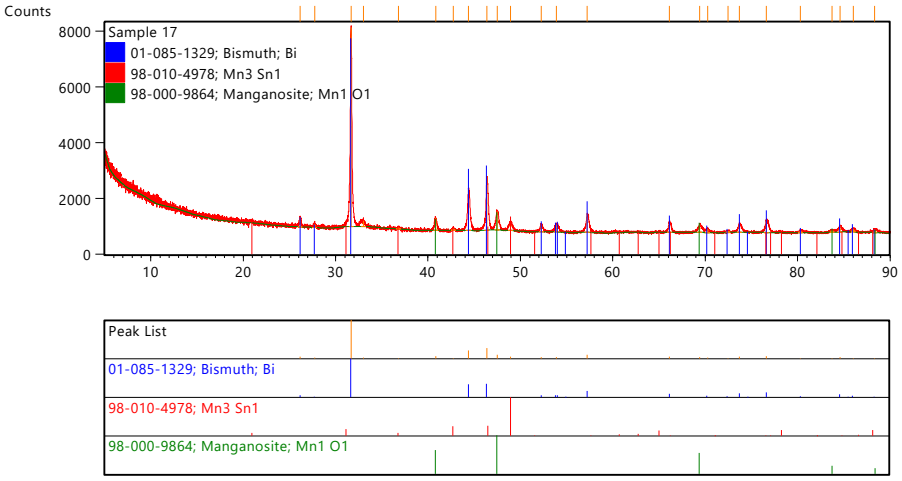
Counts
Sample 17
01-085-1329; Bismuth; Bi
98-010-4978; Mn3 Sn1
98-000-9864; Manganosite; Mn1 O1
Peak List
01-085-1329; Bismuth; Bi
98-010-4978; Mn3 Sn1
98-000-9864; Manganosite; Mn1 O1

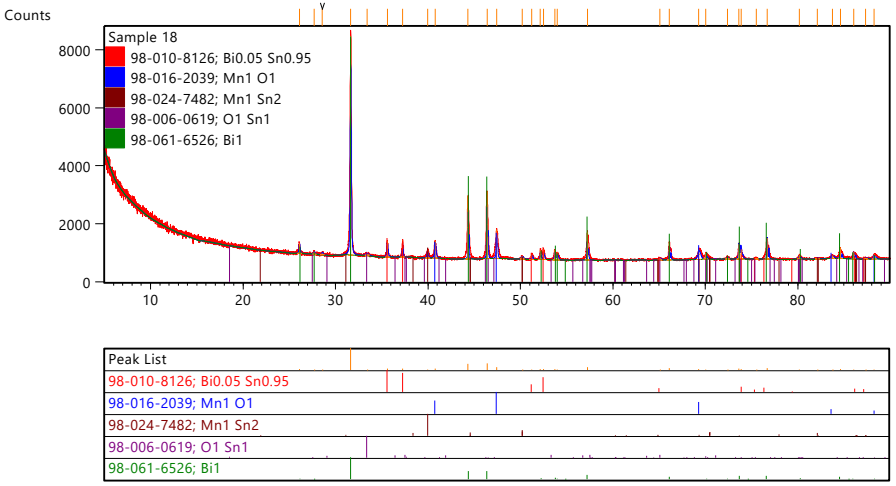
Counts
Sample 18
98-010-8126; Bi0.05 Sn0.95
98-016-2039; Mn1 O1
98-024-7482; Mn1 Sn2
98-006-0619; O1 Sn1
98-061-6526; Bi1
Peak List
98-010-8126; Bi0.05 Sn0.95
98-016-2039; Mn1 O1
98-024-7482; Mn1 Sn2
98-006-0619; O1 Sn1
98-061-6526; Bi1

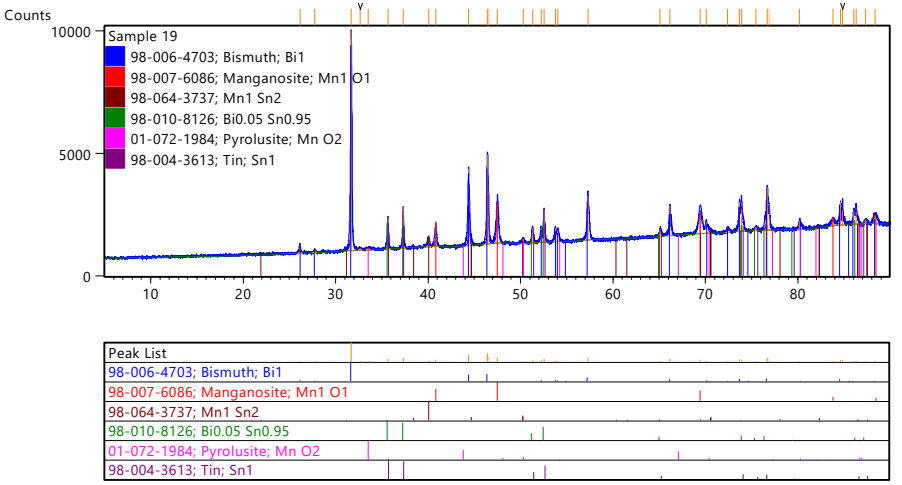
Counts
Sample 19
98-006-4703; Bismuth; Bi1
98-007-6086; Manganosite; Mn1 O1
98-064-3737; Mn1 Sn2
98-010-8126; Bi0.05 Sn0.95
01-072-1984; Pyrolusite; Mn O2
98-004-3613; Tin; Sn1
Peak List
98-006-4703; Bismuth; Bi1
98-007-6086; Manganosite; Mn1 O1
98-064-3737; Mn1 Sn2
98-010-8126; Bi0.05 Sn0.95
01-072-1984; Pyrolusite; Mn O2
98-004-3613; Tin; Sn1

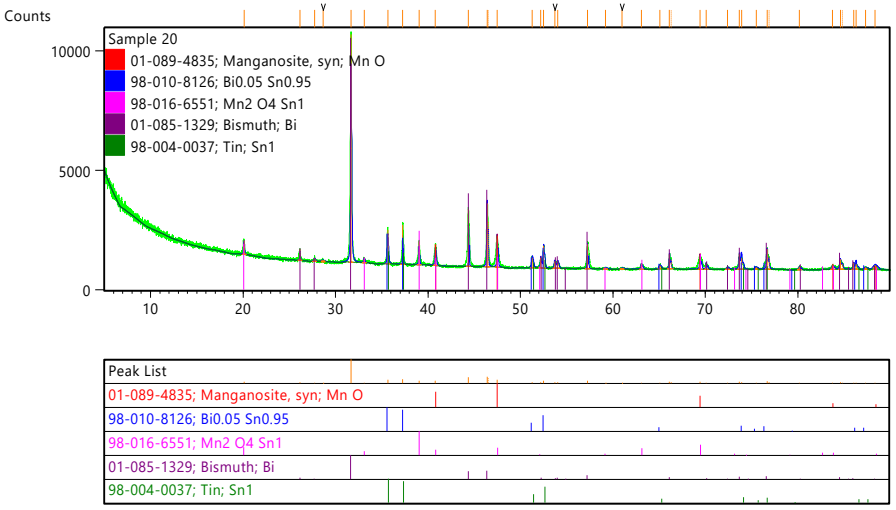
Counts
Sample 20
01-089-4835; Manganosite, syn; Mn O
98-010-8126; Bi0.05 Sn0.95
98-016-6551; Mn2 O4 Sn1
01-085-1329; Bismuth; Bi
98-004-0037; Tin; Sn1
Peak List
01-089-4835; Manganosite, syn; Mn O
98-010-8126; Bi0.05 Sn0.95
98-016-6551; Mn2 O4 Sn1
01-085-1329; Bismuth; Bi
98-004-0037; Tin; Sn1

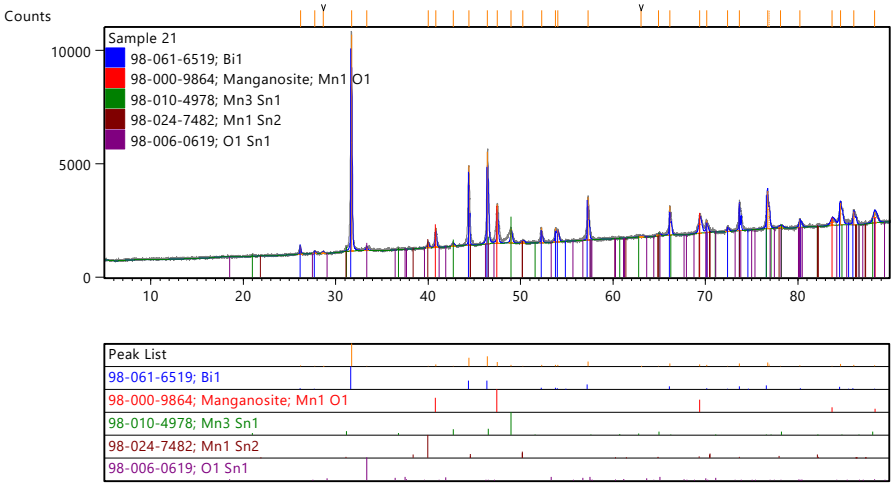
Counts
Sample 21
98-061-6519; Bi1
98-000-9864; Manganosite; Mn1 O1
98-010-4978; Mn3 Sn1
98-024-7482; Mn1 Sn2
98-006-0619; O1 Sn1
Peak List
98-061-6519; Bi1
98-000-9864; Manganosite; Mn1 O1
98-010-4978; Mn3 Sn1
98-024-7482; Mn1 Sn2
98-006-0619; O1 Sn1

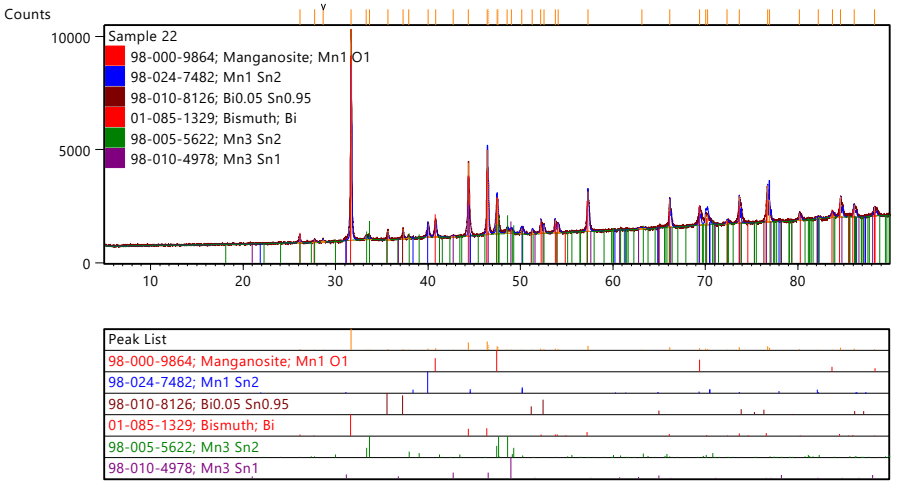
Counts
Sample 22
98-000-9864; Manganosite; Mn1 O1
98-024-7482; Mn1 Sn2
98-010-8126; Bi0.05 Sn0.95
01-085-1329; Bismuth; Bi
98-005-5622; Mn3 Sn2
98-010-4978; Mn3 Sn1
Peak List
98-000-9864; Manganosite; Mn1 O1
98-024-7482; Mn1 Sn2
98-010-8126; Bi0.05 Sn0.95
01-085-1329; Bismuth; Bi
98-005-5622; Mn3 Sn2
98-010-4978; Mn3 Sn1

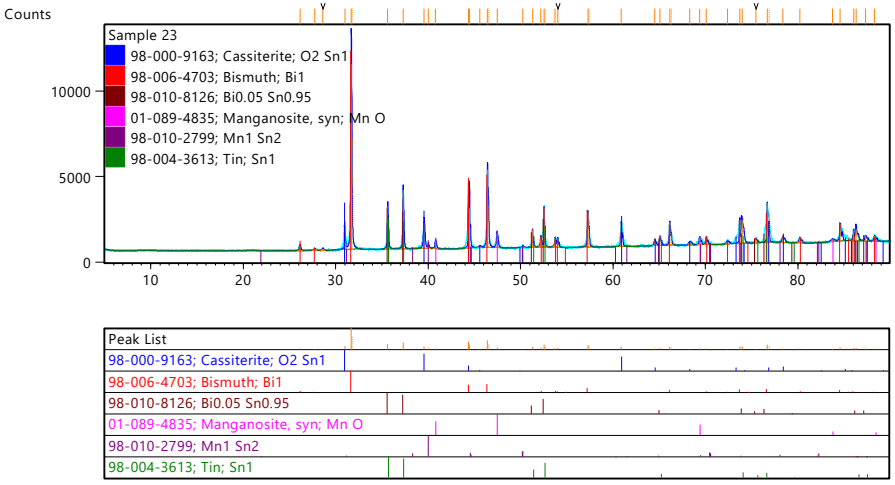
Counts
Sample 23
98-000-9163; Cassiterite; O2 Sn1
98-006-4703; Bismuth; Bi1
98-010-8126; Bi0.05 Sn0.95
01-089-4835; Manganosite, syn; Mn O
98-010-2799; Mn1 Sn2
98-004-3613; Tin; Sn1
Peak List
98-000-9163; Cassiterite; O2 Sn1
98-006-4703; Bismuth; Bi1
98-010-8126; Bi0.05 Sn0.95
01-089-4835; Manganosite, syn; Mn O
98-010-2799; Mn1 Sn2
98-004-3613; Tin; Sn1

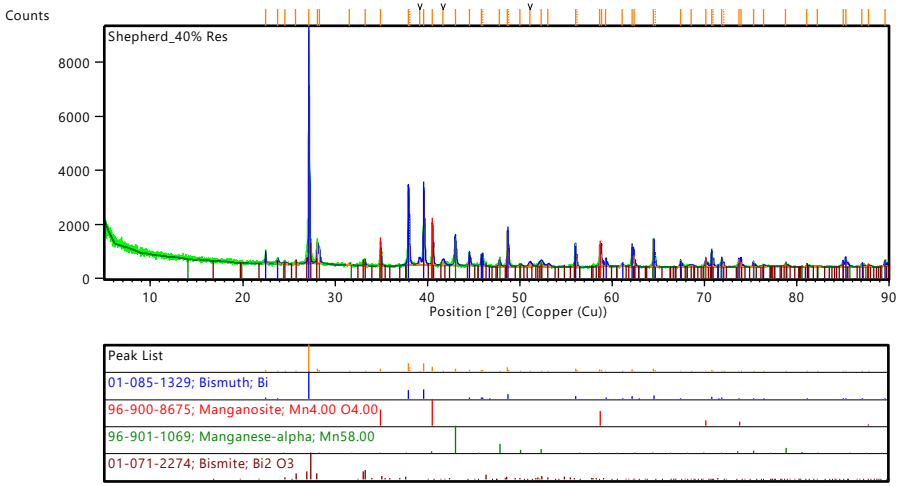
Counts
Shepherd_40% Res
Position [°2θ] (Copper (Cu))
Peak List
01-085-1329; Bismuth; Bi
96-900-8675; Manganosite; Mn4.00 O4.00
96-901-1069; Manganese-alpha; Mn58.00
01-071-2274; Bismite; Bi2 O3

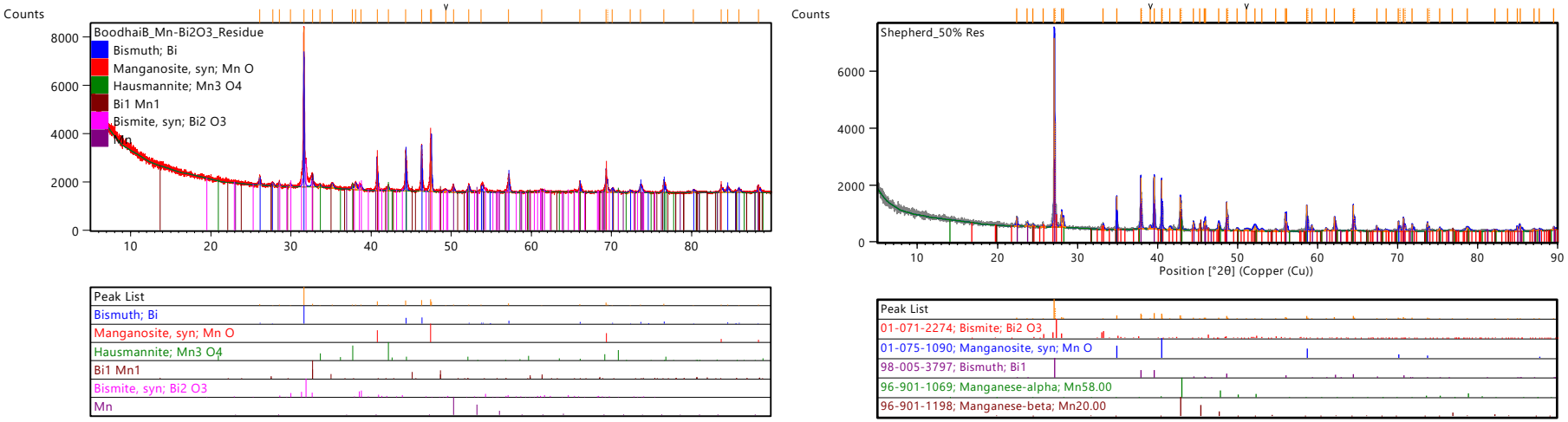

Figure S 2: XRD diffractograms of residues obtained after combustion in the glass tubes

Appendix C: One example of burning performance in a lead tube.

Some pictures of a burning performance in a lead tube filled with a composition Bi_2O_3:Mn:Sn = 63.7:22.5:13.8. “Start” means the ignition of the sparkler, and “End” means the end of the burning process. The direction of the arrow in the pictures was the axis of the burning front. The red zone in the oval in the picture “End” was the same as that in the last picture.